The Dissertation Committee for Joseph Louis Bass
certifies that this is the approved version of the following dissertation:

Nonholonomic Hamiltonian Method for Reacting Molecular Dynamics

Committee:

Eric P. Fahrenthold, Supervisor

Raul G. Longoria

Steven P. Nichols

Kamy Sepehrnoori

Eric M. Taleff

Nonholonomic Hamiltonian Method for Reacting Molecular Dynamics

by

Joseph Louis Bass

DISSERTATION

Presented to the Faculty of the Graduate School of

The University of Texas at Austin

in Partial Fulfillment

of the Requirements

for the Degree of

DOCTOR OF PHILOSOPHY

THE UNIVERSITY OF TEXAS AT AUSTIN

August 2017

Dedicated to my mother and father.

Acknowledgments

I am truly grateful to my advisor, Dr. Eric P. Fahrenthold, for giving me this opportunity. His support and guidance were paramount to the success of this project and my academic growth. I would also like to thank my dissertation committee member: Dr. Raul Longoria, Dr. Steven Nichols, Dr. Kamy Sepehrnoori, and Dr. Eric Taleff.

This research was supported by the Defense Threat Reduction Agency (Grant number HDTRA1-13-1-0023). The support and assistance of the program managers, Su Peiris and Allen Dalton, has been much appreciated. Computer time support was provided by the Texas Advanced Computing Center at the University of Texas at Austin.

Nonholonomic Hamiltonian Method for Reacting Molecular Dynamics

Publication No. _____

Joseph Louis Bass, Ph.D.
The University of Texas at Austin, 2017

Supervisor: Eric P. Fahrenthold

Macroscale, mesoscale, and ab initio models of reacting shock physics are based, in their most general forms, on rate law descriptions of the chemical processes of interest. Reacting molecular dynamics simulations, by contrast, typically employ potential functions (holonomic Hamiltonian methods) to model chemical reactions. An alternative approach to reacting molecular dynamics models the bonding-debonding process using a rate law, resulting in a nonholonomic Hamiltonian formulation. In previous work at macro and meso scales, discrete nonholonomic Hamiltonian methods have been applied to develop very general models of shock impact and fragmentation process. In this dissertation a similar nonholonomic modeling methodology is used, at the molecular scale, to explicitly model transient chemical processes. Note that the chemistry problem is much more difficult, since both dissociation (fragmentation) and the formation of new molecules must be modeled. The result is the first general reacting molecular dynamics formulation which explicitly

models chemical kinetics. Simulation results using this method show good agreement with experiment, for energy release and detonation products in two widely used explosives (HMX and RDX). The reacting molecular dynamics simulation results are used to propose reaction mechanisms and species concentration based kinetics models suitable for use in meso and macro scale shock to detonation simulations. Computational modeling of energetic materials is capable of estimating molecular behavior under conditions not amenable to direct experimental measurement. Further development of RMD methods may help to provide a better understanding of energetic material behavior. This in turn may help to develop improved insensitive high energy density materials.

Table of Contents

List of Tables

List of Figures

Chapter 1

Introduction

This dissertation develops and validates a new formulation of reacting molecular dynamics. The chapter begins with a discussion of previous work, followed by the motivation which drives this research and the corresponding research objectives. The chapter concludes with an overview of the organization in the dissertation.

1.1 Previous Work

Rapid advances in computing power over the past four decades have led to the development of various reacting molecular dynamics (RMD) formulations, intended for a range of applications and materials [7, 34, 60, 62]. These formulations can be broadly grouped into three categories: ad hoc methods, holonomic methods, and nonholonomic methods. Ad hoc methods are often designed for modeling a specific material or phenomenon. These formulations typically employ bonded and unbonded potential energy functions to model inter-atomic interactions and step changes in the bonded state [65, 102]. The step changes are used to switch between the bonded and unbonded potential energy functions, and the model may not satisfy conservation of energy [34].

Historically, these methods have been used to model polymerization processes, employing multistage algorithms to create and relax polymer chains [85, 115]. Specific multistage algorithms are in general applicable only to a material of interest, but have been shown to agree with experimental results [3].

In the literature, holonomic methods are by far the most prominent method and have been used to model a variety of systems including metals [21, 52, 81], energetic materials [103, 108, 124], silicon [35, 97], nanotubes (functionalization) [76], polymers [79], and other materials. Individual formulations can incorporate multiple parameterizations and functional forms, in order to better represent the physics of different systems [66, 116]. For example, the reacting forcefield method (ReaxFF) was initially parameterized for hydrocarbons [111], but was later parameterized for H, C, N, O systems (ReaxFFnitro). Conventionally, these methods are parameterized to match ab initio or empirical data. Holonomic formulations can be further broken down into two categories: Reactively Modified Standard Forcefield methods and Empirical Forcefield methods. Reactively Modified Standard Forcefield methods use equilibrium potential functions derived from well established non-reactive formulations such as CHARMM [113] or MM3 [63]. These equilibrium potentials are composed of molecular mechanics terms (two, three, and four body potentials) as well as van der Waals and Coulomb terms. The advantage of incorporating the potential energy functions from a standard non-reactive forcefield is that a developed database of equilibrium constants is available. Reactively Modified Standard Forcefield methods augment the equilibrium

potential functions with inter-atomic distance dependent switching schemes, which allows for a smooth transition between bonded and nonbonded potential functions. Conceptually, these switching schemes control the transition states during the bonding and de-bonding process. In the Reactive Molecular Dynamics Force Field method (RMDff) method [100], a distance dependent reaction coordinate (RC) is used to smoothly transition from bonded to non-bonded potential energy functions. Here, bonding occurs as RC goes from 0 to 1, while de-bonding is represented by RC moving from 1 to 0. A different switching scheme is used in the Empirical Valence Bond (EVB) [12, 94] method. In this formulation, instead of introducing a smooth reaction coordinate, eigenvalue calculations are used to identify the minimum energy path to be used in moving from a bonded to a non-bonded state. While this process is easily applied to two body interactions, transition potentials become difficult to obtain if more than two atoms participate in a bonding process.

Empirical Forcefield methods most often describe the bonded state by introducing a bond order term in the potential energy. While each Empirical Forcefield method has its own special attributes, the most widely used formulation is that imbedded in the code ReaxFF, developed by van Duin [111] in 2001. ReaxFF has been used by many groups to model a wide variety of materials including: hydrocarbons [22, 111], metals [23, 52, 81], silicon [35, 84], carbon nanotubes [76], glycine [89], sucrose [118], polymers [121], hydrazine [125], RDX [5, 20, 58, 78, 103–105, 117, 123, 124, 129], HMX [20, 67, 119, 124, 125], PETN [18, 127–129], TATP [29, 112], TNT [36, 40], CL-20 [40, 121],

nitromethane [41, 92], Fox-7 [58], and many others. The following discussion of Empirical Forcefield methods focuses on ReaxFF, since it is so widely used and since it exemplifies empirical forcefield methods.

The bond order variables in ReaxFF are a complex function of inter-atomic distance and atomic valence [77]. There are several intrinsic issues that arise when a holonomic formulation is used to model the bonded state. First, determining whether two atoms are bonded can be difficult. This is caused by difficulties in choosing a bond order value (between zero and one) which corresponds to a bonded atom configuration. The value suggested by van Duin is 0.3 [67], but values from 0.3 to 0.8 have been reported [40]. This can lead to ambiguity in the bonded states as well as large (and perhaps unstable) atom clusters in high pressure simulations [41]. Second, the holonomic bonding formulations are also prone to over and under coordination, since the bond orders show a strong dependence on inter-atomic distance and the associated potentials must satisfy strict smoothness requirements. This can result in unrealistic bonding in molecules and in general unrealistic atomic interactions. Third, chemical kinetic effects are not explicitly modeled during a simulation. Chemical reactions are generally described in a post processing mode, by selecting the bond order value which indicates a bonded pair. In an effort to minimize large cluster formation in high-temperature high-pressure simulations, Strachan [104] applied a bonding criterion that required the kinetic energy of an atom pair to be lower than the binding energy of the atom pair. Difficulties in formulating bonding criteria emphasize the disadvantages

of implicit (holonomic) modeling of chemical kinetics. Other Empirical Forcefield methods, including those of Abell [1] and Tersoff [109, 110], Reactive Empirical Bond Order (REBO) [16, 17, 38, 45–49, 80, 91, 95, 106], Charge Optimized Many Body (COMB) [21, 28, 61, 97, 98], and Stillinger Weber potential offshoots [44] use similar modeling techniques.

The potential energy function in the ReaxFF formulation is representative of those found in holonomic formulations; it is [111]:

$$E = E_{bond} + E_{over} + E_{under} + E_{val} + E_{tor} + E_{conj} + E_{pen} + E_{vdw} + E_{cou} \quad (1.1)$$

Here E_{bond} is a bond order dependent term, which calculates the bond energy associated with atom pairs. The E_{over} and E_{under} terms are penalty functions used to avoid over and under coordinated atoms. The valence and torsional energy contributions, E_{val} and E_{tor}, are bond order dependent terms which quantify the potential energy for three and four body interactions. These terms quantify the energy contributions due to non-equilibrium valence and torsional angles. The conjugation energy, E_{conj}, maximized for bond order values of 1.5 [43], is introduced to account for conjugation effects associated with alternating double bonds within molecules. An energy penalty, E_{pen}, is used to stabilize the system in the presence of over and under coordinated of atoms linked by two double bonds. The E_{vdw} term models van der Waals interactions; in the case of ReaxFF a Morse potential is used. The final energy term, E_{cou}, is a Coulomb interaction energy computed for all atom pairs [93]. The charge for each atom is determined at each time step using an Electronegativity Equalization Method (EEM) [43, 96]. Practitioners note that such charge

equilibration calculations are computationally expensive, so that most of the holonomic methods discussed here do not include it in their formulations.

Nonholonomic RMD methods apply nonholonomic constraints in describing the system dynamics. This research presents the first nonholonomic Hamiltonian methodology for reacting molecular dynamics [8, 9]. Note however that nonholonomic constraints have been introduced in some previous molecular dynamics (MD) simulations, to describe thermostats that control the system temperature. For example, several published thermostat models have been formulated to enforce the nonholonomic constraint:

$$\dot{\theta} = 0 \tag{1.2}$$

where θ is the system temperature [51]. A methodology for incorporating both holonomic and nonholonomic constraints in an MD formulation was discussed by Kutteh [55, 56]. However that work did not develop a nonholonomic RMD methodology.

Another important component of previous work in RMD, separate from the various formulations discussed above, is the consideration of which ensembles are assumed in conducting a simulation. In the literature [73], the microcanonical ensemble (NVE, which holds constant atom count and type, volume, and energy) and the canonical ensemble (NVT, which holds constant atom count and type, volume, and temperature) are the most common. In order to maintain an NVT ensemble, a thermostat is used to control the system temperature. Application of a standard thermostat controls the kinetic energy

in the system, to create conditions which reflect those observed in a physical system of interest. Thermostatting methods can be grouped into three categories: (1) stochastic methods, (2) strong coupling constraint methods, and (3) weak coupling constraint methods [51]. Stochastic thermostatting methods, like the one presented by Andersen [6], reset atomic momenta or apply stochastic forces to achieve the desired temperature. Strong coupling methods enforce the nonholonomic constraint of equation 1.2, and are labeled 'hard' boundary conditions since the temperature is maintained at the desired temperature at all time steps. A weakly coupled thermostat, like the one developed by Berendsen [13], applies a 'soft' boundary condition, since it causes the temperature to approach and fluctuate about the desired temperature. While each of these methods has advantages and disadvantages, a weakly coupled method is used in this research; it is used to approximate the physics of a bomb calorimetry experiment. Such experiments produce data which may be used to validate an RMD formulation.

Note that in the present work, we refer to an 'NVE' ensemble as a set of atoms, confined by wall potentials, which do not interact thermally with the environment. We refer to an 'NVT' ensemble as a set of atoms, confined by wall potentials, which do interact thermally with the environment, in order to move to or remain at a specified temperature.

1.2 Motivation

In their most general forms, ab initio, mesoscale, and macroscale models use rate laws to describe chemical processes. This suggests that attempts to formulate a molecular level model of the physical chemistry should consider a rate law description of the bonding and debonding process. In general, the resulting reacting molecular dynamics model will take a nonholonomic form. Conventional molecular dynamics simulations of reacting shocks employ a holonomic Hamiltonian formulation; the breaking and forming of covalent bonds is described by potential functions. In general the potential functions: (1) are algebraically complex, (2) must satisfy strict smoothness requirements, and (3) contain many fitted parameters. In conventional reacting molecular dynamics (holonomic formulations) transient processes of central interest in stability and sensitivity studies are not explicitly represented in the numerical simulation. Instead, the bonding and debonding process is inferred from inter atomic distances. In previous work [32, 33, 50, 53], Fahrenthold and co-workers have developed and validated against experiment very general models of shock impact and fragmentation processes, using discrete nonholonomic Hamiltonian methods at macro and meso scales. A similar nonholonomic modeling methodology can be used at the molecular scale to explicitly model transient chemical processes. Note that the chemistry problem is much more difficult, since both disassociation (fragmentation) and the formation of new molecules must be modeled.

Computational modeling of energetic materials is capable of estimat-

ing molecular behavior under conditions not amenable to direct experimental measurement. Further development of RMD methods may help to provide a better understanding of energetic material behavior. This in turn may help to develop improved insensitive high energy density materials. Noholonomic Hamiltonian methods offer important opportunities for the development of improved numerical models of shock-to-detonation processes in condensed phase explosives.

1.3 Research Objectives

This research develops the first nonholonomic Hamiltonian methodology for reacting molecular dynamics simulation. The general formulation was developed to model detonation phenomena, and is validated against experimental results for detonation in energetic materials. A bond order rate law eliminates ambiguity in the bonded states, and explicitly incorporates chemical kinetics into the numerical formulation. Thus, transient processes of central interest in energetic materials modeling are directly represented. Chemical kinetics models may be derived from the RMD simulations, for application in larger scale simulations.

1.4 Dissertation Organization

The central contributions of this research are: (1) the development of the first nonholonomic Hamiltonian formulation for reacting molecular dynamics, (2) the development of an explicit model of chemical kinetics at the

molecular scale, through the use of a bond order rate law, and (3) the development of chemical kinetic models for explosive detonation, and detonation products recombination, using RMD simulations.

The remaining chapters are organized as follows. Chapter 2 provides a brief discussion of the importance of energetic materials modeling, and indicates the advantages of a nonholonomic formulation, as compared to the current state of the art. This discussion is followed by the development of an RMD formulation for an NVE ensemble. This formulation is validated using two example problems, which model detonation in one and two dimensions respectively. Chapter 3 provides a brief discussion of experimental methods and modeling methods developed for the study of energetic materials. Next a very general RMD formulation is developed, suitable for performing both NVE and NVT simulations. The introduction of an entropy state is used to model the system thermodynamics, for example to thermostat the system to a desired temperature (NVT). Detonation simulations for RDX and HMX are used to validate the formulation, by comparison to published experiments. Chemical kinetics models are derived from the RMD simulation results presented for each explosive. Chapter 4 summarizes the contributions of the dissertation, and suggests possible directions for future work.

Chapter 2

NVE Formulation and Validation Simulations

The development of explosives in current commercial and defense use has been based largely on experiment, and modern compositions typically employ energetic materials that have been available, in their basic form, for at least fifty years. Much recent explosives research has been characterized by two pervasive themes: (1) interest in the development of new energetic materials with reduced sensitivity [87], and (2) interest in the increased use of computation [30], as an adjunct to experiment, in the development of new energetic materials with reduced sensitivity and improved performance. The critical importance of insensitive munitions in defense applications is widely recognized; well known accidents at Thule, Greenland, on board the USS Forrestal, and at Camp Doha, Kuwait emphasize the hazard. The inherent difficulties of high speed, high pressure, high temperature experimentation and the rapid development of computing capabilities have focused attention on the potential for modeling and simulation to assist in energetic materials design. [1]

[1]This chapter is based on: J. Bass and E. Fahrenthold, Nonholonomic Hamiltonian method for molecular dynamics simulations of reacting shocks. *Proceedings of 19th American physical Society SCCM Conference*, 2015. The co-author is an expert in Hamiltonian methods, the dissertation author's expertise is in reacting molecular dynamics.

Macroscale, mesoscale, and ab initio models of reacting shock physics are based, in their most general forms, on rate law descriptions of the chemical processes of interest. At the macroscale level, [57] the rate laws are ordinary differential equations describing the rates of change of concentrations of reactants and products. At the ab initio level, [70] the rate law of interest is the time dependent Schroedinger equation, a partial differential equation describing the evolution of the electronic wave function. In both cases, the rate laws explicitly describe transitions between equilibrium states. A notable exception to this modeling practice arises in molecular scale simulation [93], where position dependent potential functions are almost invariably used to represent the physics of chemical reactions.

2.1 Numerical Method

The difficulties of extending potential based (holonomic) reacting molecular dynamics methods to material systems with complex chemistry are widely recognized. In developing an alternative molecular scale modeling approach, it is important to note that general computational chemistry models developed for application at both higher (macro) and lower (electronic structure) scales are based on rate laws, that is a kinetic description of the transient bonding-debonding process. In a Hamiltonian context, such formulations are labeled nonholonomic, and offer great flexibility in nonlinear systems modeling. This section outlines a new nonholonomic formulation of reacting molecular dynamics, developed to model detonation dynamics in condensed phase explosives.

Note that the model described in this chapter is limited to NVE applications, and its derivation is presented in an abbreviated form. The general formulation presented in the next chapter is derived in detail.

The system potential energy is

$$V = V^{xyz}(\mathbf{c}) + \sum_{i=1}^{n} V_i \tag{2.1}$$

where V^{xyz} is a wall potential and the potential energy for atom 'i' is computed from the rate relation

$$\dot{V}_i = \dot{V}_i^{rea} + \dot{V}_i^{vdw} + \dot{V}_i^{mec} \tag{2.2}$$

with the second and third terms on the right hand side representing van der Waals and molecular mechanics contributions. The reacting potential is obtained by integrating

$$\dot{V}_i^{rea} = \sum_{j=1}^{n} [B_{ij} F_{ij}^{AR} + (1 - B_{ij}) F_{ij}^{R}] \, \dot{r}^{(ij)} \tag{2.3}$$

where the inter-atomic distance, $r^{(ij)}$, and the rate of change of the inter-atomic distance, $\dot{r}^{(ij)}$, are

$$(r^{(ij)})^2 = (\mathbf{c}^{(i)} - \mathbf{c}^{(j)})^2 \,, \qquad \dot{r}^{(ij)} = \frac{(\mathbf{c}^{(i)} - \mathbf{c}^{(j)}) \cdot (\dot{\mathbf{c}}^{(i)} - \dot{\mathbf{c}}^{(j)})}{r^{(ij)}} \tag{2.4}$$

with '$\mathbf{c}$' an atomic position vector. The bond order is defined by

$$B_{ij} = \frac{1}{2}(b_{ij} + b_{ji}) \tag{2.5}$$

and is computed from the rate relations

$$\tau_{ij} \dot{b}_{ij} + b_{ij} = b_{ij}^{rhs}(\mathbf{b}, \mathbf{c}) \tag{2.6}$$

with τ_{ij} a time constant for the bonding-debonding process. The right hand side function weights neighbor atoms as a function of position **c** and bond state **b** in order to compute atomic bond orders. The atomic interaction forces, F^{AR} and F^{R}, may be computed from non-analytic pseudo-potentials using

$$F_{ij} = -\frac{\partial\, V_{ij}}{\partial\, r^{(ij)}} \tag{2.7}$$

This is illustrated in Figure 2.1, which shows a non-analytic pseudo potential and the corresponding atomic interaction forces.

2.2 Incorporation of Existing Potential Functions

It is important to note that nothing in the nonholonomic formulation described here precludes the use of complex potential functions already developed and found to be accurate and effective. This is a consequence of the general fact that any holonomic Hamiltonian system can be modeled using a nonholonomic approach. To illustrate this point, consider the van der Waals potential energy in reference [91].

$$V_{ij}^{vdw} = P_0 + r^{(ij)}[P_1 + r^{(ij)}(P_2 + r^{(ij)}P_3)]\,; \qquad 1.75 \leq r^{(ij)} < 2.91 \tag{2.8}$$

$$V_{ij}^{vdw} = 4\epsilon\Big\{\Big(\frac{\sigma}{r^{(ij)}}\Big)^{12} - \Big(\frac{\sigma}{r^{(ij)}}\Big)^{6}\Big\}\,; \qquad 2.91 \leq r^{(ij)} < 7.31 \tag{2.9}$$

$$V_{ij}^{vdw} = \sum_{i=3}^{5} d_i (r^{(ij)} - 7.32)^i\,; \qquad 7.31 \leq r^{(ij)} < 7.32 \tag{2.10}$$

Here P_i, d_i ϵ and σ are constants. This potential can be differentiated to produce the rate form

$$\dot{V}_{ij}^{vdw} = [P_1 + 2r^{(ij)}(P_2 + 1.5r^{(ij)}P_3)]\,\dot{r}^{(ij)}\,; \qquad 1.75 \leq r^{(ij)} < 2.91 \tag{2.11}$$

$$\dot{V}_{ij}^{vdw} = 4\epsilon\Big\{12\Big(\frac{\sigma}{r^{(ij)}}\Big)^{11}\Big(\frac{-\sigma}{(r^{(ij)})^2}\Big) - 6\Big(\frac{\sigma}{r^{(ij)}}\Big)^{5}\Big(\frac{-\sigma}{(r^{(ij)})^2}\Big)\Big\}\,\dot{r}^{(ij)}\,; \qquad 2.91 \le r^{(ij)} < 7.31 \quad (2.12)$$

$$\dot{V}_{ij}^{vdw} = \sum_{i=3}^{5} i\,d_i(r^{(ij)} - 7.32)^{i-1}\,\dot{r}^{(ij)}\,; \qquad 7.31 \le r^{(ij)} < 7.32 \quad (2.13)$$

These potential energy evolution equations are nonholonomic constraints on the system level model. In the rate based NVE model developed here, the parameters P_i, d_i, ϵ and σ may be expressed as a function of the states while conserving energy in the system.

2.3 Example Problem: 1-D Detonation

This section presents a one dimensional example problem. The first subsection introduces the example problem, including a discussion of previous work. The second subsection describes the numerical method used to model the physics, and the third subsection presents the simulation results.

2.3.1 Introduction

The first example problem is a one dimensional simulation of detonation in solid nitric oxide. This problem has been previously studied in simulation by Elert [31], and experimental mass spectrometry studies of detonation in solid nitric oxide have been reported by Bulusu [19]. The initial configuration, taken from reference [31], is a repeating chain of N-O O-N unit cells, as pictured in Figure 2.3. The 'detonation' reaction proposed by Elert and reproduced in

this research is:

$$2NO \rightarrow N_2 + O_2 \tag{2.14}$$

Detonation is initiated by setting the velocities of the six left-most atoms to a high value. Three simulations were run, with initial velocities of 4, 6 and 8 km/s.

2.3.2 Numerical Formulation

The potential energy evolution equations (nonholonomic constraints) take the following form:

$$\dot{V}^{(i)} = \dot{V}^{(i)}_{wall} + \sum_{j=1}^{N} B_{ij}\dot{V}^{(ij)}_{bond} + (1 - B_{ij})\dot{V}^{(ij)}_{nonbonded} \tag{2.15}$$

where $\dot{V}^{(ij)}_{bond}$ and $\dot{V}^{(ij)}_{nonbonded}$ are derived from the bonded and unbonded potential energy functions in reference [31]. In the cited reference, the bonded (V_{bond}) and unbonded ($V_{nonbonded}$) potential energy functions have the form

$$V_{bond}(r^{(ij)}) = D_e^{(ij)}\Big\{exp[-2\beta^{(ij)}(r^{(ij)} - r_e^{(ij)})] - 2\,exp[-\beta^{(ij)}(r^{(ij)} - r_e^{(ij)})]\Big\} \tag{2.16}$$

$$V_{nonbonded}(r^{(ij)}) = \frac{A^{(ij)}}{(r^{(ij)})^6} - Z^{(ij)}exp(-\alpha^{(ij)}r^{(ij)}) \tag{2.17}$$

where $A^{(ij)}$ and $Z^{(ij)}$ are defined as

$$A^{(ij)} = \frac{\epsilon^{(ij)}\alpha^{(ij)}(\rho^{(ij)})^7}{6 - \alpha^{(ij)}\rho^{(ij)}}\,, \qquad Z^{(ij)} = \frac{6A^{(ij)}exp(\alpha^{(ij)}\rho^{(ij)})}{\alpha^{(ij)}(\rho^{(ij)})^7} \tag{2.18}$$

The parameters $D_e^{(ij)}$, $r_e^{(ij)}$, $\beta^{(ij)}$, $\alpha^{(ij)}$, $\epsilon^{(ij)}$ and $\rho^{(ij)}$ are the constants listed in Table 2.1. Differentiation of V_{bond} and $V_{nonbonded}$ provides the evolution

equations

$$\dot{V}_{bond}^{(ij)} = D_e^{(ij)}\Big\{ -2\beta^{(ij)} exp[-2\beta^{(ij)}(r^{(ij)} - r_e^{(ij)})] + 2\beta^{(ij)} exp[-\beta^{(ij)}(r^{(ij)} - r_e^{(ij)})]\Big\}\dot{r}^{(ij)} \quad (2.19)$$

$$\dot{V}_{nonbond}^{(ij)} = \Big[-6\frac{A^{(ij)}}{(r^{(ij)})^7} + Z^{(ij)}\alpha^{(ij)} exp(-\alpha^{(ij)} r^{(ij)})\Big]\dot{r}^{(ij)} \quad (2.20)$$

The repulsive part of a Lennard-Jones potential is used to represent a container wall

$$\dot{V}_{wall}^{(i)} = \dot{V}_{wall\,1}^{(i)} + \dot{V}_{wall\,2}^{(i)} \quad (2.21)$$

where

$$\dot{V}_{wall\,1}^{(i)} = -12\Big(\frac{\sigma}{r^{(iw_1)}}\Big)^{11}\Big(\frac{\sigma}{(r^{(iw_1)})^2}\Big)\dot{r}^{(iw_1)} f_s(r^{(iw_1)}) \quad (2.22)$$

$$\dot{V}_{wall\,2}^{(i)} = -12\Big(\frac{\sigma}{r^{(iw_2)}}\Big)^{11}\Big(\frac{\sigma}{(r^{(iw_2)})^2}\Big)\dot{r}^{(iw_2)} f_s(r^{(iw_2)}) \quad (2.23)$$

and f_s is a step cut off function The parameters $r^{(iw_1)}$ and $r^{(iw_2)}$ are the distances between atom 'i' and the left and right walls respectively,

$$(r^{(iw)})^2 = (c^{(i)} - c^{(w)})^2 \qquad \dot{r}^{(iw)} = \frac{(c^{(i)} - c^{(w)})(\dot{c}^{(i)})}{r^{(iw)}} \quad (2.24)$$

and $c^{(i)}$ is an atomic position.

The formulation described here differs fundamentally from that of Elert, since the bonded state is determined by integrating a rate law.

2.3.3 Simulation Results

Six snapshots depicting the first 2.63 picoseconds of the v_o=4 km/s simulation are shown in Figure 2.4. The simulation result used to compare

these simulations with those of Elert is the detonation wave speed, v_{wave}, which has an experimental value of 5.5 km/s [31]. The detonation wave speed is computed from the simulation, as follows. First, the position ($c_{wave}^{(k)}$) of the detonation wave front at time step 'k', is determined: it is set equal to the position of the furthest right atom whose squared velocity exceeds a specified value. Second, the detonation wave velocity is computed using

$$v_{wave}^{(k+1)} = \frac{c_{wave}^{(k+1)} - c_{wave}^{(k)}}{t^{(k+1)} - t^{(k)}} \tag{2.25}$$

where $t^{(k)}$ is the simulation time at step 'k'. The computed wave velocities are averaged with those at neighboring time steps in order to provide a final estimate for the detonation wave velocity. The final wave speed versus time results for the three simulations are shown in Figure 2.2. All three simulations reach steady state by 2 picoseconds, and the estimated wave speeds range from 5.05 km/s (v_o=4 km/s case) to 5.36 km/s (v_o=8 km/s case). This result compares well with the experimental value of 5.5 km/s. Note that previous work computed a value of 11 km/s for the steady state detonation wave velocity [31].

2.4 Example Problem: 2-D Detonation

This section presents a two dimensional example problem. The first subsection describes the problem and discusses previous work. The second and third subsections describe the numerical method and discuss the simulation results.

2.4.1 Introduction

The second test problem simulates the detonation of a confined, homogeneous crystal composed of covalently bonded A-B molecules in a two dimensional crystal lattice. This test problem has been simulated by groups at NRL [16], ARL [90, 91], and LANL [46, 47] using potentials which take an exponential form; the bond state interpolation schemes and other details vary between the last cited papers. Hence the work discussed here describes application of a new RMD method for NVE systems simulation on a widely studied test problem.

A schematic of the initial atomic configuration is shown in Figure 2.5. This modeled reaction is:

$$2AB \rightarrow A_2 + B_2. \tag{2.26}$$

Detonation is initiated by impulse loading of the crystal unit cells located along the left side boundary; a sustained detonation propagates across the modeled crystal, from left to right.

2.4.2 Numerical Formulation

The evolution equations (nonholonomic constraints) for the system are

$$\dot{V}^{(ij)} = f_s(r_{ij})[(1 - B_{ij})\frac{\partial V_R^{(ij)}}{\partial r_{ij}}\dot{r}_{ij} + B_{ij}\frac{\partial V_{AR}^{(ij)}}{\partial r_{ij}}\dot{r}_{ij}] + \frac{\partial V_{VDW}^{(ij)}}{\partial r_{ij}}\dot{r}_{ij} \tag{2.27}$$

where f_s is a step cutoff function, V_R is a repulsive (unbonded) potential, V_{AR} is a attractive-repulsive (bonded) potential and V_{VDW} is a van der Waals

potential. The model employs exponential pseudo-potentials of the form described in reference [91], but without: (1) the complex switching function used to discriminate among near neighbors, and (2) their multi-parameter augmentation of the van der Waals potential. In reference [91] the potential energy has the form

$$V' = \sum_{i}^{N} \sum_{j>i}^{N} \Big\{ f_c \left[V_R^{'(ij)} - B'_{ij} V_A^{'(ij)} \right] + V_{vdw}^{'(ij)} \Big\} \tag{2.28}$$

where f_c is a smooth cutoff function, B'_{ij} is a smooth algebraic Tersoff bond order function, V'_R is a repulsive potential and V'_A is an attractive potential. The potentials take the form

$$V_R^{'(ij)} = \frac{D_e^{(ij)}}{S-1} exp[-\alpha (2S)^{.5} (r^{(ij)} - r_e^{(ij)})] \tag{2.29}$$

$$V_A^{'(ij)} = \frac{S D_e^{(ij)}}{S-1} exp[-\alpha \Big(\frac{2}{S}\Big)^{.5} (r^{(ij)} - r_e^{(ij)})] \tag{2.30}$$

where S and α are constants, D_e is the well depth, and r_e is the equilibrium inter-atomic distance (values are given in Table 2.2). The bonded and unbonded potentials (V_{AR} and V_R) are obtained by setting B'_{ij} equal to one and then equal to zero, so that

$$V_{AR}^{(ij)} = V_R^{'(ij)} - V_A^{'(ij)} \,, \qquad V_R^{(ij)} = V_R^{'(ij)} \tag{2.31}$$

Since

$$\frac{\partial V_{AR}^{(ij)}}{\partial r_{ij}} \, \dot{r}_{ij} = \dot{V}_R^{'(ij)} - \dot{V}_A^{'(ij)} \,, \qquad \frac{\partial V_R}{\partial r_{ij}} \, \dot{r}_{ij} = \dot{V}_R^{'(ij)} \tag{2.32}$$

it follows that

$$\dot{V}_R^{'(ij)} = \frac{D_e^{(ij)}}{S-1} (-\alpha (2S)^{.5}) exp[-\alpha (2S)^{.5} (r^{(ij)} - r_e^{(ij)})] \dot{r}^{(ij)} \tag{2.33}$$

$$\dot{V}_A^{'(ij)} = \frac{SD_e^{(ij)}}{S-1}(-\alpha\Big(\frac{2}{S}\Big)^{.5})exp[-\alpha\Big(\frac{2}{S}\Big)^{.5}(r^{(ij)} - r_e^{(ij)})]\dot{r}^{(ij)} \tag{2.34}$$

2.4.3 Results

The simulation results are shown in Figure 2.6, which depicts four snapshots showing the progression of the detonation wave from left to right. The detonation wave velocity computed from this simulation is 10.2 km/s. There are no experimental data for comparison, since this test problem does not model any real material. The literature has reported a range of computed detonation velocities: 6.6 km/s by ARL [91], 9.3 km/s by NRL [16], and 9.5 km/s by LANL [47]. The most recent cited work, from LANL, indicates results similar those computed in this work.

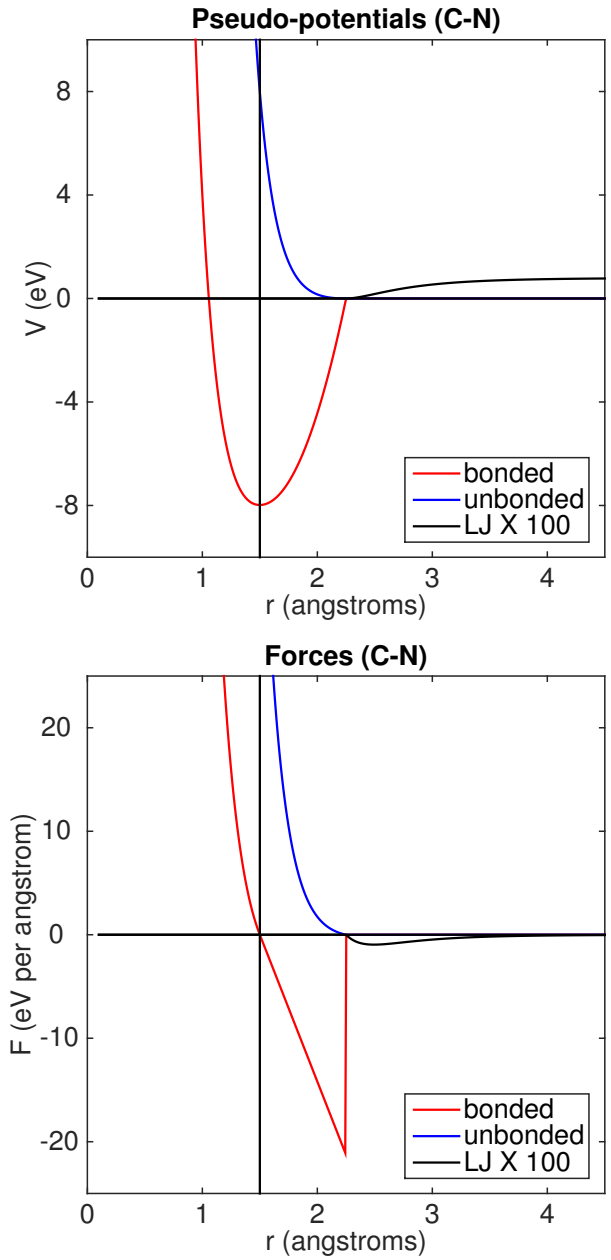

Figure 2.1: Pseudo-potential for the carbon-nitrogen interaction (top), and inter-atomic forces (bottom) derived from the pseudo potential

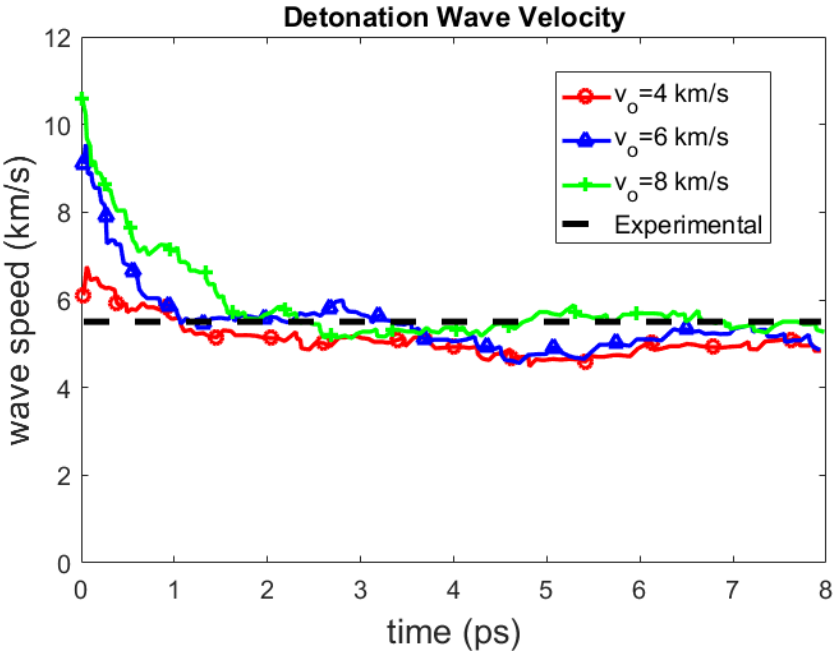

Figure 2.2: Wave velocity versus time for initial shocks of 4, 6, and 8 km/s (1-D example problem)

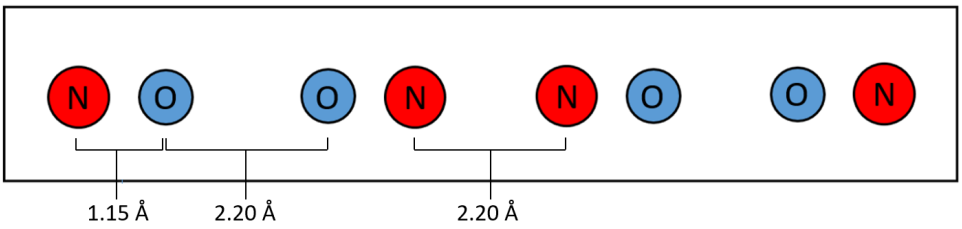

Figure 2.3: Initial atomic configuration (1-D example problem)

Table 2.1: Parameters for the 1-D example problem

Bond Type	$D_e^{(ij)}$ (eV)	$r_e^{(ij)}$ (Å)	$\beta^{(ij)}$ (Å^{-1})	$\alpha^{(ij)}$ (Å^{-1})	$\epsilon^{(ij)}$ (eV)	$\rho^{(ij)}$ (Å)
N-N	9.755	1.098	2.689	.044	.259	2.2
O-O	5.235	1.208	2.654	.047	.259	2.2
N-O	6.615	1.151	2.743	.044	.259	2.2

Table 2.2: Parameters for the 2-D example problem

Parameter	Unit	Value
$D_e^{(AA)}$	eV	5
$D_e^{(BB)}$	eV	2
$D_e^{(AB)}$	eV	1
$r_e^{(AA)}$	Å	1.2
$r_e^{(BB)}$	Å	1.5
$r_e^{(AB)}$	Å	1.35
S	-	1.8
α	Å^{-1}	2.7
m_A	amu	15
m_B	amu	46

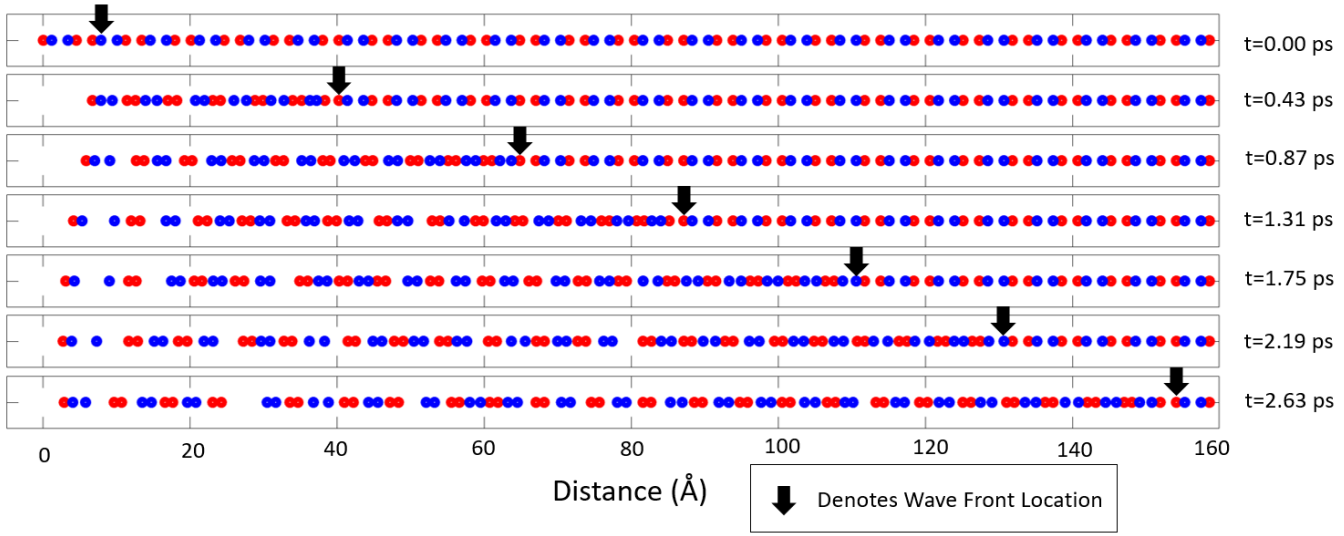

Figure 2.4: Detonation wave propagation snapshots (1-D example problem)

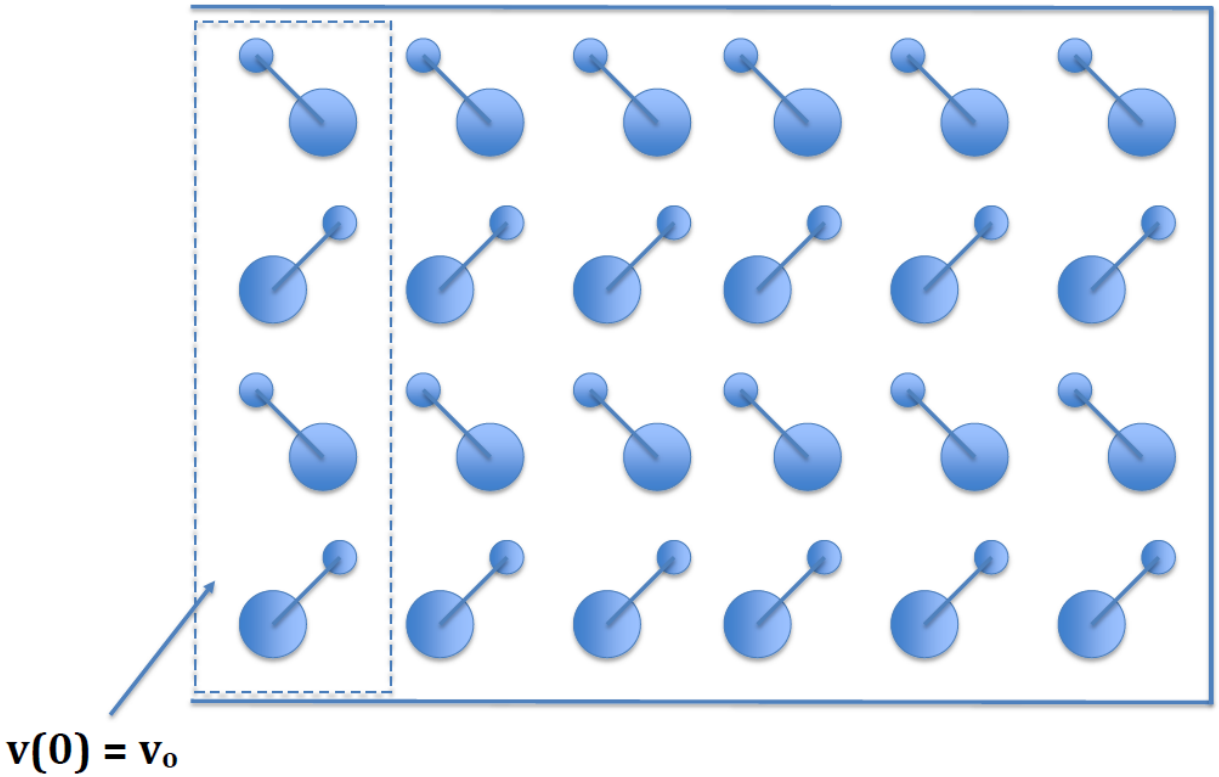

Figure 2.5: Initial atomic configuration schematic (2-D detonation example problem)

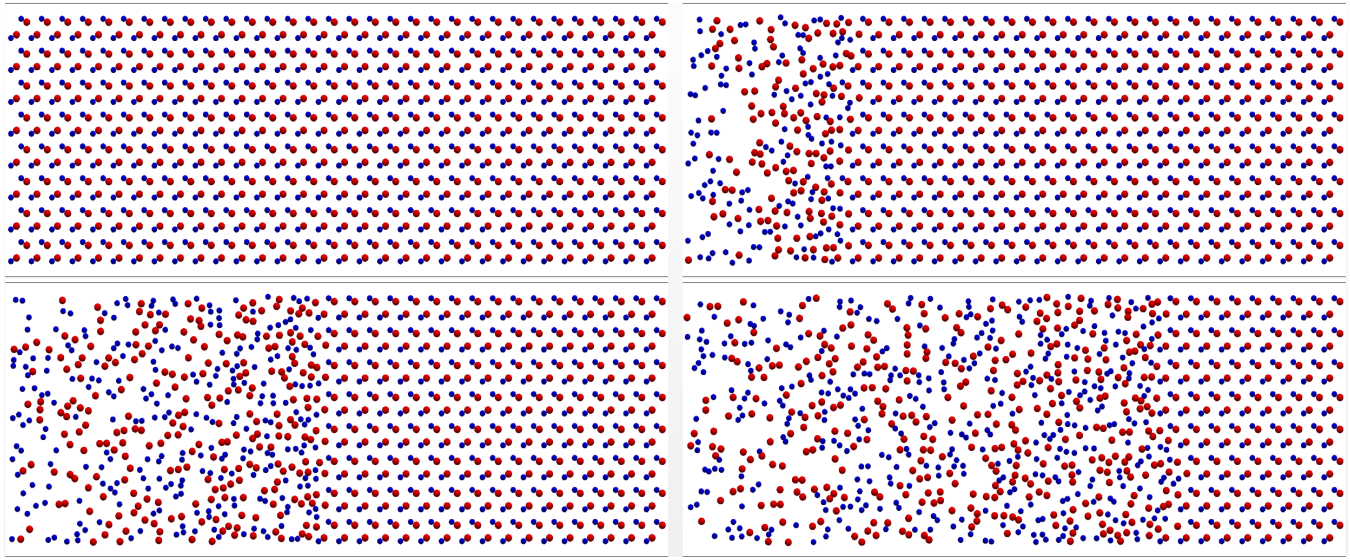

Figure 2.6: Detonation wave propagation snapshots (2-D example problem)

Chapter 3

General Formulation and Validation Simulations

This chapter develops and validates a general nonholonomic RMD formulation capable of simulating reacting shocks in the NVE and NVT ensembles. The chapter begins with a discussion of experimental methods and modeling techniques for detonation studies, followed by the derivation of Hamilton's equations for the nonholonomic system. The formulation is then validated by comparing the results of detonation simulations with experimental data, for two energetic materials. Chemical kinetics models for both of the energetic materials are obtained from the RMD simulation data.[1]

A wide variety of shock tube [64], bomb calorimetry [82, 83], pyrolysis [10], and spectroscopy [74] methods have been applied to investigate reaction mechanisms, reaction rates, and decomposition products in energetic materials [72, 107]. Despite considerable success, experimental measurement of detonation dynamics remains difficult and has motivated complimentary modeling research. Similarly, published computational work on the application of ab

[1]This chapter is based partly on: J. Bass and E. Fahrenthold, A kinetic formulation of reacting molecular dynamics. *Proceedings of the ASME 2016 International Mechanical Engineering Congress and Exposition*, 2016. The co-author is an expert in modeling Hamiltonian methods, the dissertation author's expertise is in modeling reactive systems.

initio [20, 99, 126], molecular dynamics [42, 103, 123], and multiscale [37, 59] modeling methods to energetic materials has proven the value of coordinated experimental and computational research, but also emphasized the need for improved numerical models of detonation processes.

At the molecular scale, a prominent and longstanding goal of computational research has been the accurate simulation of shock induced detonation in condensed phase explosives. Specific goals include validation of the numerical model against published experimental data on energy release and detonation products, and the prediction of reaction mechanisms and rates at conditions not amenable to direct experimental measurement. Perhaps the most important obstacle in the pursuit of this goal has been the difficulty of extending reacting potential methods [47, 95], developed over several decades, to material systems with complex chemistry [67].

3.1 Numerical Method

3.1.1 Introduction

The following formulation was developed to model general reacting systems, although it has been validated only for detonation modeling in H, C, N, O, explosives. The detonation phenomena of interest are modeled in two phases. The first is an adiabatic disassociation phase in which the energetic material detonates under NVE conditions. In the second phase, the system is thermostatted to a designated temperature, which leads to recombination.

3.1.2 Stored Energy Functions

The atomic scale kinetic energy is the sum of the translational kinetic energies for each atom

$$T = \sum_{i=1}^{n} \frac{\mathbf{p}^{(i)2}}{2m^{(i)}} \tag{3.1}$$

where '$\mathbf{p}$' is an atomic momentum and 'm' is an atomic mass. There is not any rotational kinetic energy, because each atom is modeled as a point mass.

The potential energy for the ensemble is composed of a wall potential, V^{xyz}, and the potential energy (V^R) due to unbonded (repulsive) interactions

$$V = V^R(\mathbf{c}) + \sum_{i=1}^{n} \left(V_i^{xyz}(\mathbf{c}) \right) \tag{3.2}$$

where '$\mathbf{c}$' is an atomic position vector. The wall potential energy models the repulsive interaction between the atoms and the ensemble boundaries. The wall potential takes the form

$$V_i^{xyz} = V_i^{x_{min}} + V_i^{y_{min}} + V_i^{z_{min}} + V_i^{x_{max}} + V_i^{y_{max}} + V_i^{z_{max}} \tag{3.3}$$

$$V_i^{x_{min}} = 4\,\epsilon_{wall}^{(i)}\, m^{(i)} \left(\frac{\sigma_{wall}}{|x^{(i)} - x_{min}|} - 1 \right)^{n_w} \tag{3.4}$$

$$V_i^{x_{max}} = 4\,\epsilon_{wall}^{(i)}\, m^{(i)} \left(\frac{\sigma_{wall}}{|x^{(i)} - x_{max}|} - 1 \right)^{n_w} \tag{3.5}$$

$$V_i^{y_{min}} = 4\,\epsilon_{wall}^{(i)}\, m^{(i)} \left(\frac{\sigma_{wall}}{|y^{(i)} - y_{min}|} - 1 \right)^{n_w} \tag{3.6}$$

$$V_i^{y_{max}} = 4\,\epsilon_{wall}^{(i)}\, m^{(i)} \left(\frac{\sigma_{wall}}{|y^{(i)} - y_{max}|} - 1 \right)^{n_w} \tag{3.7}$$

$$V_i^{z_{min}} = 4\,\epsilon_{wall}^{(i)}\, m^{(i)} \left(\frac{\sigma_{wall}}{|z^{(i)} - z_{min}|} - 1 \right)^{n_w} \tag{3.8}$$

$$V_i^{z_{max}} = 4\,\epsilon_{wall}^{(i)}\, m^{(i)} \left(\frac{\sigma_{wall}}{|z^{(i)} - z_{max}|} - 1 \right)^{n_w} \tag{3.9}$$

where σ_{wall} and n_w are constants, $x^{(i)}$, $y^{(i)}$, $z^{(i)}$ are the components of the position vector $\mathbf{c}^{(i)}$, and $\epsilon^{(i)}_{wall}$ is an atom type dependent constant with units of energy per unit mass. The repulsive inter-atomic potential used is

$$V_i^R = \sum_{j=1}^{n} \frac{1}{2} k_b^{(ij)} (r^{(ij)} - r_b^{(ij)})^2 \left(\frac{r^{(ij)}}{r_e^{(ij)}} \right)^{-n_b}; \qquad r^{(ij)} \leq r_b^{(ij)} \tag{3.10}$$

where $r^{(ij)}$ is the inter-atomic distance defined by

$$(r^{(ij)})^2 = (\mathbf{c}^{(i)} - \mathbf{c}^{(j)})^2 \tag{3.11}$$

Here r_b is a bond cutoff distance, r_e is an equilibrium bond distance, n_b is an empirical constant (n_b=3), and k_b is the bond stiffness

$$k_b^{(ij)} = \frac{2\, v_b^{(ij)}}{(r_b^{(ij)} - r_e^{(ij)})^2} \tag{3.12}$$

where v_b is a bonding energy. Values for v_b and r_b are determined using Table 3.4 and the relations:

$$v_b^{(ij)} = 0.5\, v_e^{(ij)}\,, \qquad r_b^{(ij)} = 1.5\, r_e^{(ij)} \tag{3.13}$$

3.1.3 State Space Evolution Equations

In this formulation, the evolution equations for the bond order and the entropy are nonholonomic constraints. This section describes the evolution equations for the bond order followed by the evolution equations for the entropy.

3.1.3.1 Bond Order Evolution Equations

The bond order evolution equations unambiguously determine the bonded states in the ensemble, through the use of a rate law (nonholonomic constraint).

Since this formulation, like all RMD formulations, is not ab initio, it contains material specific empirical parameters. The first set of material parameters is an effective valence matrix for the bonded atoms, $\nu_{\alpha\beta}^{bnd}$, where the subscripts α and β refer to atom type. The elements of the effective valence matrix are the number of allowable bonds associated with an atom pair type. The matrix used here for hydrogen, carbon, nitrogen and oxygen is shown in Table 3.1. The second set of material parameters is an unbonded effective valence matrix, $\nu_{\beta\alpha}^{unb}$. The elements of the unbonded effective valence matrix are tunable parameters that weight, in a chemical sense, atom type interactions in order to determine which bond types are generated. The third set of material parameters is a bond type probability matrix, P^{bnd}. The elements of P^{bnd}, determined from published experimental data, are set to the fraction of the atoms (H, C, etc.) associated with each bond type (C-O, N-N, etc..) in the final detonation products. The bond type probability matrix takes the functional form:

$$P_{\alpha\beta}^{bnd} = \Big(\sum_{k=1}^{n_{species}} n_{mol}^{(k)} \, n_{btype}^{(\alpha\beta k)} \Big) (n_{atype}^{(\alpha)})^{-1} \tag{3.14}$$

where $n_{species}$ is the number of unique molecules, $n_{mol}^{(k)}$ is the number of molecules of species 'k', $n_{btype}^{(\alpha\beta k)}$ is the number of bonds that 'α' atoms make with 'β' atoms in species 'k', and $n_{atype}^{(\alpha)}$ is the total number of atoms of type 'α'. Recognizing that the measured detonation products described in published detonation experiments do not in general conserve mass, the experimental data are adjusted (slightly) so as to satisfy stoichiometry. For example, in the experimental data of Ornellas [83] for HMX, the reported percent recovery for each atom type

was: H=104%, C=75.6%, N=97.1% and O=101%. Tables 3.2 and 3.3 compare the composition of the reported experimental end products to the end products estimated by the Kistiakowsky-Wilson rules and the Springall-Roberts rules [2, 88]. It is important to note that of these three material parameter sets, only one ($\nu^{unb}_{\beta\alpha}$) requires computational tuning.

Three more parameter sets are computed from the aforementioned data. The first set are 'bin limits' $e_{\alpha\beta\gamma}$, used to determine bond types (single, double, triple, and 'quadruple' bonds). The subscript γ is a bond type, and hence has a range from one to four. The bin limits are set to a number greater than the maximum number of allowable bonds, unless $\gamma \leq \nu^{ref}_{\alpha}$ and $\gamma \leq \nu^{ref}_{\beta}$ (where $\nu^{ref} = [1, 4, 3, 2]$), in which case

$$e_{\alpha\beta\gamma} = \gamma\, \nu^{bnd}_{\alpha\beta}\, (1 + \nu^{bnd}_{\alpha\beta})^{-1} \tag{3.15}$$

The second and third computed parameter sets, $\omega^{min}_{\alpha\beta}$ and $\omega^{max}_{\alpha\beta}$, are determined from the bond type probability matrix using the formulas

$$\omega^{min}_{\alpha\,1} = 0\,; \quad \alpha = 1, 2...n_a \tag{3.16}$$

$$\omega^{max}_{\alpha\,1} = P^{bnd}_{\alpha\beta}\,; \quad \alpha = 1, 2...n_a \tag{3.17}$$

$$\omega^{min}_{\alpha\beta} = \omega^{max}_{\alpha\gamma}\,; \quad \alpha = 1, 2...n_a\,,\ \beta = 2, 3...n_a, \quad \gamma = \beta - 1 \tag{3.18}$$

$$\omega^{max}_{\alpha\beta} = \omega^{min}_{\alpha\gamma} + P^{bnd}_{\alpha\beta}\,; \quad \alpha = 1, 2...n_a\,,\ \beta = 2, 3...n_a, \quad \gamma = \beta - 1 \tag{3.19}$$

where n_a is the number of atom types. Application of these empirical and computed parameter sets is discussed later in the section.

A bond order B_{ij} is computed for each atom pair, and ranges from zero to one, where zero represents the unbonded state and one represents the fully the bonded state. The bond order is computed by averaging the 'ij' and 'ji' values of the bond state variable b_{ij}

$$B_{ij} = \frac{1}{2}(b_{ij} + b_{ji}) \tag{3.20}$$

The bond state variable is computed from the rate law (nonholonomic constraint)

$$\tau_{ij}\,\dot{b}_{ij} + b_{ij} = b_{ij}^{rhs}(\mathbf{c}, \mathbf{b}) \tag{3.21}$$

where τ_{ij} is a bonding time constant, and b_{ij}^{rhs} is a (normally nonanalytic) function of position and bonded state. The right hide side term b_{ij}^{rhs} term is calculated in a four step process, which follows.

Step One: Bonding weights, w_{ij}, are calculated for all atom pairs. These weights are used in estimating the relative likelihood of bonding between an atom pair, as a function of proximity and current bond state (note the use of Lagrange interpolation):

$$w_{ij} = B_{ij} + (1 - B_{ij}) f(r^{(ij)}) \tag{3.22}$$

where $f(r^{(ij)})$ weights proximity

$$f(r^{(ij)}) = u_s(r_b^{(ij)} - r^{(ij)})\Big(1 - \frac{r^{(ij)}}{r_b^{(ij)}}\Big)\Big(1 - \frac{r_e^{(ij)}}{r_b^{(ij)}}\Big)^{-1} \tag{3.23}$$

and u_s is a step function. The value of the proximity function ranges from zero when $r^{(ij)} = r_b^{(ij)}$ to one when $r^{(ij)} = r_e^{(ij)}$. From the raw weighting functions,

normalized weights are next computed using

$$\hat{w}_{ij} = \frac{w_{ij}}{w_i} \,, \qquad w_i = \sum_{j=1}^{n} w_{ij} \tag{3.24}$$

so long as the summed weight for the atom is greater than zero

$$w_i > 0 \,, \qquad w_j > 0 \tag{3.25}$$

Otherwise the normalized bonding weight is zero.

Step Two: Next an estimated bond order is computed. The estimated bond order, $\hat{b}_{ij}$, a preliminary measure of the bonded state between two atoms, has the functional form

$$\hat{b}_{ij} = \hat{b}^{bnd}_{ij} + \hat{b}^{unb}_{ij} \,, \qquad \hat{b}_{ji} = \hat{b}^{bnd}_{ji} + \hat{b}^{unb}_{ji} \tag{3.26}$$

where $\hat{b}^{bnd}$ and $\hat{b}^{unb}$ account for currently bonded and currently unbonded contributions respectively. The bonded contribution is a function of the bonded effective valence matrix (ν^{bnd}) and takes the form

$$\hat{b}^{bnd}_{ij} = B_{ij}\, \nu^{bnd}_{\alpha\beta}\, \hat{w}_{ij} \,, \qquad \hat{b}^{bnd}_{ji} = B_{ij}\, \nu^{bnd}_{\beta\alpha}\, \hat{w}_{ji} \tag{3.27}$$

The unbonded contribution to the estimated bond order is used to determine which new bonds are formed. At the beginning of a simulation, each atom is assigned a random number, 'R', which falls between zero and one. When the separation distance for two atoms falls within their bond cutoff distance, the 'R' values for those atoms are used to determine whether or not those atoms are allowed to bond. Specifically, if the random numbers for the atoms satisfy

$$\omega^{min}_{\alpha\beta} \leq R_i < \omega^{max}_{\alpha\beta} \quad \text{and} \quad \omega^{min}_{\beta\alpha} \leq R_j < \omega^{max}_{\beta\alpha} \tag{3.28}$$

then the unbonded contribution to the estimated bond order is nonzero, and is computed from

$$\hat{b}_{ij}^{unb} = (1 - B_{ij})\, \nu_{\alpha\beta}^{unb}\, \hat{w}_{ij} \tag{3.29}$$

$$\hat{b}_{ji}^{unb} = (1 - B_{ij})\, \nu_{\beta\alpha}^{unb}\, \hat{w}_{ji} \tag{3.30}$$

Step Three: This step generates an initial value for b_{ij}^{rhs}. The bin limits ($e_{\alpha\beta\gamma}$) and the estimated bond orders are used to compute b_{ij}^{rhs} and the bond type b_{ij}^{typ}, using the following pseudo-code:

if $\hat{b}_{ij} \geq e_{\alpha\beta 4}$ and $\hat{b}_{ji} \geq e_{\beta\alpha 4}$ then $b_{ij}^{rhs} = 1$ and $b_{ij}^{typ} = 4$

else if $\hat{b}_{ij} \geq e_{\alpha\beta 3}$ and $\hat{b}_{ji} \geq e_{\beta\alpha 3}$ then $b_{ij}^{rhs} = 1$ and $b_{ij}^{typ} = 3$

else if $\hat{b}_{ij} \geq e_{\alpha\beta 2}$ and $\hat{b}_{ji} \geq e_{\beta\alpha 2}$ then $b_{ij}^{rhs} = 1$ and $b_{ij}^{typ} = 2$

else if $\hat{b}_{ij} \geq e_{\alpha\beta 1}$ and $\hat{b}_{ji} \geq e_{\beta\alpha 1}$ then $b_{ij}^{rhs} = 1$ and $b_{ij}^{typ} = 1$

else $b_{ij}^{rhs} = 0$ and $b_{ij}^{typ} = 0$

Step Four: The final step is an over coordination check, which ensures that no atom has more than its allowable number of bonds. The coordination of an atom, n^b, is computed as

$$n_i^b = \sum_{j=1}^{n} b_{ij}^{typ} \tag{3.31}$$

If the value of n^b for atom 'i' is great than the number of allowable bonds associated with the atom type, then all associated b_{ij}^{rhs} are set to zero.

3.1.3.2 Entropy Evolution Equations

The evolution equation for the ensemble entropy is (the nonholonomic constraint)

$$\dot{S} = \dot{S}^{rea} + \dot{S}^{vis} + \dot{S}^{con} \tag{3.32}$$

where $\dot{S}^{rea}$ is an entropy flow due to bonding-debonding, $\dot{S}^{vis}$ is an irreversible entropy flow associated with viscous dissipation, and $\dot{S}^{con}$ is an imposed conduction entropy flow rate.

The entropy flow associated with bonding-debonding is

$$\dot{S}^{rea} = -\frac{1}{\theta}\,\mathbf{f}^{rea\,T}\dot{\mathbf{c}} \tag{3.33}$$

where θ is the ensemble kinetic temperature

$$\theta = \sum_{i=1}^{n} \frac{2}{3}\frac{1}{n\,k_B}\Big(\frac{1}{2}\mathbf{p}^{(i)\,T}\dot{\mathbf{c}}^{(i)}\Big) \tag{3.34}$$

with 'n' the number of atoms and k_B Boltzmann's constant. The components of the global force vector $\mathbf{f}^{rea}$ are due to bonding-debonding of the atoms

$$\mathbf{f}^{rea\,(ij)} = B_{ij}\,(\mathbf{f}^{AR\,(ij)} - \mathbf{f}^{R\,(ij)}) \tag{3.35}$$

where $\mathbf{f}^{AR}$ is an attractive-repulsive force representing the interaction of a bonded atom pair, and $\mathbf{f}^{R}$ is a repulsive force representing the interaction of an unbonded atom pair ($\frac{\partial V^R}{\partial r}$). Differentiating the aforementioned repulsive potential,

$$\mathbf{f}^{R\,(ij)} = \Big[k_b\,(r^{(ij)} - r_b^{(ij)})\Big(\frac{r^{(ij)}}{r_e^{(ij)}}\Big)^{-n_b} - \frac{1}{2}k_b^{(ij)}(r^{(ij)} - r_b^{(ij)})^2 \Big(\frac{n_b}{r_e^{(ij)}}\Big)\Big(\frac{r^{(ij)}}{r_e^{(ij)}}\Big)^{-n_b-1}\Big]\Big(\frac{\mathbf{c}^{(i)} - \mathbf{c}^{(j)}}{r^{(ij)}}\Big);\quad r^{(ij)} \le r_b^{(ij)} \tag{3.36}$$

The expression for the attractive-repulsive force depends on the atomic separation distances. When the inter-atomic distance is less than the equilibrium distance, the attractive-repulsive force is

$$\mathbf{f}^{AR\,(ij)} = \Big(1 - \frac{r^{(ij)}}{r_e^{(ij)}}\Big)\,\mathbf{f}^{R\,(ij)} - \Big(\frac{r^{(ij)}}{r_e^{(ij)}}\Big) \\ [-k_e^{(ij)}(r^{(ij)} - r_e^{(ij)})]\Big(\frac{\mathbf{c}^{(i)} - \mathbf{c}^{(j)}}{r^{(ij)}}\Big);\quad r^{(ij)} < r_e^{(ij)} \tag{3.37}$$

When the inter-atomic distance is between the equilibrium and the bonding cutoff distance,

$$\mathbf{f}^{AR\,(ij)} \;=\; \Big\{k_e^{(ij)}(r^{(ij)} \,-\, r_e^{(ij)})\Big\}\Big(\frac{\mathbf{c}^{(i)} - \mathbf{c}^{(j)}}{r^{(ij)}}\Big);\quad r_e^{(ij)} \;\leq\; r^{(ij)} \;<\; r_b^{(ij)} \tag{3.38}$$

where k_e is an equilibrium bond stiffness parameter defined as

$$k_e^{(ij)} = \frac{2v_e^{bnd\,(ij)}}{(r_b^{(ij)} - r_e^{(ij)})^2} \tag{3.39}$$

and v_e^{bnd} is the equilibrium bonding energy

$$v_e^{bnd\,(ij)} = v_e^{(ij)}\, max(1,\, 0.5 + 0.5\, b_{ij}^{typ}) \tag{3.40}$$

which depends on the bond type. Values for v_e and r_e, obtained from the literature [4, 26] for H, C, N, O systems, are shown in Table 3.4.

The irreversible entropy generation rate due to viscous effects is

$$\dot{S}^{vis} = -\frac{1}{\theta}\,\mathbf{f}^{vis\,T}\dot{\mathbf{c}} \tag{3.41}$$

where the global force vector $\mathbf{f}^{vis}$ is obtained from

$$\mathbf{f}^{vis\,(i)} = -\Big[u_s(t - t_{beg}) - u_s(t - t_{end})\Big]\;\sum_{j=1}^{n}\nu\,(\dot{\mathbf{c}}^{(i)} - \dot{\mathbf{c}}^{(j)}) \tag{3.42}$$

and ν is a damping coefficient. The step functions limit the application of the viscous forces to the time range, t_{beg} to t_{end}, over which the thermostat is applied. These forces allow for very fast cooling rates (on the order or 10^{14} K/s) when the thermostat is applied.

An imposed entropy conduction is used to control the ensemble kinetic temperature and has the functional form:

$$\dot{S}^{con}(\theta, t) = \Big[u_s(t - t_{beg}) - u_s(t - t_{end})\Big]\, \dot{S}_o\, min\Big[1, \frac{\theta}{max(\theta_o, \theta_{therm})} - 1\Big] \quad (3.43)$$

where $\dot{S}_o$ is a specified constant, θ_o is the minimum allowable system temperature, and the desired system temperature is θ_{therm}.

3.1.4 Power Input and Output

The power into and out of the system is due to the imposed conduction entropy flow and has the form

$$P = -\theta \dot{S}^{con} \quad (3.44)$$

Combining equations 3.32, 3.33, 3.41 and 3.44 the net power flow to the system is

$$P = -\Big(\theta\, \dot{S} + \mathbf{f}^{rea\,T} \dot{\mathbf{c}} + \mathbf{f}^{vis\,T} \dot{\mathbf{c}}\Big) \quad (3.45)$$

Recalling the definition for kinetic temperature, define a vector '$\mathbf{g}$' such that

$$\theta = \mathbf{g}^T\, \dot{\mathbf{c}}\,, \qquad \mathbf{g}^{(i)} = \frac{\mathbf{p}^{(i)}}{3\, n\, k_B} \quad (3.46)$$

Combining equations 3.46 and 3.45, note that all terms in the net power flow expression are proportional to the global generalized velocity vector $\dot{\mathbf{c}}$

$$P = -\left[(\dot{S}\mathbf{g})^T \, \dot{\mathbf{c}} \; + \mathbf{f}^{rea\,T} \dot{\mathbf{c}} + \mathbf{f}^{vis\,T} \dot{\mathbf{c}} \right] \tag{3.47}$$

3.1.5 Canonical Hamilton's Equations

The ensemble Hamiltonian is the sum of the system's potential and kinetic energy

$$H = T + V \tag{3.48}$$

The canonical Hamilton's equations are

$$\dot{\mathbf{p}}^{(i)} = -\frac{\partial H}{\partial \mathbf{c}^{(i)}} + \mathbf{q}^{nc\,(i)} \tag{3.49}$$

$$\dot{\mathbf{c}}^{(i)} = \frac{\partial H}{\partial \mathbf{p}^{(i)}} = \frac{\mathbf{p}^{(i)}}{m^{(i)}} \tag{3.50}$$

$$0 = -\frac{\partial H}{\partial b_{ij}} + q^{b_{ij}} \tag{3.51}$$

$$0 = -\frac{\partial H}{\partial S} + q^{S} \tag{3.52}$$

where $\mathbf{q}^{nc\,(i)}$, q^s, $q^{b_{ij}}$ are generalized nonconservative forces determined by the net power flow and the nonholonomic constraints. Equations 3.51 and 3.52 are 'degenerate' Hamilton's equations, since there are no generalized momenta associated with the corresponding generalized coordinates.

3.1.6 Generalized Forces

The generalized conservative forces obtained from the potential energy are

$$\frac{\partial H}{\partial \mathbf{c}^{(i)}} = \mathbf{f}^{R\,(i)} \tag{3.53}$$

The generalized nonconservative forces $\mathbf{f}^{gen}$ due to the net power flow are

$$\mathbf{f}^{gen} = -\dot{S}\mathbf{g} - \mathbf{f}^{rea} - \mathbf{f}^{vis} \tag{3.54}$$

In order to determine the nonconservative forces due to the nonholonomic constraints, Lagrange multipliers ($\lambda^{b_{ij}}$ and λ^{S}) are introduced for the bond order evolution and entropy evolution relations

$$\lambda^{b_{ij}}\Big[\tau_{ij}\,\dot{b}_{ij} + b_{ij} - b_{ij}^{rhs}(\mathbf{c},\mathbf{b})\Big] = 0 \tag{3.55}$$

$$\lambda^{S}\Big[\dot{S} + \frac{1}{\theta}\,\mathbf{f}^{rea\,T}\dot{\mathbf{c}} + \frac{1}{\theta}\,\mathbf{f}^{vis\,T}\dot{\mathbf{c}} - \dot{S}^{con}\Big] = 0 \tag{3.56}$$

The nonconservative forces are equal to the coefficients of the generalized velocities in the constraints. Therefore

$$q^{b_{ij}} = \lambda^{b_{ij}}\,\tau_{ij}, \qquad q^{S} = \lambda^{S}\,, \qquad \mathbf{q}_{S}^{nc\,(i)} = \frac{\lambda^{S}}{\theta}\mathbf{f}^{rea(i)} + \frac{\lambda^{S}}{\theta}\mathbf{f}^{vis(i)} \tag{3.57}$$

where $\mathbf{q}_{S}^{nc\,(i)}$ are nonconservative forces due to the entropy evolution relation. The degenerate Hamilton's equations allow the Lagrange multipliers to be determined in closed form (using equations 3.51 and 3.52)

$$\frac{\partial H}{\partial b_{ij}} = 0 \quad \rightarrow \quad q^{b_{ij}} = 0 \quad \rightarrow \quad \lambda^{b_{ij}} = 0 \tag{3.58}$$

$$\frac{\partial H}{\partial S} = 0 \quad \rightarrow \quad q^{S} = 0 \quad \rightarrow \quad \lambda^{S} = 0 \tag{3.59}$$

so that finally

$$\mathbf{q}_S^{nc\,(i)} = \frac{\lambda^S}{\theta}\mathbf{f}^{rea(i)} + \frac{\lambda^S}{\theta}\mathbf{f}^{vis(i)} = \mathbf{0} \tag{3.60}$$

As a result the nonconservative generalized forces in the momentum balance equations are

$$\mathbf{q}^{nc\,(i)} = \mathbf{f}^{gen\,(i)} = -\dot{S}\mathbf{g}^{(i)} - \mathbf{f}^{rea\,(i)} - \mathbf{f}^{vis\,(i)} \tag{3.61}$$

3.1.7 Final Hamilton's Equations

The final Hamilton's equations for the ensemble are

$$\dot{\mathbf{c}}^{(i)} = \frac{\mathbf{p}^{(i)}}{m^{(i)}} \tag{3.62}$$

$$\dot{\mathbf{p}}^{(i)} = -\mathbf{f}^{R\,(i)} - \dot{S}\mathbf{g}^{(i)} - \mathbf{f}^{rea\,(i)} - \mathbf{f}^{vis\,(i)} \tag{3.63}$$

and are augmented by the nonholonomic constraints. Note that

$$\dot{\mathbf{p}}^{(i)} = -\mathbf{f}^{R\,(i)} - \dot{S}\mathbf{g}^{(i)} - \mathbf{f}^{vis\,(i)} - \sum_{j=1}^{n} B_{ij}\left(\mathbf{f}^{AR\,(ij)} - \mathbf{f}^{R\,(ij)}\right) \tag{3.64}$$

so that when the bond order for the 'ij'th pair is equal to one (bonded), the two terms which depend only on the repulsive potential cancel.

3.1.8 Discussion

A rate law description of the bonding-debonding process has several advantages over the holonomic formulations used in previous work. First, it allows for nonanalytic functions to be used in describing the physical chemistry. Second, it explicitly represents the chemical kinetics, whereas in previous work bonding and debonding is inferred from position or velocity dependent

functions. Third, it allows for a simple, energy conserving treatment of over-coordination. As will be seen in the simulations, the formulation does not exhibit the large atom 'clusters' reported in previous work [41].

Note that a global thermostatic force, $\mathbf{f}^s$, defined by

$$\theta \dot{S} = \mathbf{f}^{s\,T} \dot{\mathbf{c}} \tag{3.65}$$

may be used to provide a physical interpretation of the entropy flow variable introduced in the calculation. Since

$$(\mathbf{g}^T \dot{\mathbf{c}}) \dot{S} = \mathbf{f}^{s\,T} \dot{\mathbf{c}}\,, \qquad (\dot{S}\mathbf{g})^T \dot{\mathbf{c}} = \mathbf{f}^{s\,T} \dot{\mathbf{c}}\,, \qquad (\mathbf{f}^s - \dot{S}\mathbf{g})^T \dot{\mathbf{c}} = 0 \tag{3.66}$$

the thermostatic force $\dot{S}\mathbf{g}$ is required in order to conserve energy. The functional form of the Berendesen thermostat [51] is imbedded as a very special case

$$\mathbf{f}^{rea} = \mathbf{0}\,, \quad \mathbf{f}^{vis} = \mathbf{0}\,, \quad \dot{S} = 3\,n\,k_b\,\zeta\,, \quad \mathbf{f}^{gen} = -\dot{S}\,\mathbf{g} = -\zeta \mathbf{p} \tag{3.67}$$

where ζ is a empirical constant or function used for temperature control. This temperature control strategy employed in this research is characterized as a weak boundary condition, since the ensemble temperature is allowed to vary from the specified thermostat temperature [51].

The state space model for the system was integrated using a second order Runge-Kutta method, and a constant time step of 0.01 fs. All simulations were performed using a bond order time constant of 0.1 ps for all bond types.

3.2 Chemical Kinetics Modeling

In a chemically reactive system there may be multiple parallel (competitive) and consecutive reactions. To form the chemical kinetics model for such a system, contributions from each reaction are summed for each species [54]

$$\frac{dC_i}{dt} = \sum_{j=1}^{N} \left[(\nu^{(i,j)} - \hat{\nu}^{(i,j)}) k_f^j \prod_{s=1}^{n} (C_s)^{\alpha_f^{(s,j)}} + (\hat{\nu}^{(i,j)} - \nu^{(i,j)}) k_r^j \prod_{s=1}^{n} (C_s)^{\alpha_r^{(s,j)}} \right] \quad (3.68)$$

where k_f and k_r are reaction rate coefficients, α_f and α_r are concentration exponents (sometimes called reaction orders [86]), the subscripts 'f' and 'r' denote forward and reverse reactions, 'i' and 's' are species indices, 'j' is a reaction index, $\hat{\nu}$ and ν terms are the stoichiometric coefficients of the reactants and products respectively, and C_i is a species concentration. In this model, the k and α values are determined from experimental data [86]. The 'k' values often use the temperature dependent form

$$k = AT^b exp\Big(\frac{-E_a}{RT}\Big) \quad (3.69)$$

where 'A' and 'b' are reaction constants, E_a is an activation energy, 'R' is the universal gas constant and 'T' is the temperature. The 'AT^b' term is called the Boltzman factor, and is intended to account for collision frequency in the system [54].

In this research, two distinct kinetics models are formulated to represent the chemistry represented in the NVE and NVT stages of the RMD simulation. The modeled chemical reactions are inferred from the time variation of the chemical species observed during the simulation.

3.2.1 Detonation Chemistry Model

The detonation chemistry model is used to represent adiabatic kinetics in the NVE ensemble. The detonation chemistry model takes the form

$$\frac{dC_i}{dt} = \sum_{j=1}^{N} \left(\nu^{(i,j)} - \hat{\nu}^{(i,j)}\right)\zeta^{(j)}, \quad \zeta^{(j)} = \left(\frac{\rho}{\rho_o}\right)^{1-m^{(j)}} k^{(j)} \prod_{s=1}^{n} C_s^{\alpha^{(s,j)}} \tag{3.70}$$

where C_s is species concentration (in moles per centimeter cubed), N is the number of reactions, $\nu^{(i,j)}$ and $\hat{\nu}^{(i,j)}$ are the stoichiometric coefficients of the products and reactants for species 'i' in reaction 'j', $\zeta^{(j)}$ are the reaction rates, ρ is the mixture density, ρ_o is a reference density, $k^{(j)}$ are rate coefficients, 's' is a species index, the $\alpha^{(s,j)}$ are concentration exponents, 'n' is the number of species, and $m^{(j)}$ is the over all reaction order defined as

$$m^{(j)} = \sum_{s=1}^{n} \alpha^{(s,j)} \tag{3.71}$$

This kinetics model differs from equation 3.68 in three details: (1) there are assumed to be no reverse reactions ($k_r = 0$), (2) there is a density correction, for application at higher scales, and (3) the adiabatic reaction rate coefficients are assumed to be temperature independent. The reaction rate coefficients and the concentration exponents will be fit to the RMD simulation data. A variable transformation for the detonation chemistry model is discussed in Appendix A.2.

3.2.2 Recombination Chemistry Model

The recombination chemistry model is a temperature dependent model used to represent the thermostatted portion of the RMD simulation data.

Temperature is taken as the independent variable, to facilitate integration of the model into reacting shock simulations preformed at higher scales. The model takes the form

$$\frac{dC_i}{d\theta_H} = \sum_{j=1}^{N} \left(\nu^{(i,j)} - \hat{\nu}^{(i,j)}\right)\zeta^{(j)}, \quad \zeta^{(j)} = \left(\frac{\rho}{\rho_o}\right)^{1-m^{(j)}} k^{(j)} \theta_H^{\gamma^{(j)}} \prod_{s=1}^{n} C_s^{\alpha(s,j)} \tag{3.72}$$

where θ_H is the homologous temperature, defined as

$$\theta_H = \frac{\theta_{max} - \theta}{\theta_{max} - \theta_{min}} \tag{3.73}$$

Note that the concentration exponents are assumed to have a value of one if species 's' corresponds to a reactant in reaction 'j'. The reaction rate coefficients and the homologous temperature exponents $\gamma^{(j)}$ will be fit to the RMD simulation data. A variable transformation for the recombination chemistry model is discussed in Appendix A.3.

A time dependent recombination chemistry model can be represented using the chain rule

$$\frac{dC}{dt} = \left(\frac{dC}{d\theta_H}\right)\left(\frac{d\theta_H}{d\theta}\right)\left(\frac{d\theta}{dt}\right) \tag{3.74}$$

where $\frac{d\theta_H}{d\theta}$ and $\frac{d\theta}{dt}$ may come from an RMD simulation or higher scale models. Transient models of this type are presented in Appendix B, for HMX and RDX, where $\frac{d\theta_H}{d\theta}$ and $\frac{d\theta}{dt}$ are obtained from an RMD simulation.

3.2.3 Density Correlation

In both the NVE and the NVT ensemble simulations, the ensemble density remains constant as neither the volume nor the atom collection in the

simulation are changing. Thus, the RMD simulation results do not directly account for density dependent kinetics effects. A density correlation factor, $(\frac{\rho}{\rho_o})^{1-m}$, may be used to specify that the production rate of each species will vary directly with mixture density. The density correlation factor is determined as follows. If a density dependence is introduced in both the concentration variables and the reaction rate expression then

$$C_s = C'_s \frac{\rho}{\rho_o} , \qquad \zeta^{(j)} = \left(\frac{\rho}{\rho_o}\right)^{\xi^{(j)}} k^{(j)} \prod_{s=1}^{n} \left(\frac{\rho}{\rho_o} C'_s\right)^{\alpha^{(s,j)}} \tag{3.75}$$

where C'_s is a concentration for species 's' at the mixture reference density. Rearranging

$$\zeta^{(j)} = \left(\frac{\rho}{\rho_o}\right)^{\xi^{(j)}+m^{(j)}} k^{(j)} \prod_{s=1}^{n} (C'_s)^{\alpha^{(s,j)}} \tag{3.76}$$

To maintain a direct proportionality between the species production rate and mixture density, the exponent of $\frac{\rho}{\rho_o}$ must equal 1, therefore

$$\xi^{(j)} + m^{(j)} = 1 , \qquad \xi^{(j)} = 1 - m^{(j)} \tag{3.77}$$

3.2.4 Fitting Chemistry Model Parameters

To fit the parameters in the detonation and recombination chemistry models to the RMD data, this research employed Matlab's fmincon routine [71] to minimize the objective function

$$O_b = \sum_{i=1}^{n_s} \sum_{t=1}^{n_t} w_s^{(i)} (C_{sim}^{(it)} - C_{fit}^{(it)})^2 \tag{3.78}$$

where n_s is the number of species in the kinetics model, n_t is the number of time steps in the simulation data, $w_s^{(i)}$ is a species weighting factor, $C_{sim}^{(it)}$ and

$C_{fit}^{(it)}$ are the concentrations of species 'i' at the time corresponding to time step 't' for the RMD simulation and for the kinetic model fit respectively. Matlab applies a least squares fit to minimize the weighted difference between the RMD concentration data and the concentrations produced by integration of the chemical kinetics model.

3.3 Validation Simulations

The general RMD formulation described in this chapter was validated by simulating detonation in perfect crystals of β-HMX and α-RDX, then comparing the predicted energy release and detonation products to corresponding experimental values. Single molecules of β-HMX and α-RDX are shown in Figure 3.1 and 3.2 respectively. All subsequent figures displaying HMX or RDX simulation results use the same color legend shown in these figures. The following two stage simulation procedure was used to model detonation and recombination processes in the energetic materials of interest. The first stage has a 50 ps duration, and simulates impact of an energetic crystal on an ensemble wall at 3 km/s, under NVE conditions. Upon impact, the energetic material detonates and dissociates into high temperature intermediate species. The energy release, $E_{release}$, for the explosive is calculated as the difference between the initial kinetic energy, $T_{initial}$, and the steady state NVE kinetic energy, T_{NVE} observed in the simulation

$$E_{release} = T_{NVE} - T_{initial} \tag{3.79}$$

Reaction mechanisms and parameters for the detonation kinetics model are obtained from this 'NVE' stage of the simulation.

The second stage of the simulation extends from 50 to 150 ps after impact; over the course of this simulation, the system is gradually thermostatted to 500 K. This allows the high temperature intermediates to recombine into the final detonation products. Thermostatting the ensemble approximates the process of heat removal from the detonation products by the water jacket in a bomb calorimeter experiment. By 150 picoseconds after impact, the final detonation products have reached steady state, and can be compared to those described in published experiments. Reaction mechanisms and parameters for the recombination kinetics model are obtained from this 'NVT' stage of the simulation.

The following sections describe the detonation simulations performed for HMX and RDX. First, the initial set up is presented, including material specific input parameters and the initial crystal configuration. Second, the simulations results are presented and compared to experiment, for both energy release and long time detonation products. Third, detonation and recombination kinetics models are presented, including plots comparing the RMD simulation data to the fitted kinetics models.

3.3.1 Simulation of Detonation in β-HMX

The material specific parameter matrices used to represented HMX are provided in Table 3.5 ($\nu_{\alpha,\beta}^{unb}$), Table 3.7 ($\omega_{\alpha,\beta}^{min}$), and Table 3.8 ($\omega_{\alpha,\beta}^{max}$). The

bond type probability matrix and the species mole ratio data used to create it are provided in Tables 3.6 and 3.9 respectively.

The atomic coordinates for the initial configuration of the β-HMX crystal were taken from neutron diffraction experiments described by Choi [25]. The unit cell for β-HMX contains two molecules (z=2), so in order to create larger crystals of HMX for the simulations, a preprocessing code was written in Matlab. The latter code uses atomic coordinates from Choi's experiments as well as the space group of β-HMX, $P2_1/c$, to replicate a unit cell. The unit cell for HMX is shown in Figure 3.3. The simulation procedure described in the introduction section of this chapter is used to simulate HMX detonation for crystals containing eight, sixteen, thirty-two, and sixty-four molecules. The HMX crystal containing sixty-four molecules is shown in Figure 3.4. Simulating four model sizes allows for a convergence analysis, comparing the species concentrations reached at the end of NVE simulation and the end of the NVT simulation. Fitted kinetics model parameters are also compared, as a function of model resolution. Figure 3.6 shows the changes in kinetic, potential, and total energy versus time for the sixty-four molecule detonation simulation. The total energy plot in that figure verifies energy conservation during the NVE simulation. Comparing the change in kinetic energy at detonation to the experimentally predicted energy release (dashed line) shows good agreement with experiment. The error between the experimental and simulated energy release is

$$\epsilon = \frac{|E^{sim}_{release} - E^{exp}_{release}|}{E^{exp}_{release}} \tag{3.80}$$

where $E^{sim}_{release}$ is the simulated energy release and $E^{exp}_{release}$ is the experimental energy release. The computed energy release shows small fluctuations during the simulation, so values over the period 30-50 ps are averaged to produce a representative energy release. The simulated energy release and the error in the simulated energy release are shown in Tables 3.13 and 3.14. The experimental error bars reported by Ornellas [83] indicate an uncertainty of 0.15 eV per molecule in the measured energy release for HMX. The steady state species concentrations for the NVE stage of the simulation are provided in Table 3.10. These species concentrations are calculated by averaging the individual species concentrations computed over the 30-50 ps (steady state) time interval. A snapshot made during the steady state portion of the NVE stage of the simulation is provided in Figure 3.5. Note that many of the atoms are not bonded, and that diatomic species are prominent at the high temperature. Computed species concentrations versus time for the NVE stage of the simulation are shown in Figures 3.7 and 3.8.

At 50 picoseconds after impact the thermostat is turned on, removing energy from the system. This is indicated by the decline in total energy shown in Figure 3.6. The NVT simulation reaches steady state at approximately 120 picoseconds, after which the final detonation products do not change significantly. A plot of the ensemble temperature during the simulation is shown in Figure 3.9. A snapshot of the simulation results at 129 ps is shown in Figure 3.24. Comparing Figure 3.5 with Figure 3.24, it is evident that many new bonds have been formed and that larger molecules, including CO_2 and H_2O,

are much more numerous. This point is further illustrated by Figure 3.25, which shows a zoomed view of the simulation results at 129 picoseconds. The zoomed view makes individual molecules and their bond types visible (light gray is a single bond, medium gray is a double bond, and dark gray is a triple bond). Computed species concentrations versus time for the NVT stage of the simulation are shown in Figures 3.26 and 3.27. These plots show that during the thermostatted stage of the simulation, the concentrations of unbonded atoms drop while the concentrations of the final end products increase. The computed detonation products are compared to published experimental data in Table 3.11, for each model size. The table includes all species with an experimental mole ratio of 0.2 or greater. Table 3.12 compares the composition of the reported experimental end products, in a stoichiometric sense, to the composition of HMX. In order to quantify how well each simulation compares with experiment, an error value, ϵ, is calculated using

$$\epsilon = \left(\sum_{i=1}^{n} w_i^{\epsilon} \frac{|M_{sim}^{(i)} - M_{exp}^{(i)}|}{M_{exp}^{(i)}} \right) \left(\sum_{i=1}^{n} w_i^{\epsilon} \right)^{-1} \tag{3.81}$$

Here $M_{sim}^{(i)}$ and $M_{exp}^{(i)}$ are product to reactant mole ratios obtained from the simulation and from the experiment, and the parameters w_i^{ϵ} are species weighting factors. The error between the experimental and the simulated final detonation products (with weighting factors equal to the mole ratio of the experimental products) is shown in Table 3.15, as a function of model size. Agreement with experiment improves with larger models.

3.3.2 Reaction Mechanisms and Kinetics Models for β-HMX

Reaction mechanisms for the adiabatic detonation process are inferred from the NVE portion of the simulation, and are provided in Table 3.16. The first reaction models the dissociation of the HMX molecule. Scission of NO_2 from the explosive molecule has been predicted as an initial step in several other decomposition models for HMX [119, 126]. Reactions two through four model the formation of high temperature intermediates and some long term detonation products. Species indices as well as initial and final mole ratios for the NVE stage of the simulation are shown in Table 3.17. The stoichemetric coefficients $\nu^{(i,j)}$ and $\hat{\nu}^{(i,j)}$ for the NVE stage reaction mechanisms in HMX are provided in Tables 3.18 and 3.19.

The detonation and recombination kinetics models for β-HMX take the form shown in section 3.2. The reaction rate coefficients and concentration exponents for the NVE stage of the simulation, fit using the procedure outlined in section 3.2.4, are listed in Tables 3.20 and 3.21. Note that all $\alpha^{(s,j)}$ values which do not appear in the table are equal to zero. The RMD simulation data and the kinetics model fit for the NVE stage of the simulation are compared in Figures 3.10 through 3.23. These plots show that the detonation kinetics model is able to reproduce the RMD species concentrations data obtained in the NVE portion of the HMX simulation.

Reaction mechanisms for the recombination process in HMX are inferred from the thermostatted (NVT) portion of the simulation, and are shown in Table 3.22. These reactions describe recombination of the high temperature

intermediates developed in the first stage of the simulation, and reproduce the end product species observed in bomb calorimeter experiments. The recombination reactions are more complex than those which describe the adiabatic detonation process, due to the presence of competitive reactions. For example reactions 1 and 5 both compete for oxygen. Species indices as well as the initial and final mole ratios for the recombination reaction mechanisms in HMX are provided in Table 3.23. Note that the final state of the detonation (NVE) reactions are taken as the initial state of the recombination (NVT) reactions. The stoichemetric coefficients $\nu^{(i,j)}$ and $\hat{\nu}^{(i,j)}$ for the NVT stage reaction mechanisms in HMX are provided in Tables 3.25 and 3.26 respectively.

The reaction rate coefficients, homologous temperature exponents, and concentration exponents for the NVT stage of the simulation are listed in Tables 3.24 and 3.27. The RMD simulation data and the kinetics model fit for the NVT stage of the simulation are compared in Figures 3.28 through 3.39. They show good agreement between the kinetics model and the RMD simulation data. Plots indicating the variation of the fitted kinetic model parameters with model size are shown in Figures 3.40 through 3.43. The general trend is that the eight molecule model shows the largest deviation from the sixty-four molecule model, and that the two intermediate size models show similar (in magnitude) deviations from the sixty-four molecule.

3.3.3 Simulation of Detonation in α-RDX

The atomic configuration for the α-RDX molecule was obtained from published experimental neutron diffraction data [24]. A unit cell for the RDX crystal is shown in Figure 3.44. A preprocessing code written in Matlab was used to replicate the RDX unit cell and produce crystal models containing eight, sixteen, thirty-two and sixty-four molecules. The sixty-four molecule crystal of RDX is shown in Figure 3.45.

The three material specific parameter matrices used in to model RDX are provided in Table 3.28 ($\nu_{\alpha,\beta}^{unb}$), Table 3.30 ($\omega_{\alpha,\beta}^{min}$), and Table 3.31 ($\omega_{\alpha,\beta}^{max}$). The bond type probability matrix and the data used to create it are provided in Tables 3.29 and 3.32 respectively. The two stage simulation procedure described in the introduction of this chapter was used to model the detonation and recombination processes in RDX. Changes in kinetic, potential, and total energy over the course of the simulation for the sixty-four molecule simulation are plotted in Figure 3.47. The simulated energy release at detonation is calculated by averaging the computed energy release values obtained over the time period 30-50 ps (shown in Table 3.36). Differences between the experimental and simulated energy release were compared using the error measure of equation 3.80; the errors are listed in Table 3.37, as a function of model resolution. The experimental error bars reported by Ornellas [83] indicate an uncertainty of 0.15 eV per molecule in the measured energy release for RDX. The steady state species concentrations for the NVE stage of the simulation are listed in Table 3.33, as a function of model size (these are average species concentra-

tions computed over the time period 30-50 ps). The data indicate that the steady state species concentrations do not vary significantly with model size. A snapshot of the simulation at 18.3 ps after impact is shown in Figure 3.46. This figure shows that the steady state products for the NVE stage simulation consist primarily of diatomic species and unbonded atoms. Species concentrations versus time for the NVE stage of the simulation are shown in Figures 3.48 and 3.49.

The variation in temperature over the entire course of the RDX simulation is shown in Figure 3.50. A snapshot of the sixty-four molecule simulation results at 149 ps is shown in Figure 3.65. As in the case of the HMX simulation, the late time NVT portion of the simulation shows few unbonded atoms, with the detonation products composed primarily of H_2O, CO_2, N_2, and CO. Figure 3.66 shows a zoomed in view of the simulation results at 149 picoseconds. In this figure, individual molecules are easily recognized. Evolution of the species concentrations over the course of the NVT stage of the simulation are shown in Figures 3.67 and 3.68. Note that by the end of the NVT stage of the simulation, the concentrations of unbonded atoms are low and the concentrations of the final products show very little fluctuation. Mole ratios for the final detonation products, for each of the four RDX models sizes, are listed in Table 3.34. Table 3.35 compares the composition of the reported experimental end products, in a stoichiometric sense, to the composition of RDX. The error in the simulated end product concentrations, as compared to published experimental data, is calculated using equation 3.81, using weights

equal to the experimental final product mole ratios (shown in Table 3.38). The error values indicate that agreement with experiment improves as model size increases.

3.3.4 Reaction Mechanisms and Kinetics Models for α-RDX

The reaction mechanisms inferred from the NVE portion of the RDX simulation are indicated in Table 3.39. The species indices as well as the starting and ending species mole ratios are provided in Table 3.40. The stoichiometric product and reactant matrices, ν and $\hat{\nu}$, for the NVE reaction mechanisms are provided in Tables 3.41 and 3.42 respectively.

The detonation and recombination kinetics models for α-RDX take the form described in section 3.2. The fitted parameters for the detonation kinetics model in RDX are provided in Tables 3.43 and 3.44. The RMD data for the NVE stage of the RDX simulation is compared to the fitted adiabatic kinetics model in Figures 3.51 through 3.64. These figures demonstrate that the fitted detonation kinetics model is able to reproduce the RMD simulation data.

The recombination reaction mechanisms inferred from the thermostatted (NVT) portion of the RDX simulation are provided in Table 3.45. Species indices as well as the initial and final mole ratios for the recombination chemistry model for RDX are provided in Table 3.46. The stoichiometric matrices ν and $\hat{\nu}$, associated with these recombination reactions are provided in Tables 3.48 and 3.49. The fit parameters and concentration exponents for the recombination kinetics model for RDX are listed in Tables 3.50 and 3.47 respectively.

Species concentration plots comparing the recombination kinetics model with the RMD simulation data are provided in Figures 3.69 through 3.79. These plots show that the recombination kinetics model is able to reproduce the species concentration versus time data produced by the RMD simulation.

Additional plots (Figures 3.80 through 3.83) describe the variation of the fitted kinetic model parameters with model size, for RDX. The general trend is that the eight molecule model shows the largest deviation from the sixty-four molecule model, and that the two intermediate size models show similar (in magnitude) deviations from the sixty-four molecule case.

Table 3.1: Effective valence for bonded atoms ($\nu_{\alpha,\beta}^{bnd}$)

	H	**C**	**N**	**O**
H	1	1	1	1
C	4	4	4	4
N	3	3	3	3
O	2	2	2	2

Table 3.2: Experimental and empirical detonation products: HMX

Species	Exp. [83]	Kistiakowsky-Wilson [2]	Springall-Roberts [2]
N_2	3.68	4	4.00
H_2O	3.18	4	4.00
CO_2	1.92	0	0.67
CO	1.06	4	2.66
$C(s)$	0.97	0	0.67
H_2	0.30	0	0.00
NH_3	0.39	0	0.00
CH_4	0.04	0	0.00
HCN	0.01	0	0.00

Table 3.3: Experimental and empirical detonation products: RDX

Species	Exp. [83]	Kistiakowsky-Wilson [2]	Springall-Roberts [2]
N_2	2.80	3	3.00
H_2O	2.34	3	3.00
CO_2	1.39	0	0.50
CO	1.10	3	2.00
$C(s)$	0.44	0	0.50
H_2	0.34	0	0.00
NH_3	0.03	0	0.00
CH_4	0.04	0	0.00
HCN	0.03	0	0.00

Table 3.4: Equilibrium bond energies and lengths

Bond Type	v_e (eV) [26]	r_e (Å) [4]
H-H	4.481	1.08
H-C	4.257	1.08
H-N	3.999	1.01
H-O	4.773	0.96
C-C	2.867	1.48
C-N	3.053	1.47
C-O	3.698	1.43
N-N	3.239	1.45
N-O	3.075	1.23
O-O	2.559	1.48

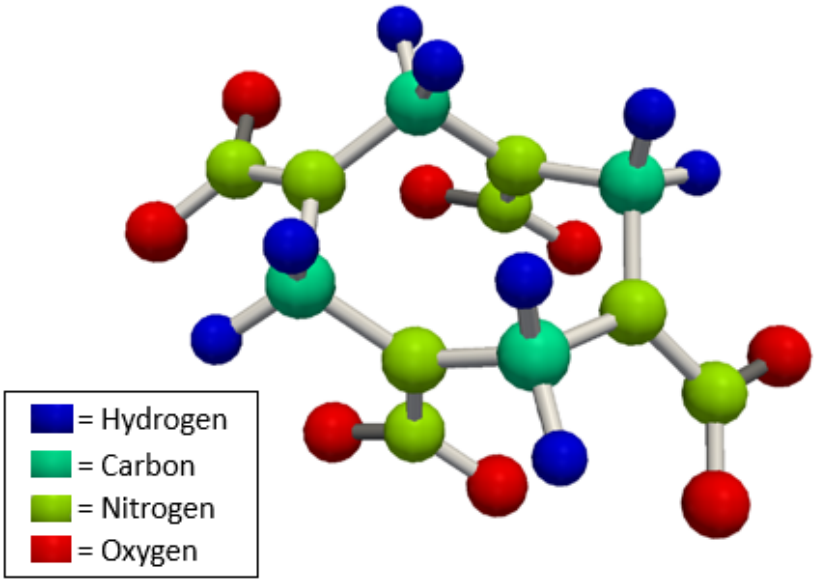

Figure 3.1: Molecule of β-HMX

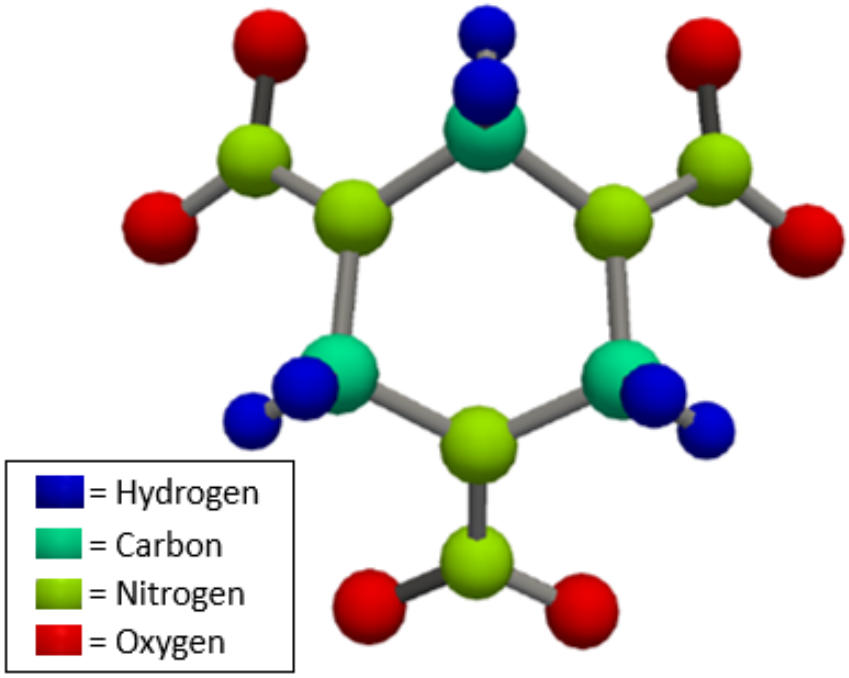

Figure 3.2: Molecule of α-RDX

Table 3.5: Effective valence for unbonded atoms ($\nu^{unb}_{\alpha,\beta}$): HMX

	H	**C**	**N**	**O**
H	1	0	2	2
C	0	1	0	4
N	6	0	1	0
O	4	2	0	0

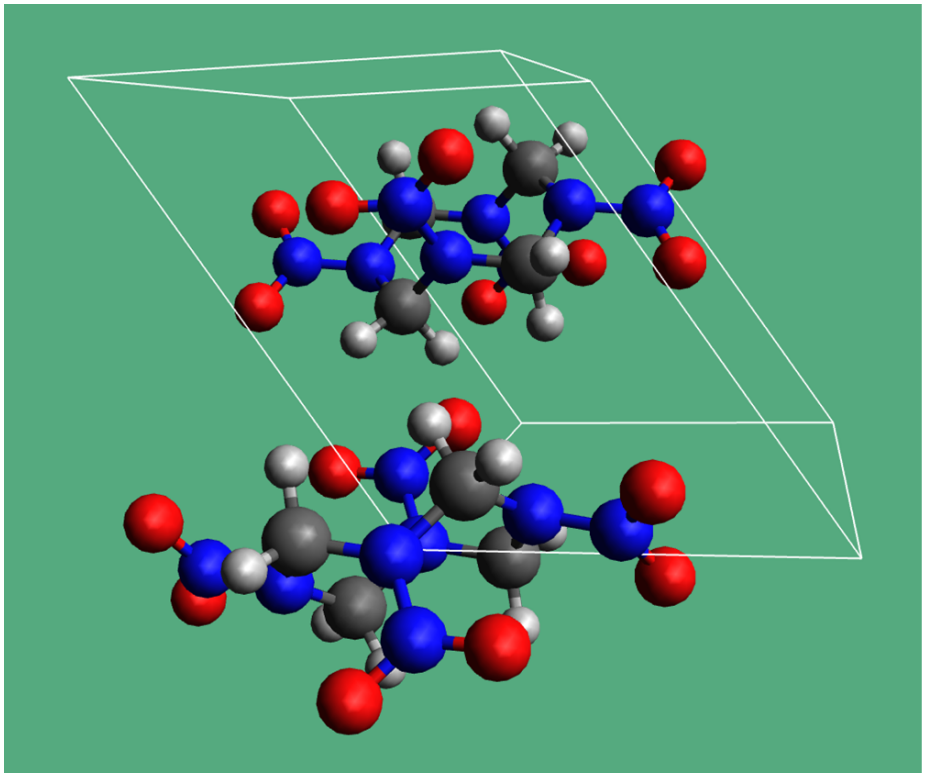

Figure 3.3: Unit cell for β-HMX (light gray is hydrogen, gray is carbon, blue is nitrogen, red is oxygen)

Table 3.6: Bond type probability matrix ($P^{bnd}_{\alpha,\beta}$): HMX

	H	**C**	**N**	**O**
H	0.0625	0.0000	0.1875	0.7500
C	0.0000	0.2500	0.0000	0.7500
N	0.0625	0.0000	0.9375	0.0000
O	0.3750	0.6250	0.0000	0.0000

Table 3.7: Random number minimum matrix ($\omega_{\alpha,\beta}^{min}$): HMX

	H	**C**	**N**	**O**
H	0.0000	0.0625	0.0625	0.2500
C	0.0000	0.0000	0.2500	0.2500
N	0.0000	0.0625	0.0625	1.0000
O	0.0000	0.3750	1.0000	1.0000

Table 3.8: Random number maximum matrix ($\omega_{\alpha,\beta}^{max}$) : HMX

	H	**C**	**N**	**O**
H	0.0625	0.0625	0.2500	1.0000
C	0.0000	0.2500	0.2500	1.0000
N	0.0625	0.0625	1.0000	1.0000
O	0.3750	1.0000	1.0000	1.0000

Table 3.9: Experimental and approximated (atom conservative) detonation products: HMX

Species	N_2	H_2O	CO_2	CO	$C(s)$	H_2	NH_3	CH_4	HCN
Exp. [83]	3.68	3.18	1.92	1.06	0.97	.30	.39	.039	.008
App.	3.75	3.00	2.00	1.00	1.00	.25	.50	0.00	0.00

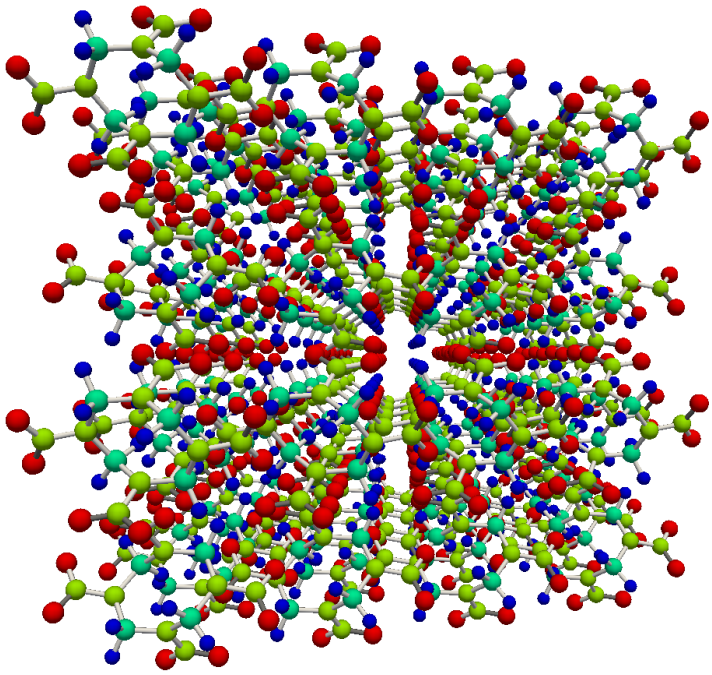

Figure 3.4: Sixty-four molecule crystal of β-HMX

Table 3.10: Steady state species concentrations (NVE): HMX

Species	8 Molecules	16 Molecules	32 Molecules	64 Molecules
N_2	1.1464	2.1864	1.8403	1.7233
N	3.6314	3.5785	4.2179	4.4697
H_2O	0.0759	0.1277	0.0948	0.1140
CO_2	0.4498	0.3787	0.4081	0.3654
CO	1.8825	1.6603	1.5924	1.5940
OH	1.1400	1.2911	1.1963	1.3256
O	4.0021	4.1635	4.3002	4.2356
H	6.5972	6.3873	6.4936	6.3556
C	1.5716	1.7377	1.8472	1.9458

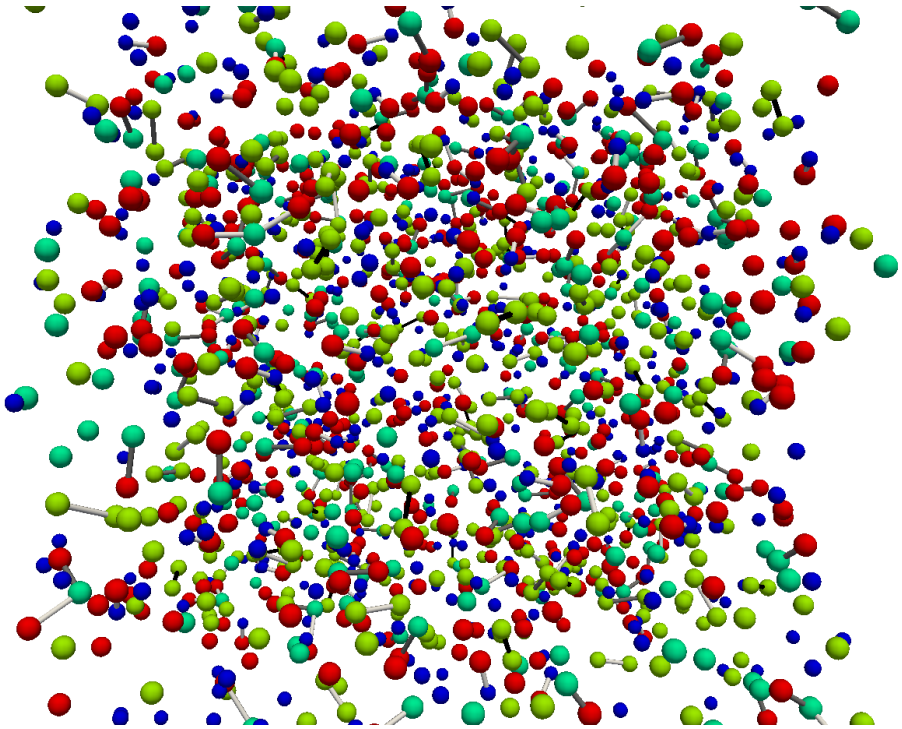

Figure 3.5: Snapshot of HMX detonation simulation at 18.2 ps (steady state in NVE)

Table 3.11: Experimental and simulated detonation products: HMX

Species	8 Molecules Simulation	16 Molecules Simulation	32 Molecules Simulation	64 Molecules Simulation	Exp. [83]
CO_2	2.000	2.375	2.313	1.906	1.92
CO	0.750	0.500	0.688	1.156	1.06
N_2	3.750	3.750	3.656	3.750	3.68
H_2O	2.500	2.750	2.688	2.969	3.18
C_2	0.375	0.500	0.500	0.406	0.485
H_2	0.375	0.250	0.188	0.188	0.30
NH_3	0.375	0.500	0.500	0.375	0.39

Table 3.12: Recovered material in experimental data: HMX

Atom Type	Ideal	Experimental
H	8	8.320
C	4	3.024
N	8	7.768
O	8	8.080

Table 3.13: Experimental and simulated energy release in eV per molecule: HMX

Exp. [83]	8 Molecules	16 Molecules	32 Molecules	64 Molecules
19.017	19.4923	19.5056	20.1161	20.2815

Table 3.14: Error in the simulated energy release: HMX

	8 Molecules	16 Molecules	32 Molecules	64 Molecules
error	0.0249	0.0257	0.0578	0.0665

Table 3.15: Error in the simulated detonation products: HMX

	8 Molecules	16 Molecules	32 Molecules	64 Molecules
error	0.1217	0.1562	0.1406	0.0542

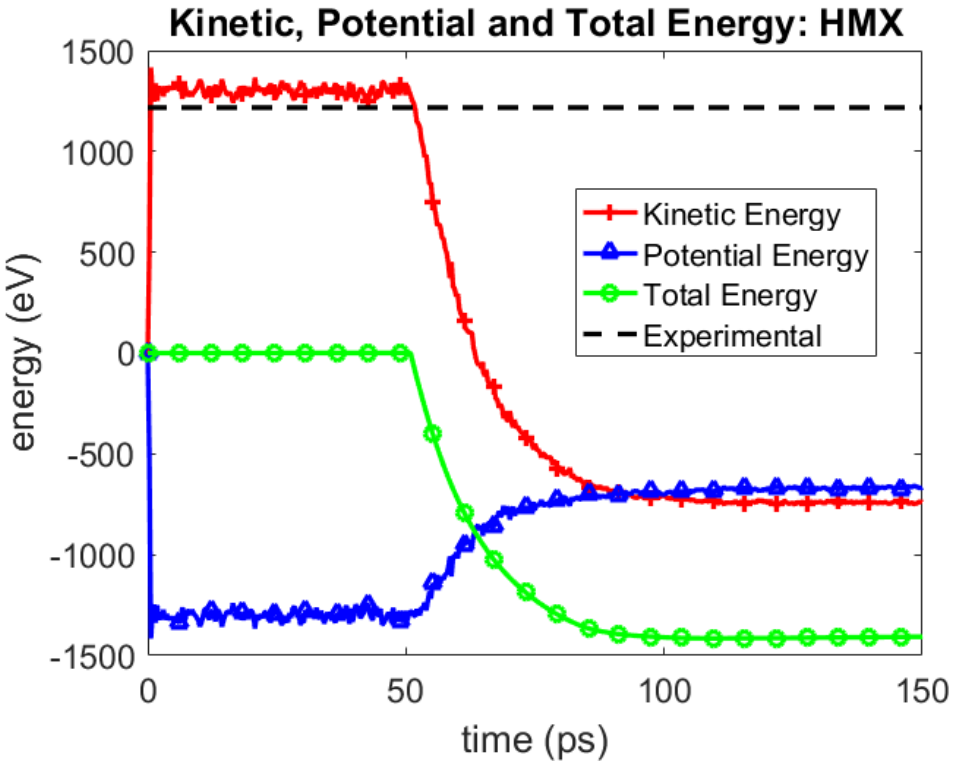

Figure 3.6: Variation in kinetic, potential, and total energy in the HMX simulation (dashed line is the experimental energy release [83])

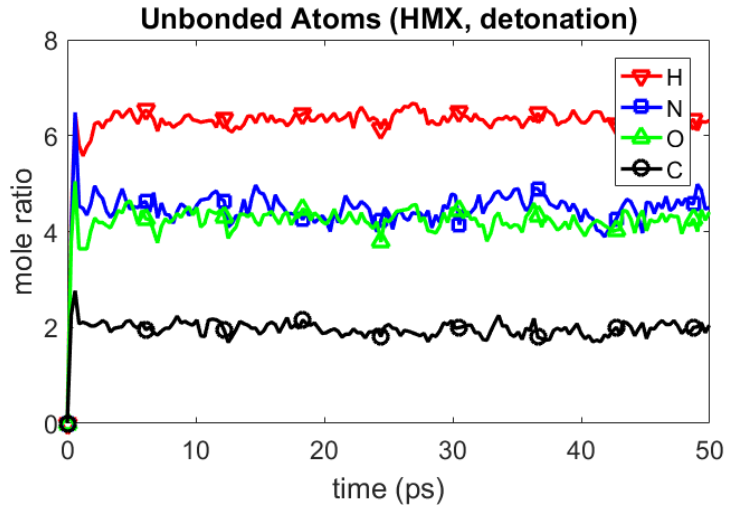

Figure 3.7: Concentration of unbonded atoms versus time (HMX, detonation)

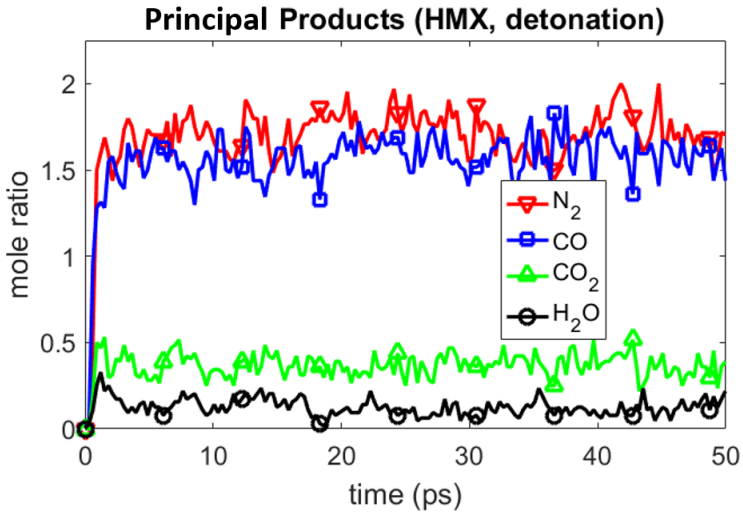

Figure 3.8: Concentration of principal end products versus time (HMX, detonation)

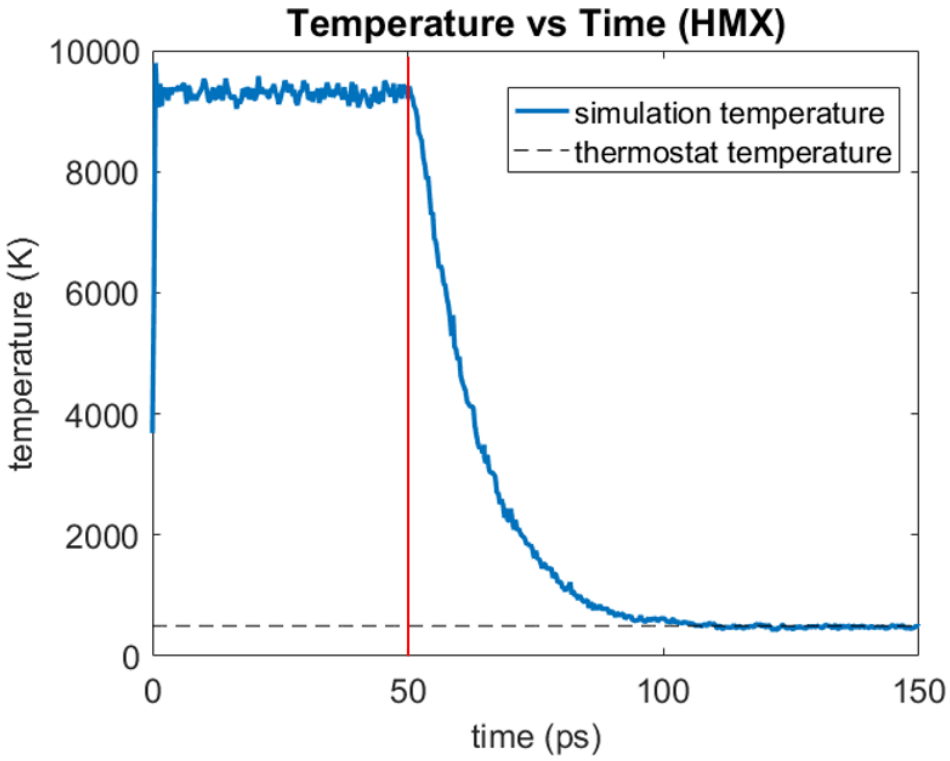

Figure 3.9: Temperature versus time (left of vertical line is NVE, right of vertical line is thermostatted): HMX

Table 3.16: Model reactions for the detonation chemistry: HMX

Reaction (j)	Chemical Reaction
1	$C_4H_8N_8O_8 \rightarrow 4\,NO_2 + 4\,CH_2 + 4\,N$
2	$NO_2 + CH_2 \rightarrow NOH + COH$
3	$4\,COH \rightarrow 0.35\,CO_2 + 1.65\,CO + 4\,H + 1.65\,O + 2\,C$
4	$4NOH \rightarrow 1.7\,N_2 + .6\,N + .15\,H_2\,O + 1.35\,OH + 2.5\,O + 2.35\,H$

Table 3.17: Species indices, initial mole ratios, and final mole ratios (detonation chemistry model): HMX

Species	Species Indices	Initial Mole Ratios	Final Mole Ratios
HMX	1	1.00	0.00
NO_2	2	0.00	0.00
CH_2	3	0.00	0.00
N_2	4	0.00	1.70
NOH	5	0.00	0.00
COH	6	0.00	0.00
CO_2	7	0.00	0.35
CO	8	0.00	1.65
C	9	0.00	2.00
H	10	0.00	6.35
O	11	0.00	4.15
N	12	0.00	4.60
H_2O	13	0.00	0.15
OH	14	0.00	1.35

Table 3.18: Stoichiometric matrix for the products in the detonation chemistry model ($\nu^{(i,j)}$): HMX

Species \ Reaction	1	2	3	4
HMX	0	0	0	0
NO_2	4	0	0	0
CH_2	4	0	0	0
N_2	0	0	0	1.70
NOH	0	1	0	0
COH	0	1	0	0
CO_2	0	0	0.35	0
CO	0	0	1.65	0
C	0	0	2.00	0
H	0	0	4.00	2.35
O	0	0	1.65	2.50
N	4	0	0	0.60
H_2O	0	0	0	0.15
OH	0	0	0	1.35

Table 3.19: Stoichiometric matrix for the reactants in the detonation chemistry model ($\hat{\nu}^{(i,j)}$): HMX

Species \ Reaction	1	2	3	4
HMX	1	0	0	0
NO_2	0	1	0	0
CH_2	0	1	0	0
N_2	0	0	0	0
NOH	0	0	0	4
COH	0	0	4	0
CO_2	0	0	0	0
CO	0	0	0	0
C	0	0	0	0
H	0	0	0	0
O	0	0	0	0
N	0	0	0	0
H_2O	0	0	0	0
OH	0	0	0	0

Table 3.20: Fit reaction rate coefficients and reaction orders (detonation chemistry model): HMX

Reaction (j)	$k^{(j)}$ $\left(\frac{1}{ps}\right)\left(\frac{moles}{cm^3}\right)^{1-m^{(j)}}$	$m^{(j)}$
1	48.68	1.27
2	148.82	2.00
3	23.26	1.41
4	25.15	1.23

Table 3.21: Concentration exponents (detonation chemistry model): HMX

Reaction (j)	Species (s)	$\alpha^{(s,j)}$
1	1	1.27
2	2	1.00
2	3	1.00
3	6	1.41
4	5	1.23

Note: all non-specified $\alpha^{(s,j)} = 0$

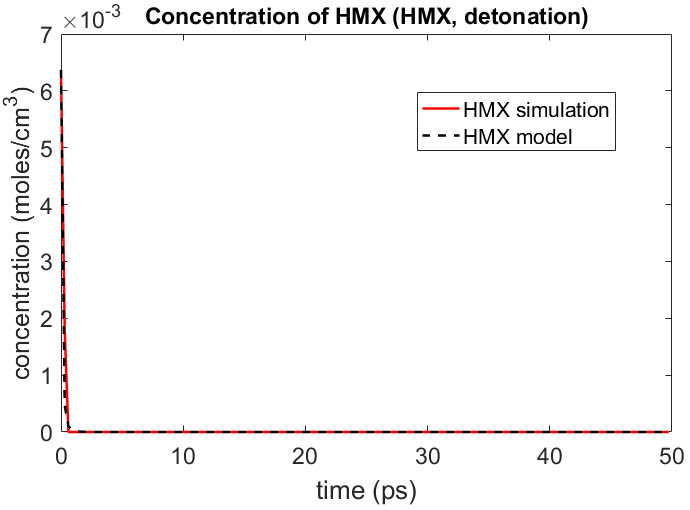

Figure 3.10: Concentration of HMX versus time (RMD simulation and detonation chemistry model): HMX

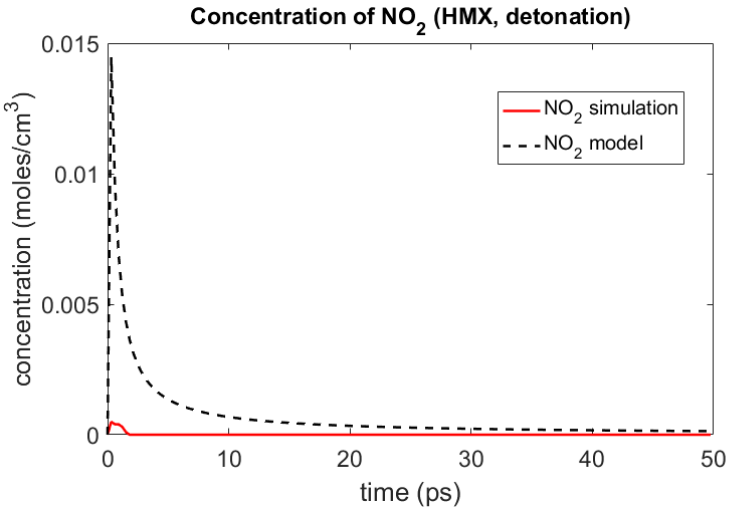

Figure 3.11: Concentration of NO_2 versus time (RMD simulation and detonation chemistry model): HMX)

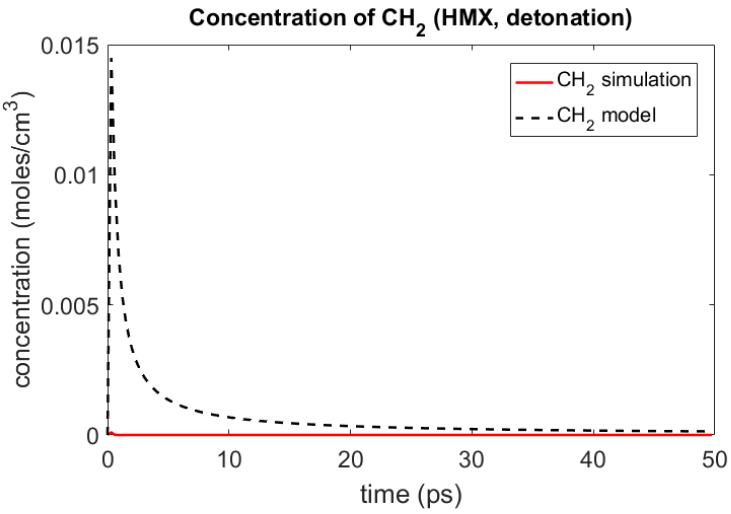

Figure 3.12: Concentration of CH_2 versus time (RMD simulation and detonation chemistry model): HMX

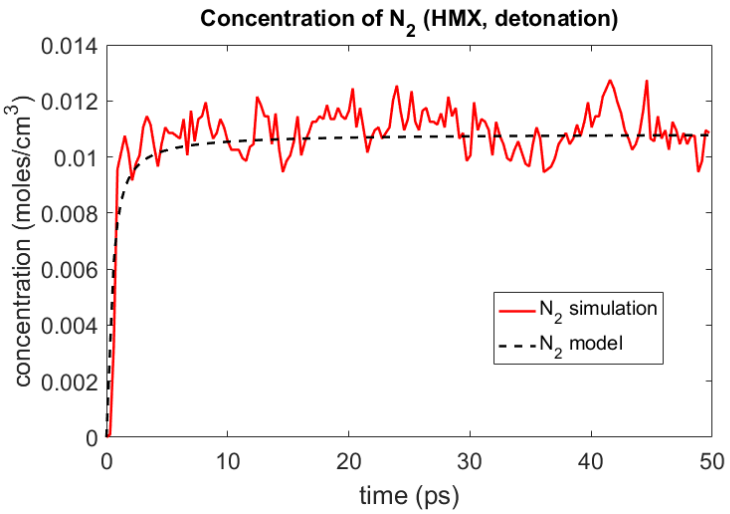

Figure 3.13: Concentration of $N2$ versus time (RMD simulation and detonation chemistry model): HMX

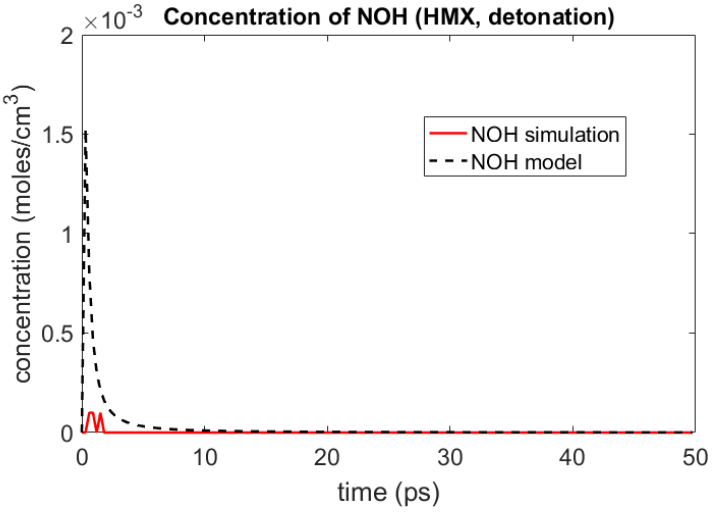

Figure 3.14: Concentration of NOH versus time (RMD simulation and detonation chemistry model): HMX

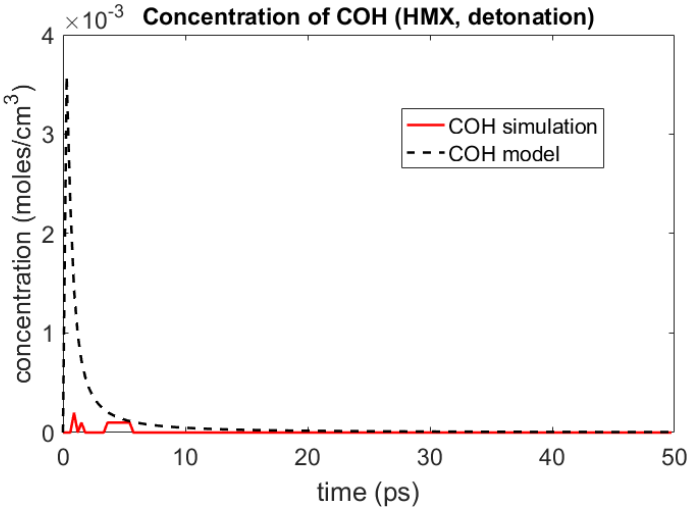

Figure 3.15: Concentration of COH versus time (RMD simulation and detonation chemistry model): HMX

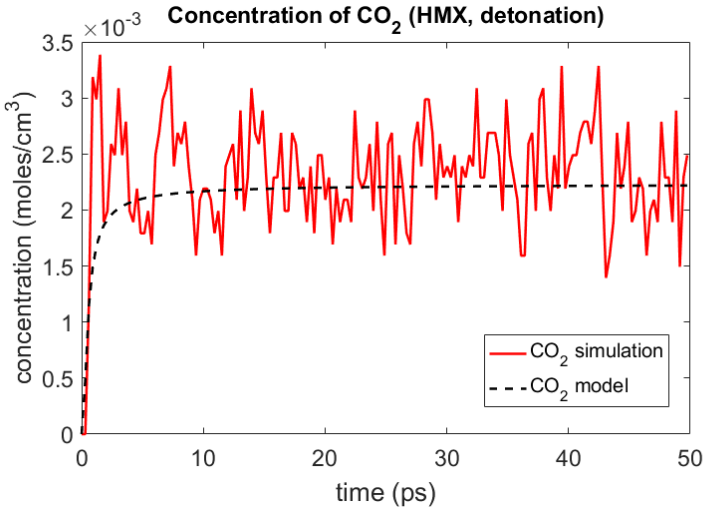

Figure 3.16: Concentration of CO_2 versus time (RMD simulation and detonation chemistry model): HMX

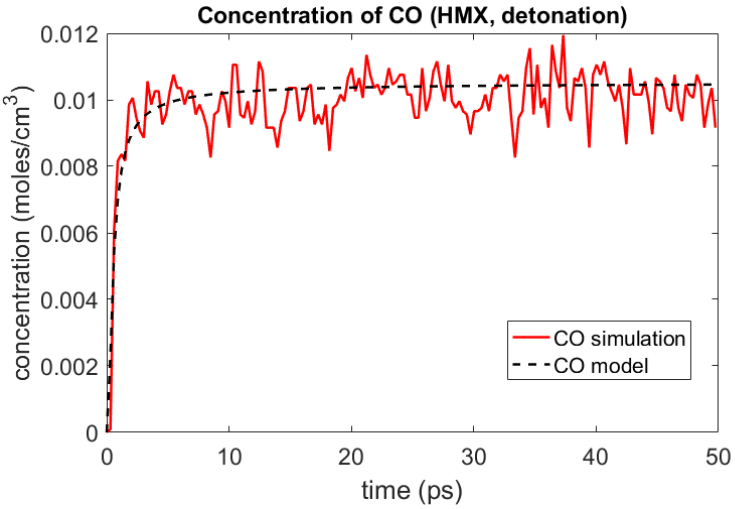

Figure 3.17: Concentration of CO versus time (RMD simulation and detonation chemistry model): HMX

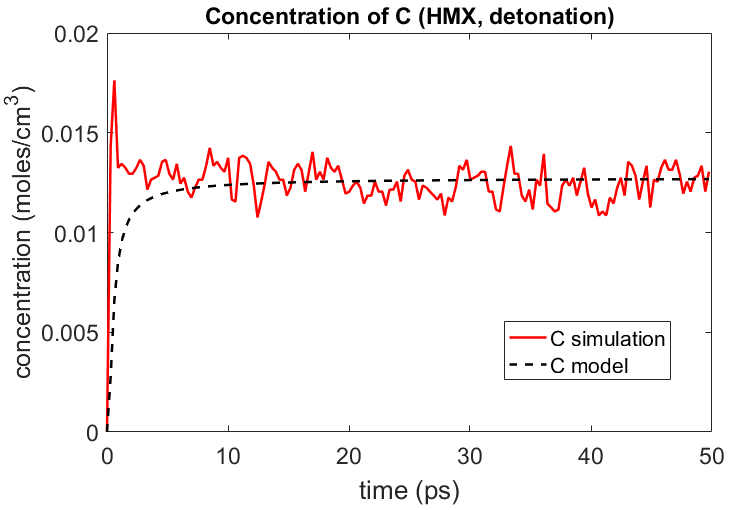

Figure 3.18: Concentration of C versus time (RMD simulation and detonation chemistry model): HMX

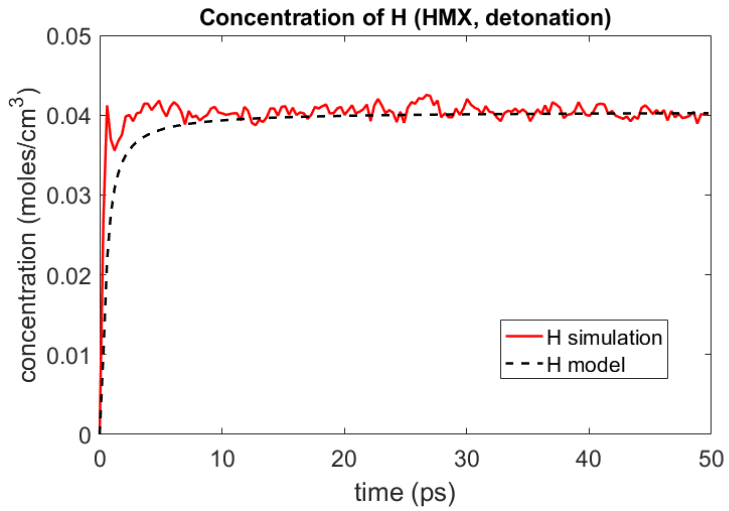

Figure 3.19: Concentration of H versus time (RMD simulation and detonation chemistry model): HMX

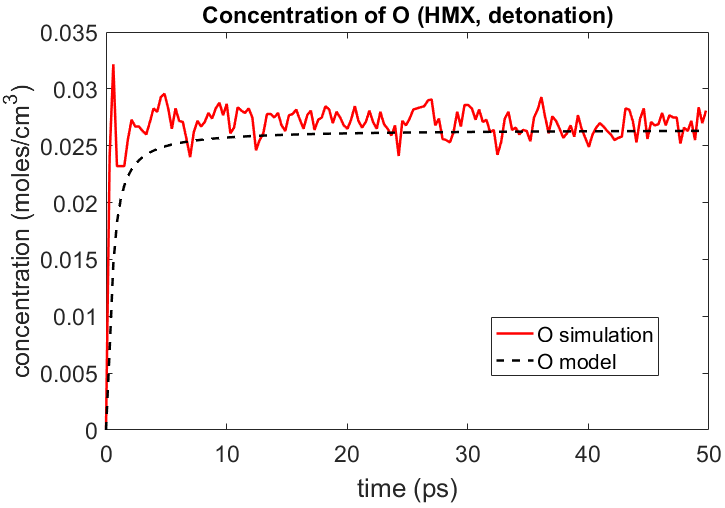

Figure 3.20: Concentration of O versus time (RMD simulation and detonation chemistry model): HMX

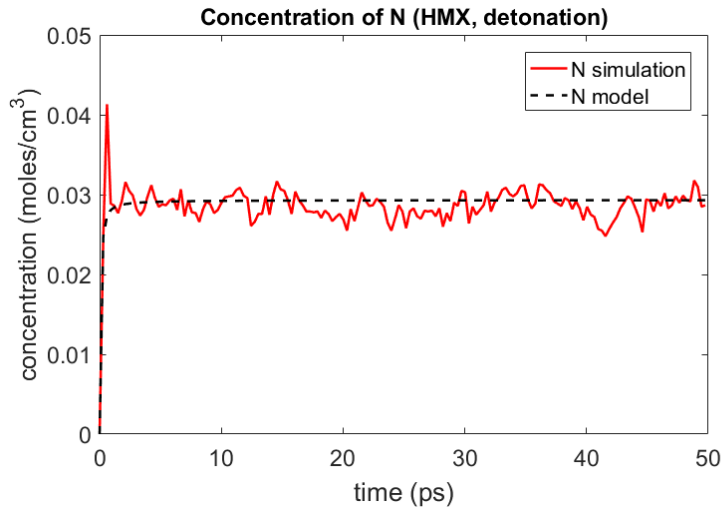

Figure 3.21: Concentration of N versus time (RMD simulation and detonation chemistry model): HMX

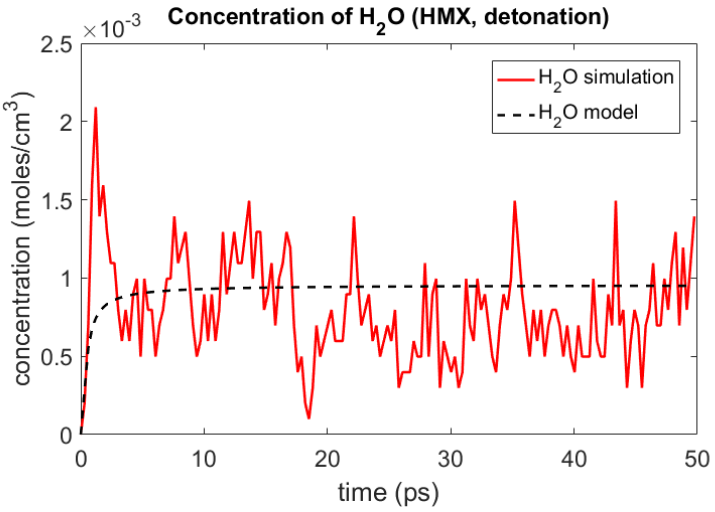

Figure 3.22: Concentration of H_2O versus time (RMD simulation and detonation chemistry model): HMX

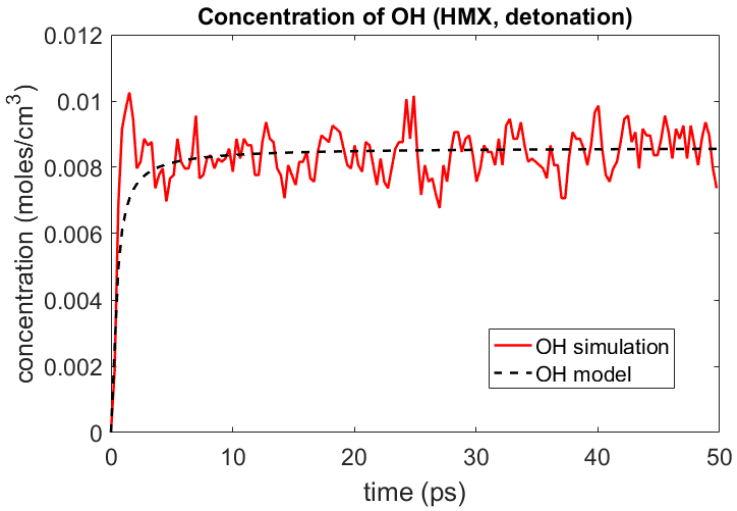

Figure 3.23: Concentration of OH versus time (RMD simulation and detonation chemistry model): HMX

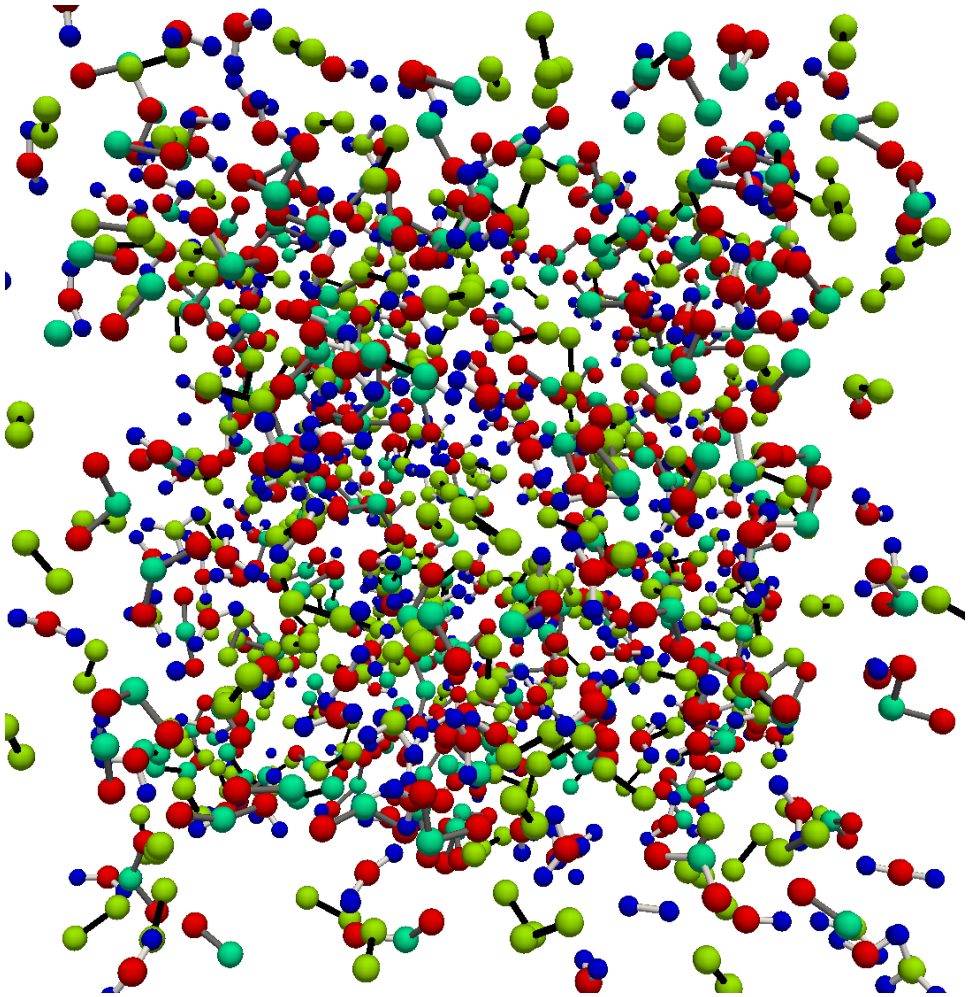

Figure 3.24: Snapshot of HMX detonation simulation at 129.1 ps (final detonation products)

Table 3.22: Model reactions for the recombination chemistry: HMX

Reaction (j)	Chemical Reaction
1	$C + O \rightarrow CO$
2	$CO + O \rightarrow CO_2$
3	$OH + H \rightarrow H_2O$
4	$2N \rightarrow N_2$
5	$O + H \rightarrow OH$
6	$N + 3H \rightarrow NH_3$
7	$2C \rightarrow C_2$
8	$2H \rightarrow H_2$
9	$H_2 + O \rightarrow H_2O$

Table 3.23: Species indices, initial mole ratios, and final mole ratios (recombination chemistry model): HMX

Species	Species Indices	Initial Mole Ratios	Final Mole Ratios
C	1	2.00	0.1899
O	2	4.15	0.0322
CO	3	1.65	1.1457
CO_2	4	0.35	1.8779
OH	5	1.35	0.1244
H	6	6.35	0.5546
H_2O	7	0.15	2.9419
N	8	4.60	0.1059
N_2	9	1.70	3.7709
NH_3	10	0.00	0.3522
C_2	11	0.00	0.3932
H_2	12	0.00	0.1903

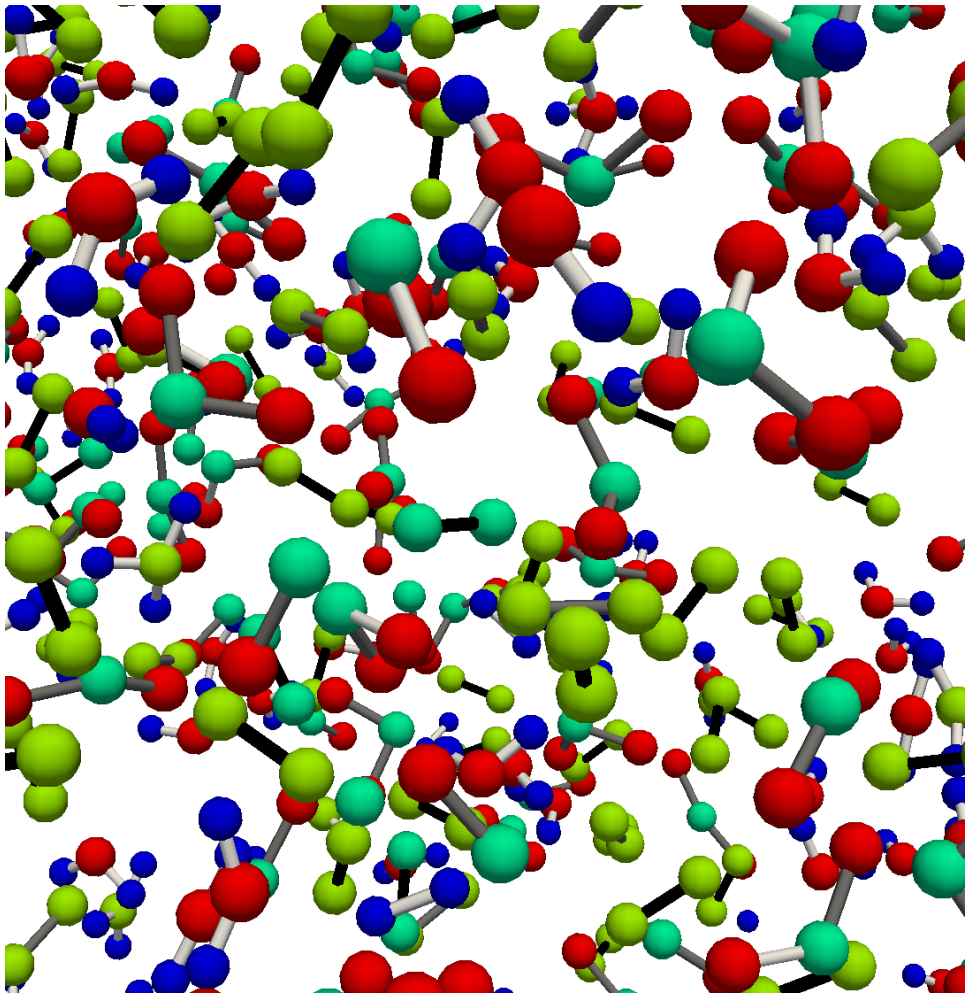

Figure 3.25: Zoomed in snapshot of HMX detonation simulation at 129.1 ps (final detonation products)

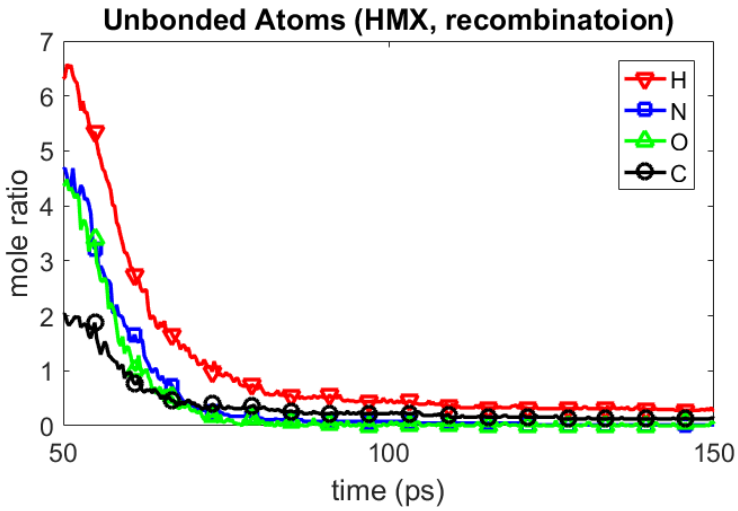

Figure 3.26: Concentration of unbonded atoms versus time (HMX, recombination)

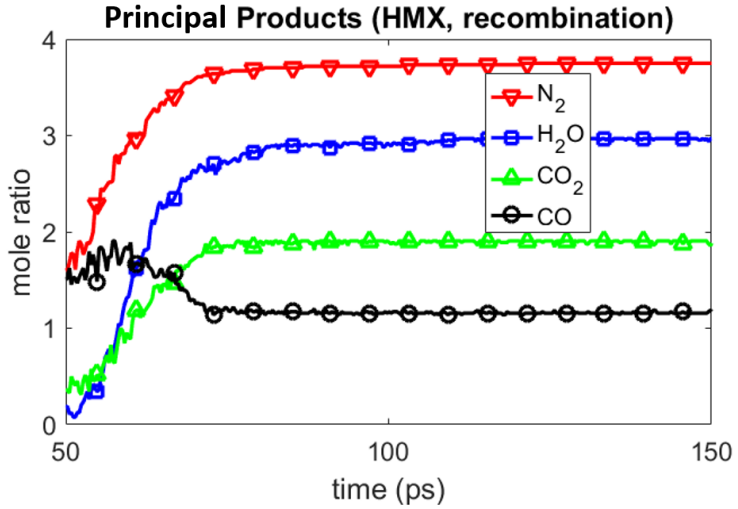

Figure 3.27: Concentration of principal end products versus time (HMX, recombination)

Table 3.24: Concentration exponents in the recombination chemistry model ($\alpha^{(s,j)}$): HMX

Species \ Reaction	1	2	3	4	5	6	7	8	9
C	1	0	0	0	0	0	1	0	0
O	1	1	0	0	1	0	0	0	1
CO	0	1	0	0	0	0	0	0	0
CO_2	0	0	0	0	0	0	0	0	0
OH	0	0	1	0	0	0	0	0	0
H	0	0	1	0	1	1	0	1	0
H_2O	0	0	0	0	0	0	0	0	0
N	0	0	0	1	0	1	0	0	0
N_2	0	0	0	0	0	0	0	0	0
NH_3	0	0	0	0	0	0	0	0	0
C_2	0	0	0	0	0	0	0	0	0
H_2	0	0	0	0	0	0	0	0	1

Table 3.25: Stoichiometric matrix for the products in the recombination chemistry model ($\nu^{(i,j)}$): HMX

Species \ Reaction	1	2	3	4	5	6	7	8	9
C	0	0	0	0	0	0	0	0	0
O	0	0	0	0	0	0	0	0	0
CO	1	0	0	0	0	0	0	0	0
CO_2	0	1	0	0	0	0	0	0	0
OH	0	0	0	0	1	0	0	0	0
H	0	0	0	0	0	0	0	0	0
H_2O	0	0	1	0	0	0	0	0	1
N	0	0	0	0	0	0	0	0	0
N_2	0	0	0	1	0	0	0	0	0
NH_3	0	0	0	0	0	1	0	0	0
C_2	0	0	0	0	0	0	1	0	0
H_2	0	0	0	0	0	0	0	1	0

Table 3.26: Stoichiometric matrix for the reactants in the recombination chemistry model ($\hat{\nu}^{(i,j)}$): HMX

Species \ Reaction	1	2	3	4	5	6	7	8	9
C	1	0	0	0	0	0	2	0	0
O	1	1	0	0	1	0	0	0	1
CO	0	1	0	0	0	0	0	0	0
CO_2	0	0	0	0	0	0	0	0	0
OH	0	0	1	0	0	0	0	0	0
H	0	0	1	0	1	3	0	2	0
H_2O	0	0	0	0	0	0	0	0	0
N	0	0	0	2	0	1	0	0	0
N_2	0	0	0	0	0	0	0	0	0
NH_3	0	0	0	0	0	0	0	0	0
C_2	0	0	0	0	0	0	0	0	0
H_2	0	0	0	0	0	0	0	0	1

Table 3.27: Fit reaction rate coefficients, temperature exponents, and reaction orders (recombination chemistry model): HMX

Reaction (j)	$k^{(j)}$ $\left(\frac{moles}{cm^3}\right)^{1-m^{(j)}}$	$\gamma^{(j)}$	$m^{(j)}$
1	622.10	1.6519	2
2	1454.4	2.9375	2
3	1064.5	2.5222	2
4	2.3172	0.6958	1
5	82.640	0.6583	2
6	2366.6	11.999	2
7	2.3864	2.6451	1
8	0.3390	2.3435	1
9	0.0212	2.5449	2

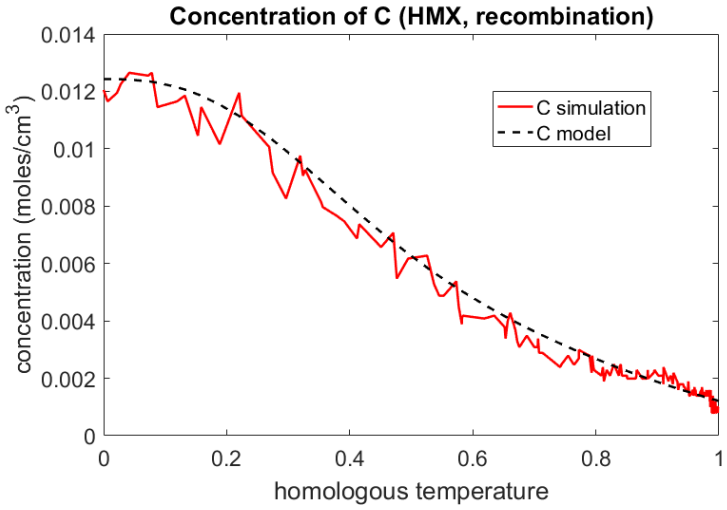

Figure 3.28: Concentration of C versus homologous temperature (RMD simulation and recombination chemistry model): HMX

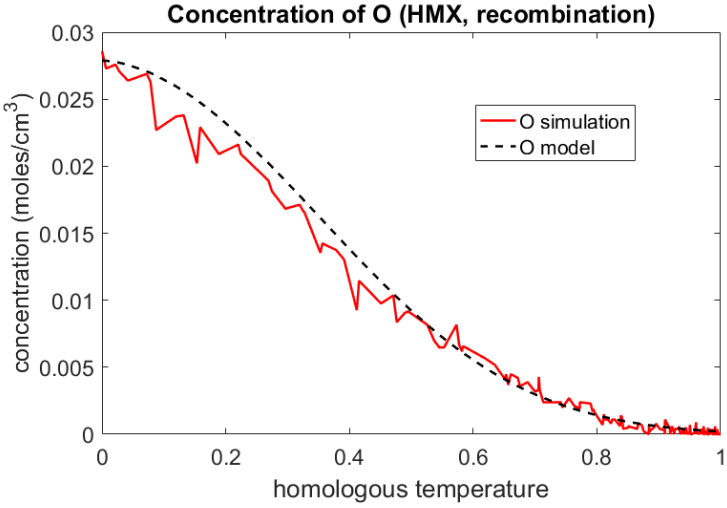

Figure 3.29: Concentration of O versus homologous temperature (RMD simulation and recombination chemistry model): HMX

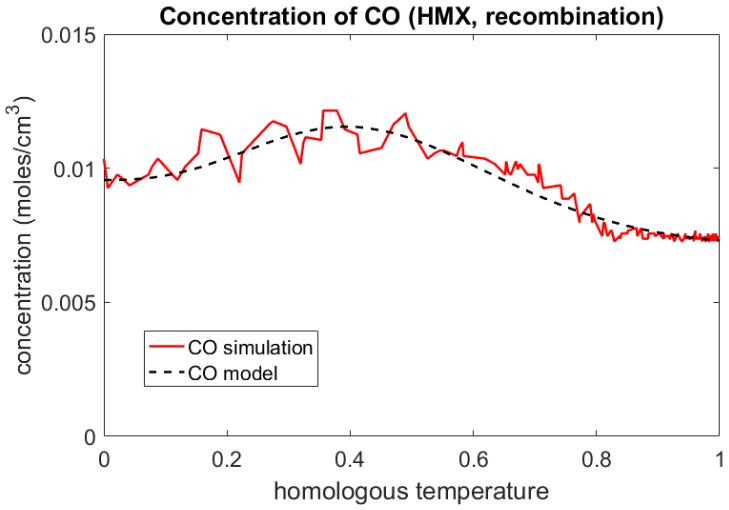

Figure 3.30: Concentration of CO versus homologous temperature (RMD simulation and recombination chemistry model): HMX

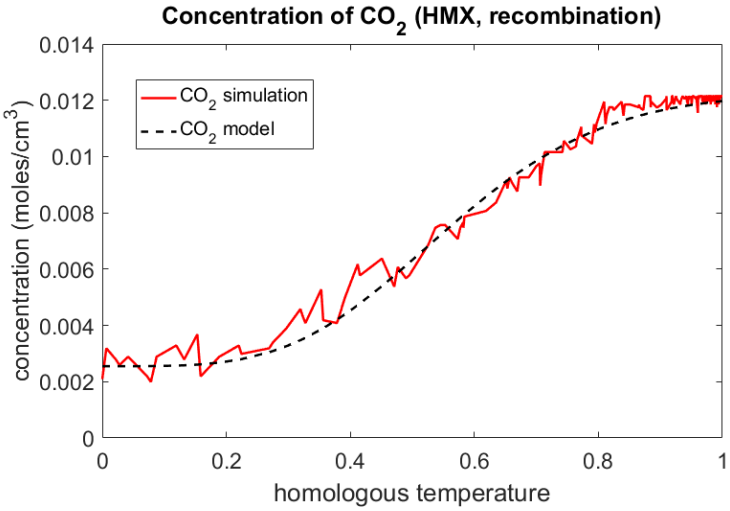

Figure 3.31: Concentration of CO_2 versus homologous temperature (RMD simulation and recombination chemistry model): HMX

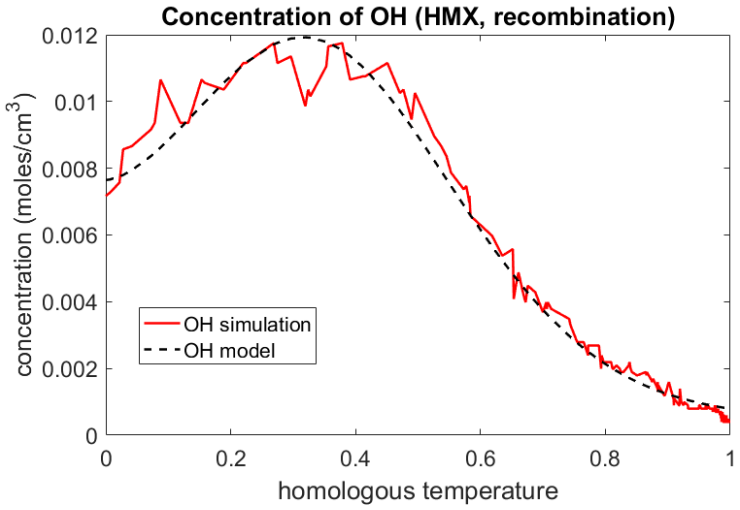

Figure 3.32: Concentration of OH versus homologous temperature (RMD simulation and recombination chemistry model): HMX

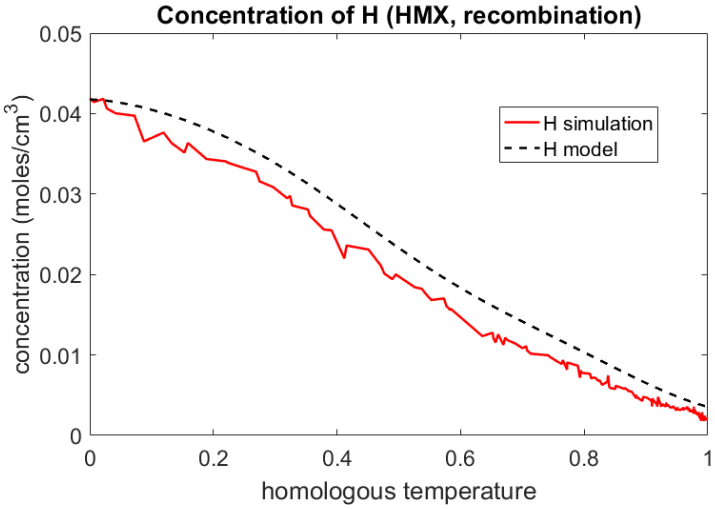

Figure 3.33: Concentration of H versus homologous temperature (RMD simulation and recombination chemistry model): HMX

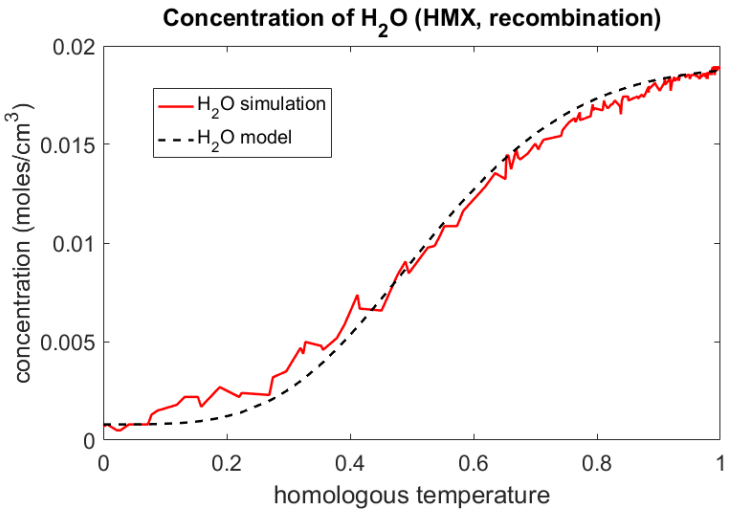

Figure 3.34: Concentration of H_2O versus homologous temperature (RMD simulation and recombination chemistry model): HMX

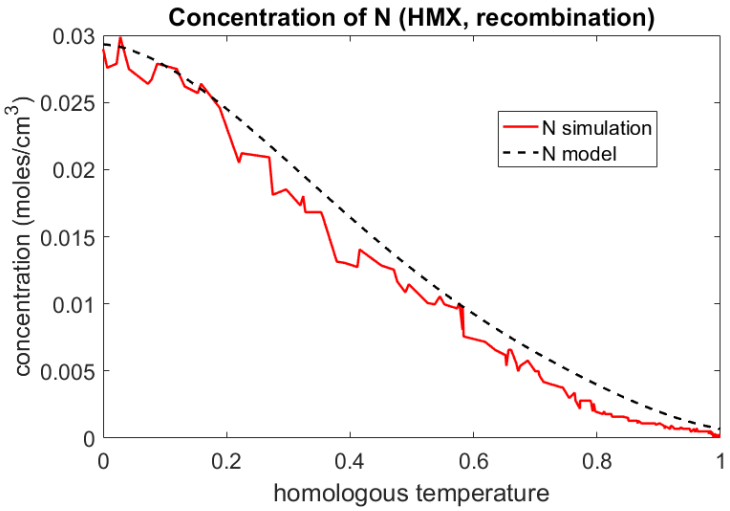

Figure 3.35: Concentration of N versus homologous temperature (RMD simulation and recombination chemistry model): HMX

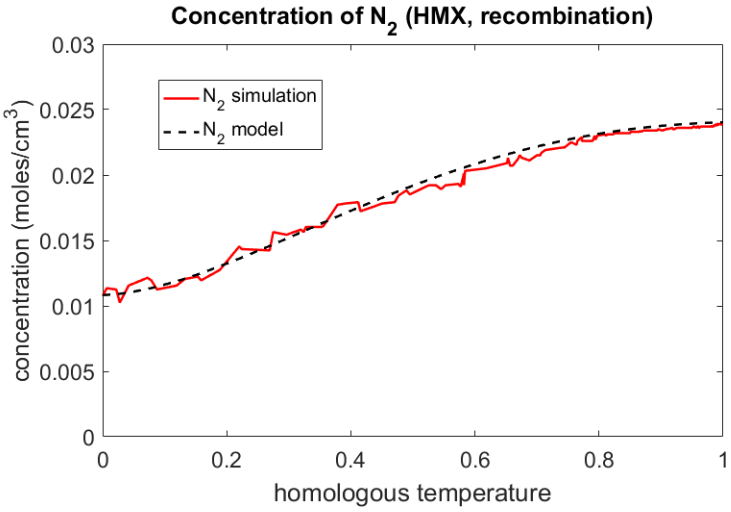

Figure 3.36: Concentration of N_2 versus homologous temperature (RMD simulation and recombination chemistry model): HMX

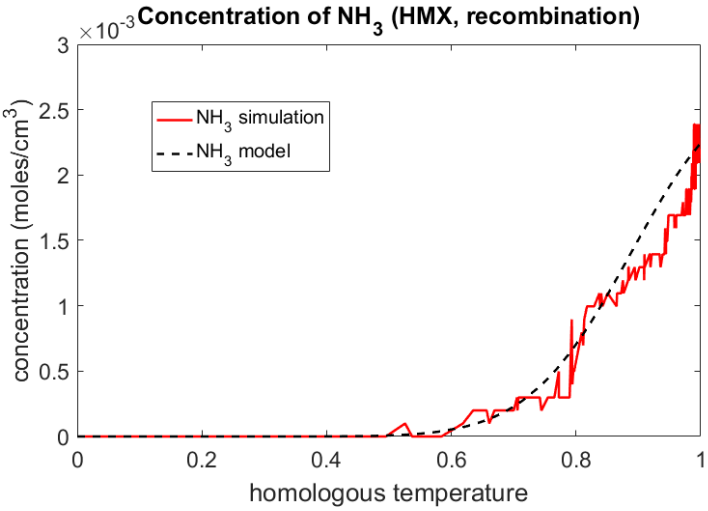

Figure 3.37: Concentration of NH_3 versus homologous temperature (RMD simulation and recombination chemistry model): HMX

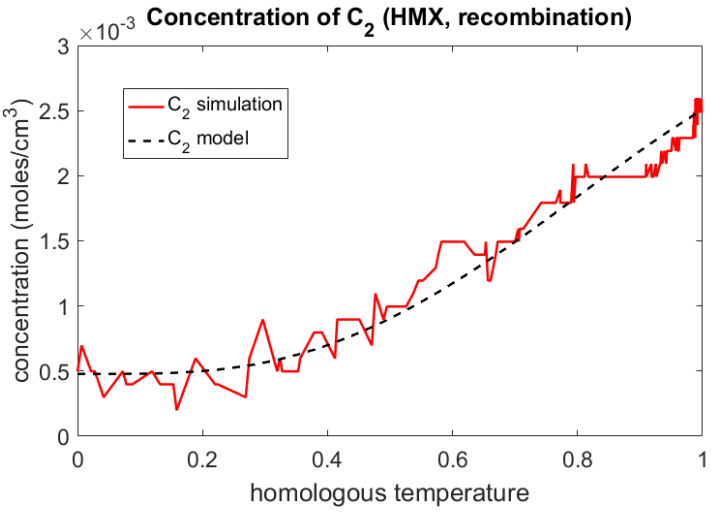

Figure 3.38: Concentration of C_2 versus homologous temperature (RMD simulation and recombination chemistry model): HMX

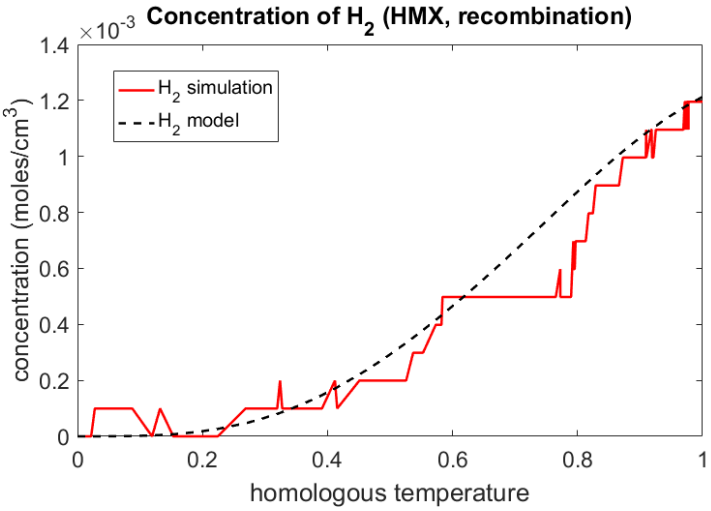

Figure 3.39: Concentration of H_2 versus homologous temperature (RMD simulation and recombination chemistry model): HMX

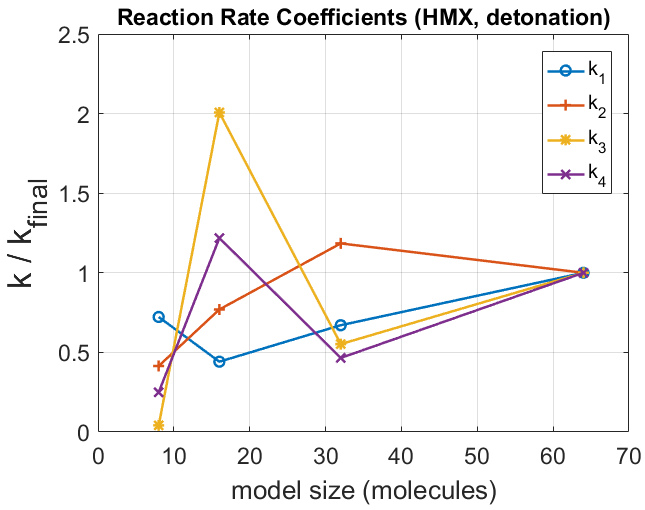

Figure 3.40: Reaction rate coefficients versus model size (detonation chemistry model): HMX

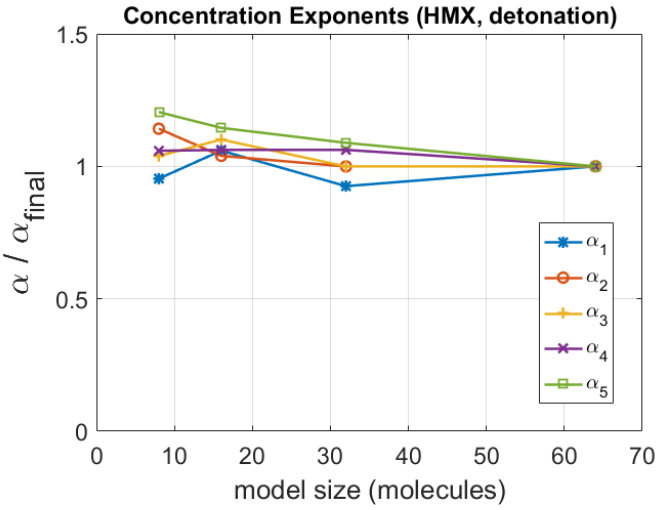

Figure 3.41: Concentration exponents versus model size (detonation chemistry model): HMX

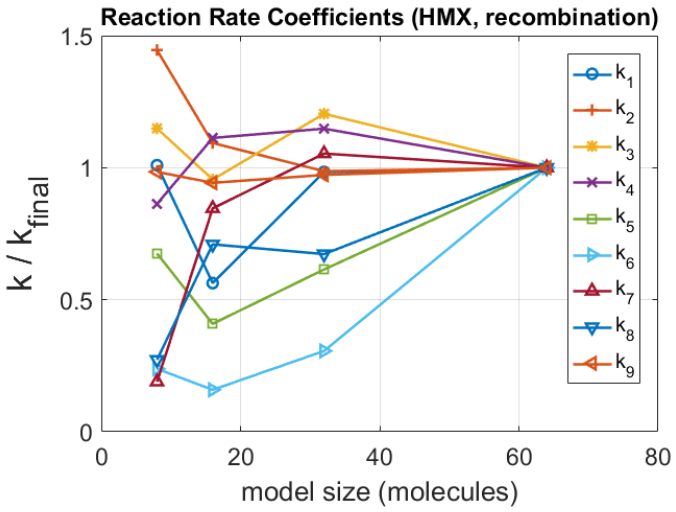

Figure 3.42: Reaction rate coefficients versus model size (recombination chemistry model): HMX

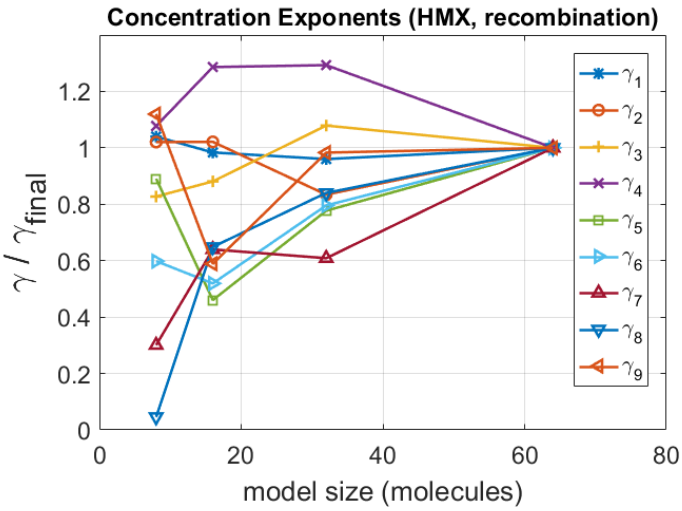

Figure 3.43: Homologous temperature exponents versus model size (recombination chemistry model): HMX

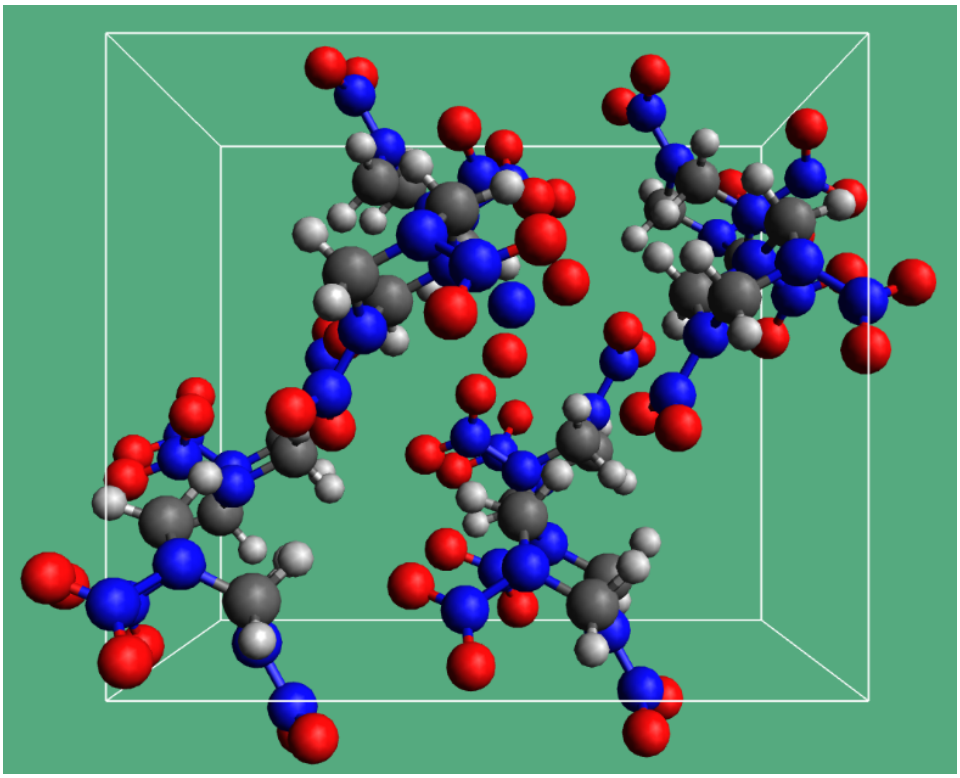

Figure 3.44: Unit cell for α-RDX (light gray is hydrogen, gray is carbon, blue is nitrogen, red is oxygen)

Table 3.28: Effective valence for unbonded atoms ($\nu_{\alpha,\beta}^{unb}$): RDX

	H	**C**	**N**	**O**
H	1	0	2	2
C	0	1	0	4
N	6	0	1	0
O	4	2	0	0

Table 3.29: Bond type probability matrix ($P_{\alpha,\beta}^{bnd}$): RDX

	H	**C**	**N**	**O**
H	0.1667	0.0000	0.0000	0.8333
C	0.0000	0.2333	0.0000	0.7667
N	0.0000	0.0000	1.0000	0.0000
O	0.4167	0.5833	0.0000	0.0000

Table 3.30: Random number minimum matrix ($\omega_{\alpha,\beta}^{min}$): RDX

	H	**C**	**N**	**O**
H	0.0000	0.1667	0.1667	0.1667
C	0.0000	0.0000	0.2333	0.2333
N	0.0000	0.0000	0.0000	1.0000
O	0.0000	0.4167	1.0000	1.0000

Table 3.31: Random number maximum matrix ($\omega_{\alpha,\beta}^{max}$): RDX

	H	**C**	**N**	**O**
H	0.1667	0.1667	0.1667	1.0000
C	0.0000	0.2333	0.2333	1.0000
N	0.0000	0.0000	1.0000	1.0000
O	0.4167	1.0000	1.0000	1.0000

Table 3.32: Experimental and approximated (atom conservative) detonation products: RDX

Species	N_2	H_2O	CO_2	CO	$C(s)$	H_2	NH_3	CH_4	HCN
Exp. [83]	2.80	2.34	1.39	1.1	0.44	.34	.028	.041	.029
Emp.	3.00	2.50	1.20	1.10	0.70	.50	0.00	0.00	0.00

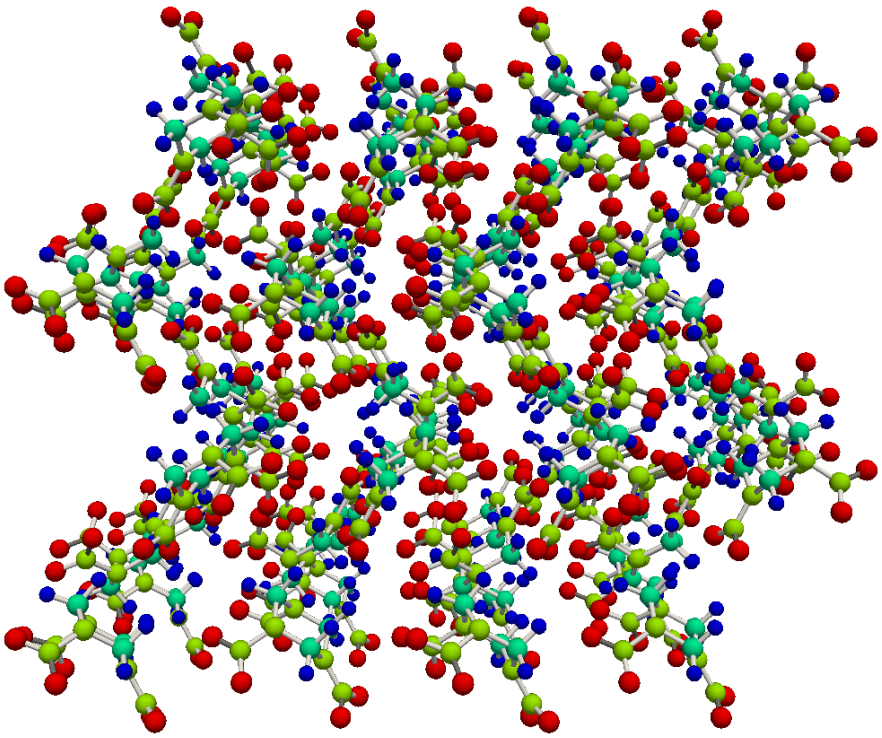

Figure 3.45: Sixty-four molecule crystal of α-RDX

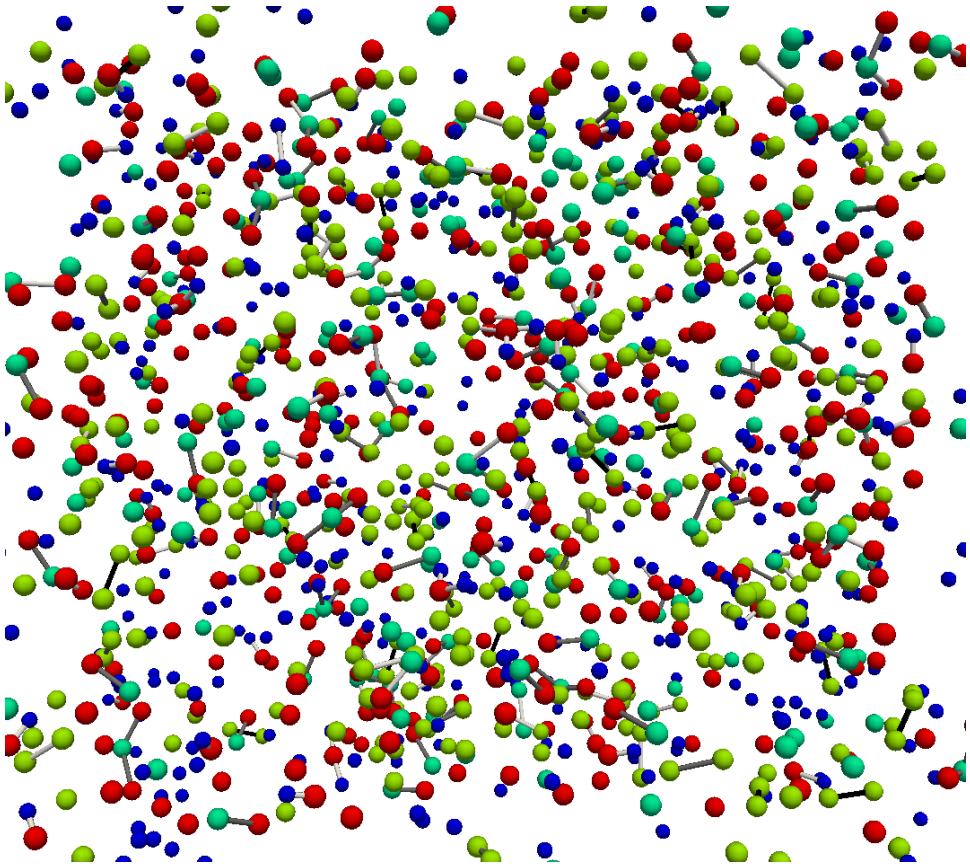

Figure 3.46: Snapshot of RDX detonation simulation at 18.3 ps (steady state in NVE)

Table 3.33: Steady state species concentrations (NVE): RDX

Species	8 Molecules Simulation	16 Molecules Simulation	32 Molecules Simulation	64 Molecules Simulation
N_2	1.7361	1.5561	1.5118	1.3073
N	2.5278	2.8878	2.9765	3.3854
H_2O	0.0534	0.1079	0.1167	0.0887
CO_2	0.2767	0.2431	0.2423	0.2314
CO	1.2639	1.2505	1.1477	1.1235
OH	0.8376	1.0337	1.2118	1.0873
O	3.2917	3.1218	3.0393	3.2376
H	4.8483	4.6864	4.5067	4.6918
C	1.3248	1.4829	1.5614	1.5905

Table 3.34: Experimental and simulated detonation products: RDX

Species	8 Molecules Simulation	16 Molecules Simulation	32 Molecules Simulation	64 Molecules Simulation	Exp. [83]
CO_2	1.875	1.188	1.094	1.234	1.39
CO	0.375	1.188	1.188	1.016	1.10
N_2	3.000	3.000	3.000	3.000	2.80
H_2O	1.875	2.438	2.563	2.500	2.34
H_2	0.750	0.500	0.406	0.438	0.34
C_2	0.375	0.250	0.281	0.297	0.22

Table 3.35: Recovered material in experimental data: RDX

Atom Type	Ideal	Experimental
H	6	5.640
C	3	2.565
N	6	5.544
O	6	6.240

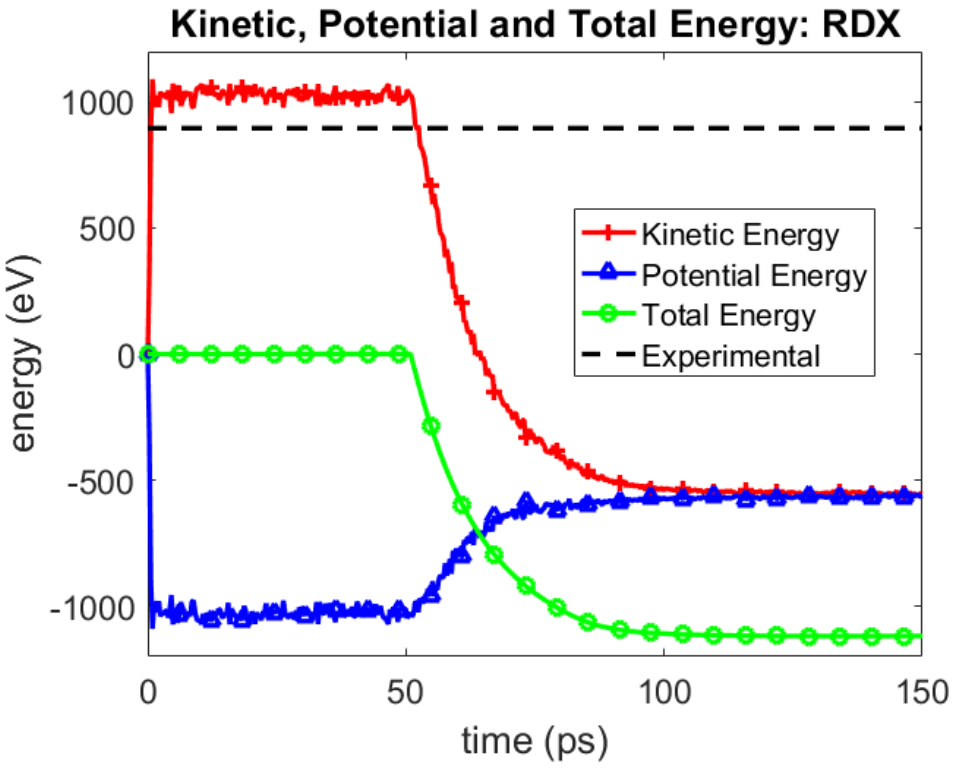

Figure 3.47: Variation in kinetic, potential, and total energy in the RDX simulation (dashed line is the experimental energy release [83])

Table 3.36: Experimental and simulated energy release in eV per molecule: RDX

Exp. [83]	8 Molecules	16 Molecules	32 Molecules	64 Molecules
14.0060	15.3198	15.7371	15.6965	15.8058

Table 3.37: Error in the simulated energy release: RDX

	8 Molecules	16 Molecules	32 Molecules	64 Molecules
error	0.0938	0.1236	0.1207	0.1285

Table 3.38: Error in the simulated detonation products: RDX

	8 Molecules	16 Molecules	32 Molecules	64 Molecules
error	0.2979	0.0949	0.1140	0.0946

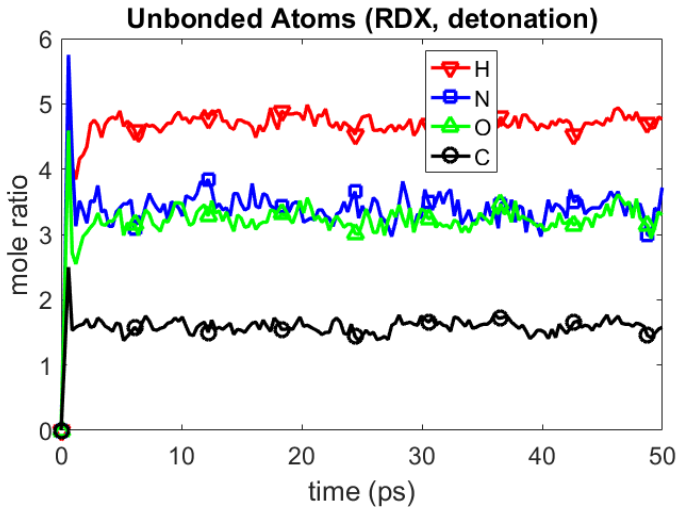

Figure 3.48: Concentration of unbonded atoms versus time (RDX, detonation)

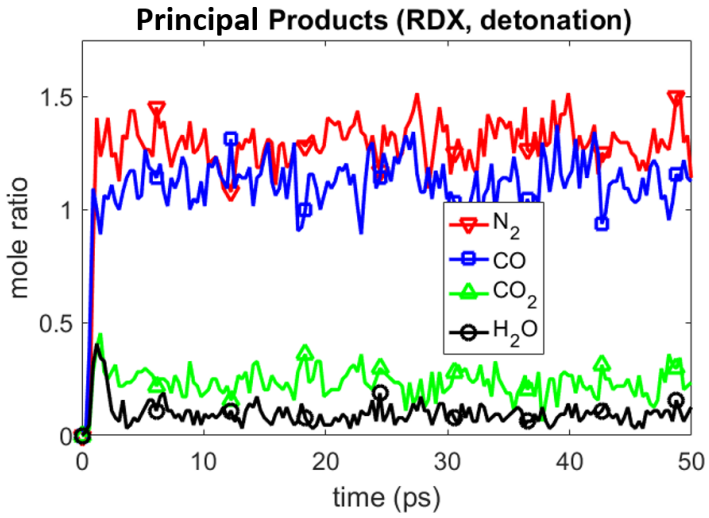

Figure 3.49: Concentration of principal end products versus time (RDX, detonation)

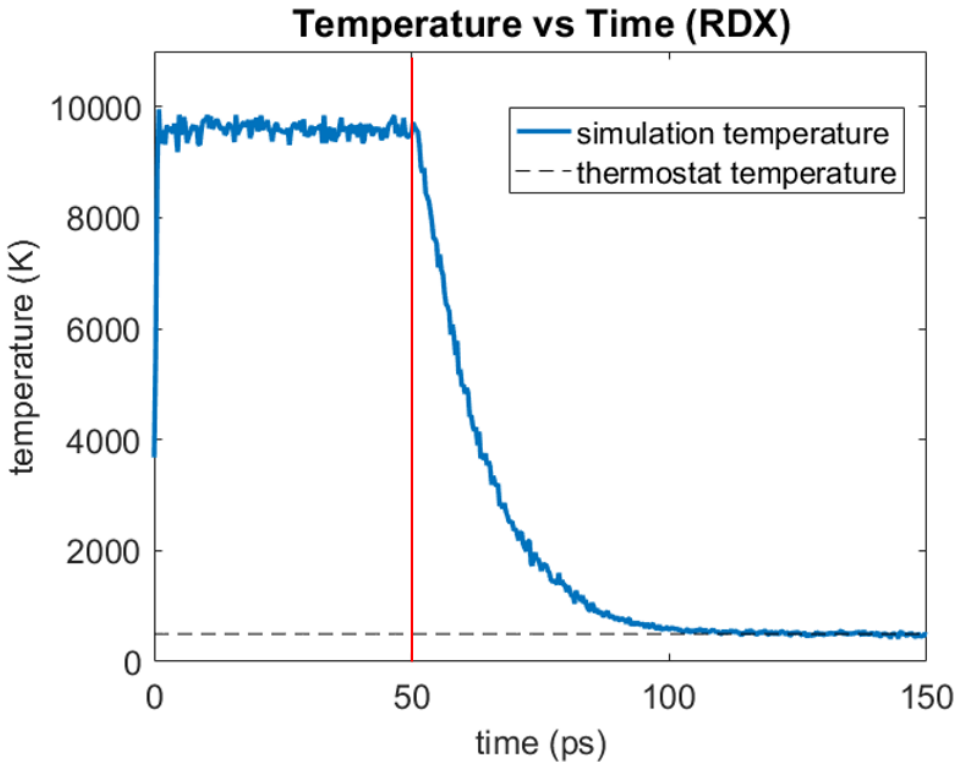

Figure 3.50: Temperature versus time (left of vertical line is NVE, right of vertical line is thermostatted): RDX

Table 3.39: Model reactions for the detonation chemistry: RDX

Reaction (j)	Chemical Reaction
1	$C_3H_6N_6O_6 \rightarrow 3\,NO_2 + 3\,CH_2 + 3\,N$
2	$NO_2 + CH_2 \rightarrow NOH + COH$
3	$3\,COH \rightarrow 0.25\,CO_2 + 1.15\,CO + 3\,H + 1.35\,O + 1.6\,C$
4	$3\,NOH \rightarrow 1.3\,N_2 + 0.4\,N + 0.1\,H_2O + 1.1\,OH + 1.8\,O + 1.7\,H$

Table 3.40: Species indices, initial mole ratios, and final mole ratios (detonation chemistry model): RDX

Species	Species Indices	Initial Mole Ratio	Final Mole Ratio
RDX	1	1.00	0.00
NO_2	2	0.00	0.00
CH_2	3	0.00	0.00
N_2	4	0.00	1.30
NOH	5	0.00	0.00
COH	6	0.00	0.00
CO_2	7	0.00	0.25
CO	8	0.00	1.15
C	9	0.00	1.60
H	10	0.00	4.70
O	11	0.00	3.15
N	12	0.00	3.40
H_2O	13	0.00	0.10
OH	14	0.00	1.10

Table 3.41: Stoichiometric matrix for the products in the detonation chemistry model ($\nu^{(i,j)}$): RDX

Species \ Reaction	1	2	3	4
RDX	0	0	0	0
NO_2	3	0	0	0
CH_2	3	0	0	0
N_2	0	0	0	1.30
NOH	0	1	0	0
COH	0	1	0	0
CO_2	0	0	0.25	0
CO	0	0	1.15	0
C	0	0	1.60	0
H	0	0	3.00	1.70
O	0	0	1.35	1.80
N	3	0	0	0.40
H_2O	0	0	0	0.10
OH	0	0	0	1.10

Table 3.42: Stoichiometric matrix for the reactants in the detonation chemistry model ($\hat{\nu}^{(i,j)}$): RDX

Species \ Reaction	1	2	3	4
RDX	1	0	0	0
NO_2	0	1	0	0
CH_2	0	1	0	0
N_2	0	0	0	0
NOH	0	0	0	3
COH	0	0	3	0
CO_2	0	0	0	0
CO	0	0	0	0
C	0	0	0	0
H	0	0	0	0
O	0	0	0	0
N	0	0	0	0
H_2O	0	0	0	0
OH	0	0	0	0

Table 3.43: Fit reaction rate coefficients and reaction orders (detonation chemistry model): RDX

Reaction (j)	$k^{(j)}$ $\left(\frac{1}{ps}\right)\left(\frac{moles}{cm^3}\right)^{1-m^{(j)}}$	$m^{(j)}$
1	6.02	1.04
2	499.32	2.00
3	9.91	1.40
4	1.45	1.00

Table 3.44: Concentration exponents (detonation chemistry model): RDX

Reaction (j)	Species (s)	$\alpha^{(s,j)}$
1	1	1.04
2	2	1.00
2	3	1.00
3	6	1.40
4	5	1.00

Note: all non-specified $\alpha^{(s,j)} = 0$

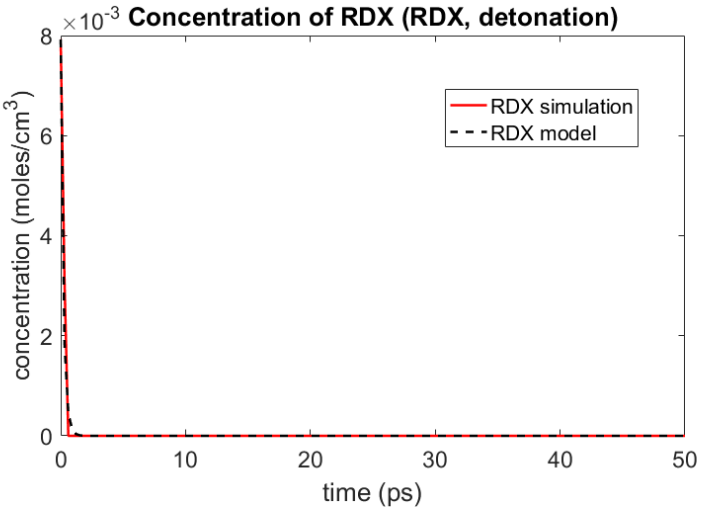

Figure 3.51: Concentration of RDX versus time (RMD simulation and detonation chemistry model): RDX

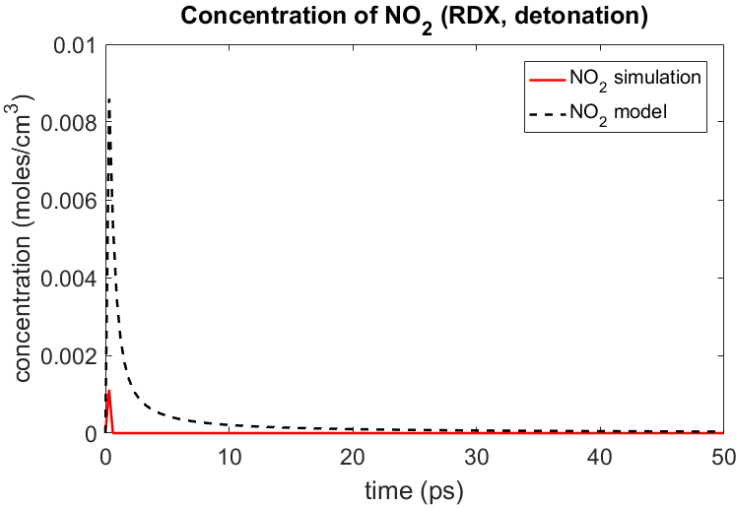

Figure 3.52: Concentration of NO_2 versus time (RMD simulation and detonation chemistry model): RDX

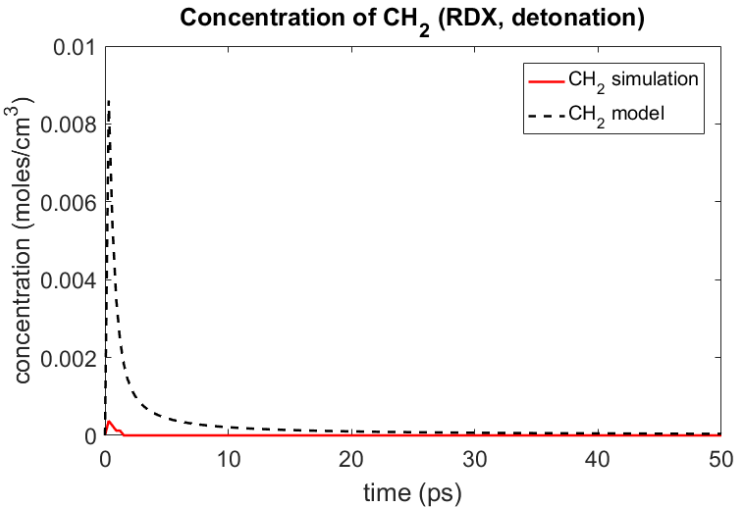

Figure 3.53: Concentration of CH_2 versus time (RMD simulation and detonation chemistry model): RDX

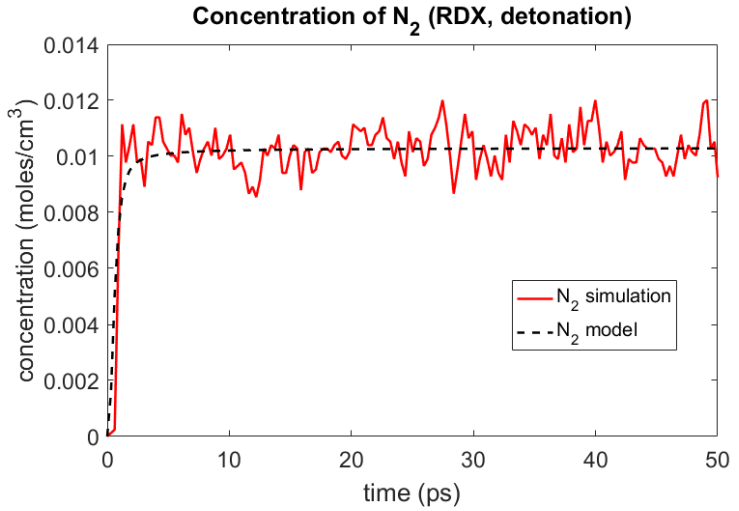

Figure 3.54: Concentration of N_2 versus time (RMD simulation and detonation chemistry model): RDX

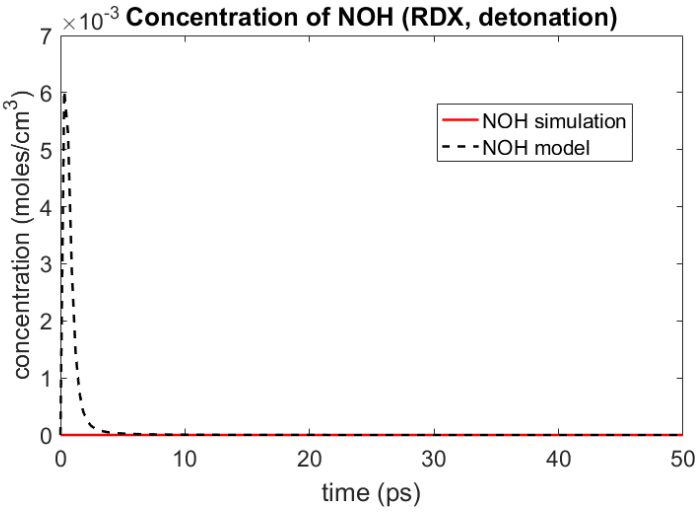

Figure 3.55: Concentration of NOH versus time (RMD simulation and detonation chemistry model): RDX

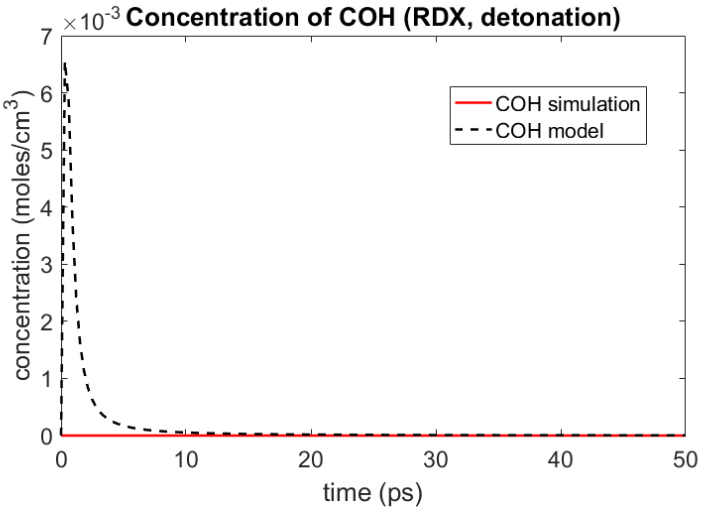

Figure 3.56: Concentration of COH versus time (RMD simulation and detonation chemistry model): RDX

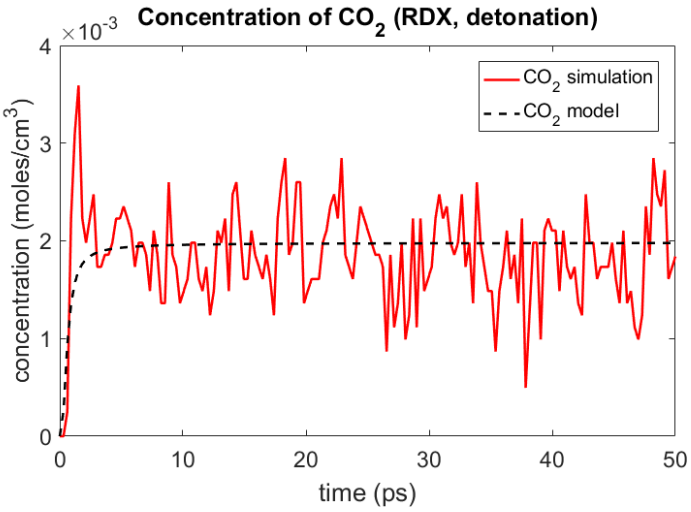

Figure 3.57: Concentration of CO_2 versus time (RMD simulation and detonation chemistry model): RDX

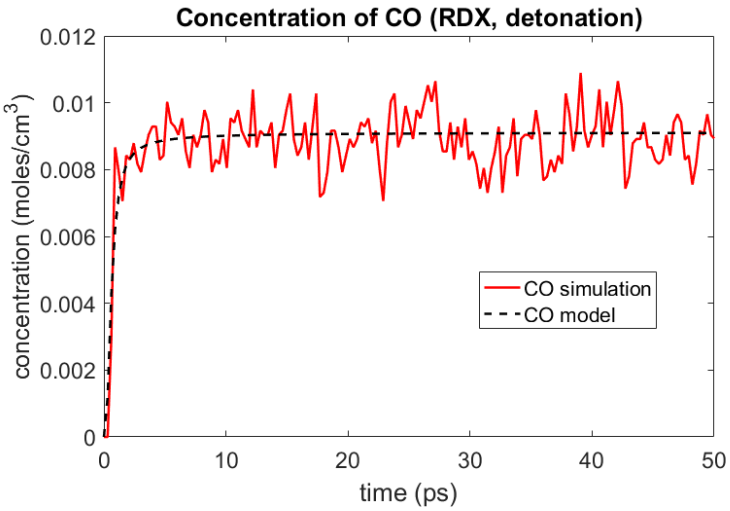

Figure 3.58: Concentration of CO versus time (RMD simulation and detonation chemistry model): RDX

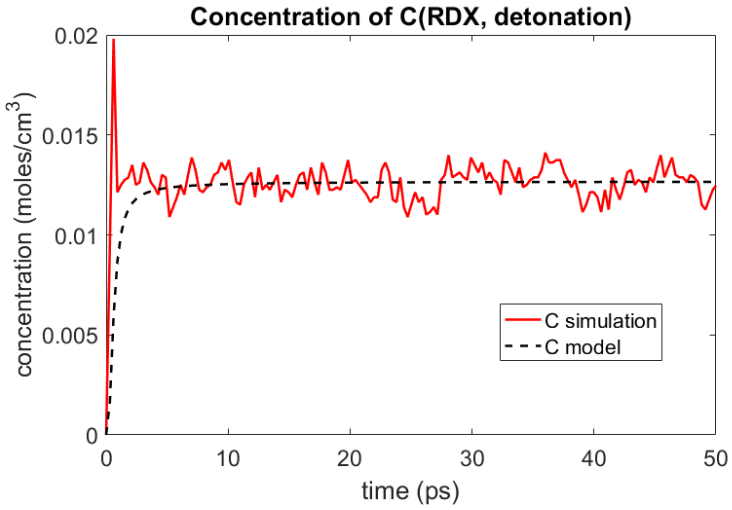

Figure 3.59: Concentration of C versus time (RMD simulation and detonation chemistry model): RDX

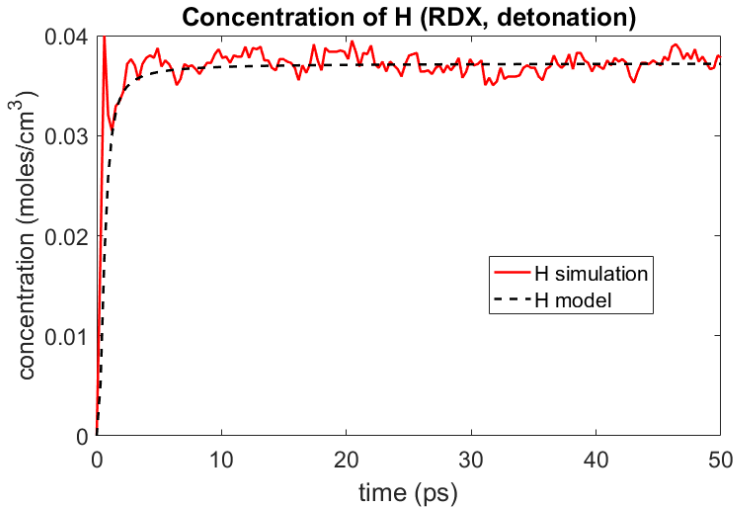

Figure 3.60: Concentration of H versus time (RMD simulation and detonation chemistry model): RDX

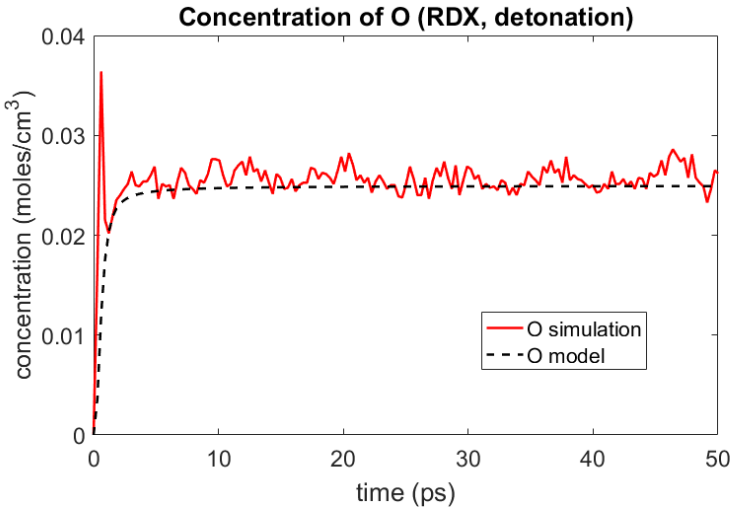

Figure 3.61: Concentration of O versus time (RMD simulation and detonation chemistry model): RDX

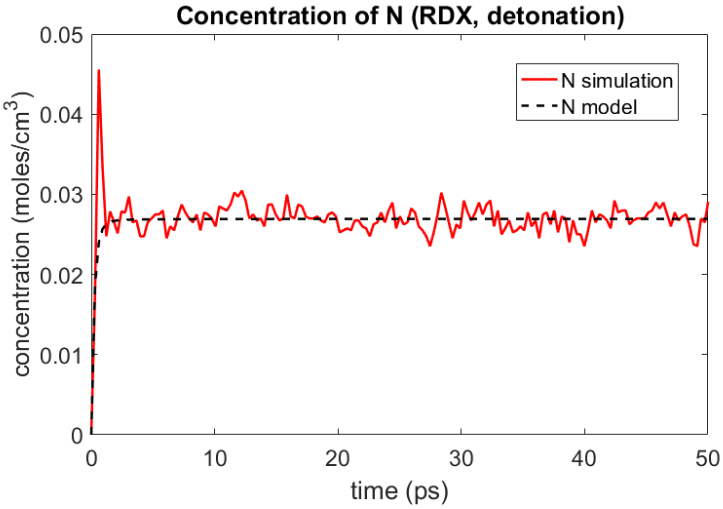

Figure 3.62: Concentration of N versus time (RMD simulation and detonation chemistry model): RDX

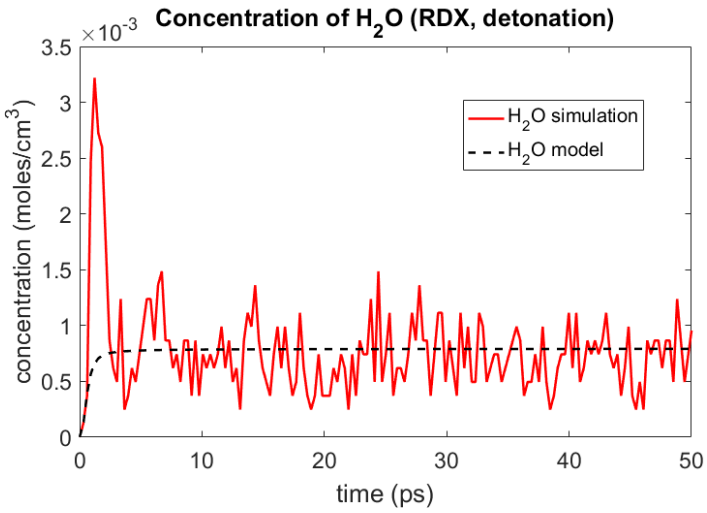

Figure 3.63: Concentration of H_2O versus time (RMD simulation and detonation chemistry model): RDX

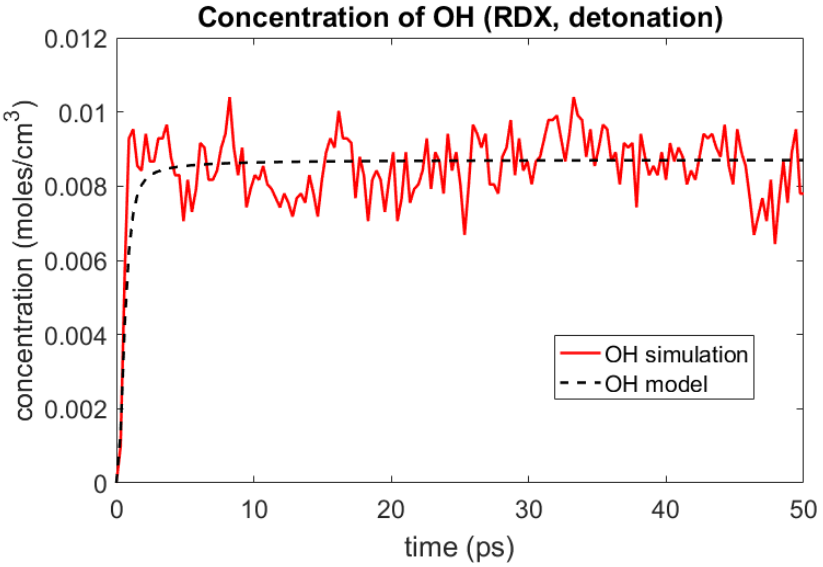

Figure 3.64: Concentration of OH versus time (RMD simulation and detonation chemistry model): RDX

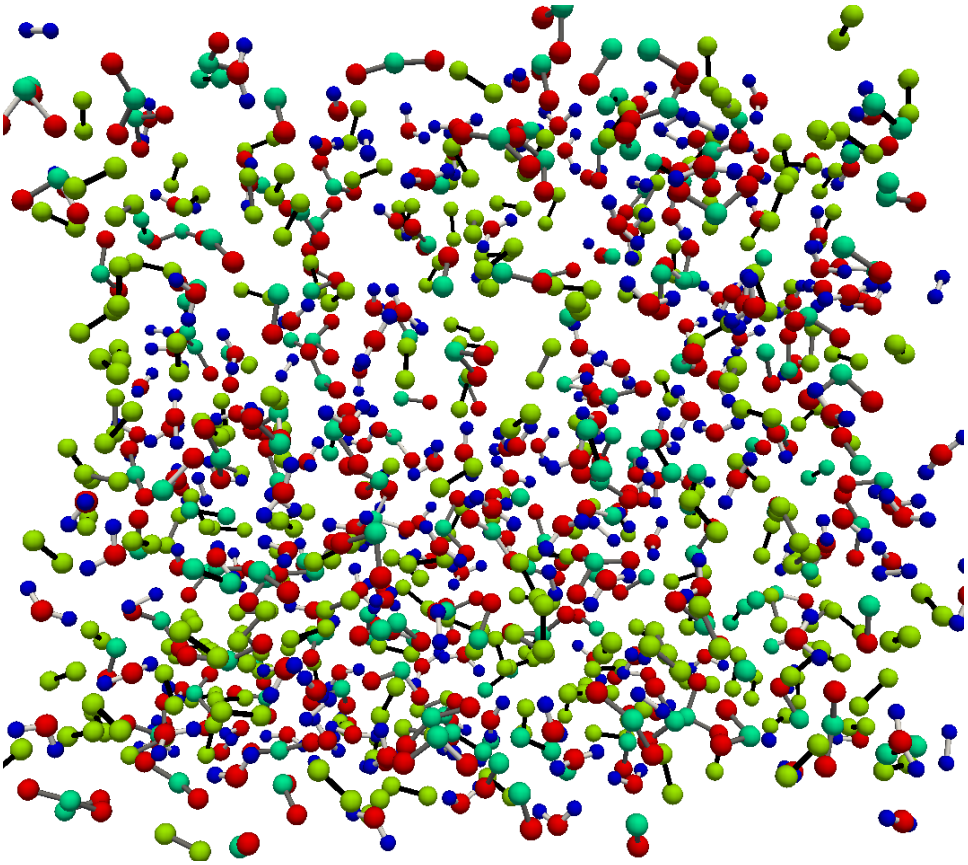

Figure 3.65: Snapshot of RDX detonation simulation at 148.9 ps (final detonation products)

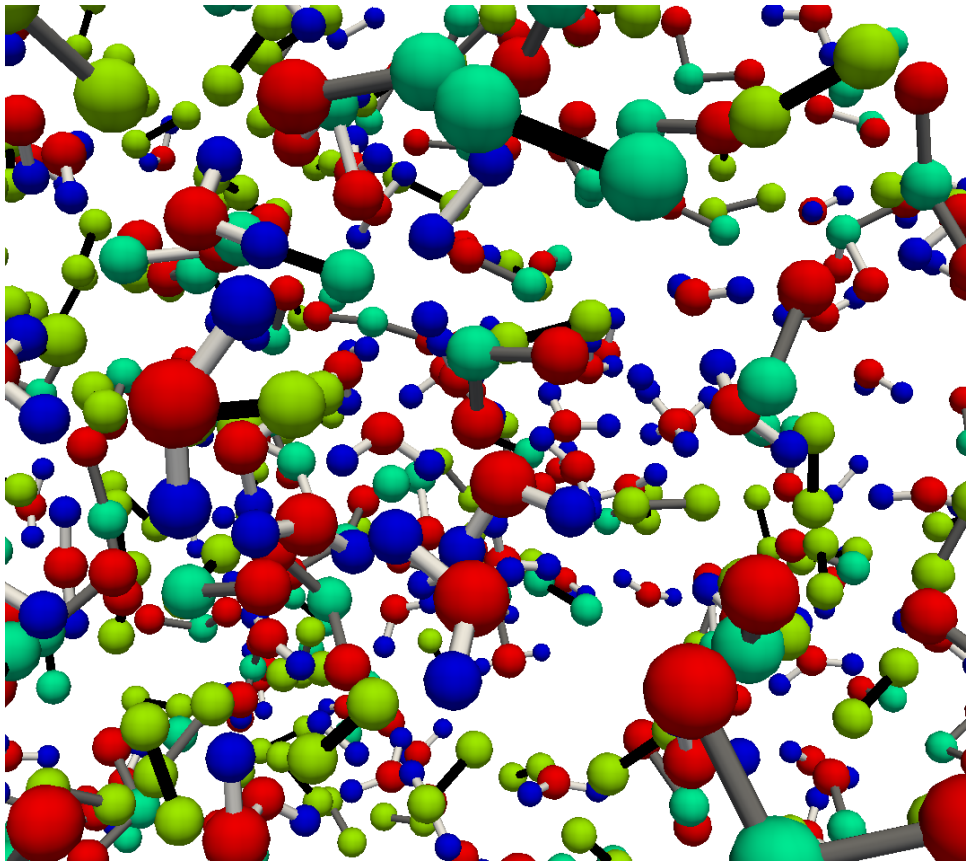

Figure 3.66: Zoomed in snapshot of RDX detonation simulation at 148.9 ps (final detonation products)

Table 3.45: Model reactions for the recombination chemistry: RDX

Reaction (j)	Chemical Reaction
1	$C + O \rightarrow CO$
2	$CO + O \rightarrow CO_2$
3	$OH + H \rightarrow H_2O$
4	$2N \rightarrow N_2$
5	$O + H \rightarrow OH$
6	$2C \rightarrow C_2$
7	$2H \rightarrow H_2$
8	$H_2 + O \rightarrow H_2O$

Table 3.46: Species indices, initial mole ratios, and final mole ratios (recombination chemistry model): RDX

Species	Species Indices	Initial Mole Ratio	Final Mole Ratio
C	1	1.60	0.1523
O	2	3.15	0.0261
CO	3	1.15	1.0103
CO_2	4	0.25	1.2197
OH	5	1.10	0.0957
H	6	4.70	0.2030
H_2O	7	0.10	2.4287
N	8	3.40	0.0707
N_2	9	1.30	2.9646
C_2	10	0.00	0.3089
H_2	11	0.00	0.4220

Table 3.47: Concentration exponents in the recombination chemistry model ($\alpha^{(s,j)}$): RDX

Species \ Reaction	1	2	3	4	5	6	7	8
C	1	0	0	0	0	1	0	0
O	1	1	0	0	1	0	0	1
CO	0	1	0	0	0	0	0	0
CO_2	0	0	0	0	0	0	0	0
OH	0	0	1	0	0	0	0	0
H	0	0	1	0	1	0	1	0
H_2O	0	0	0	0	0	0	0	0
N	0	0	0	1	0	0	0	0
N_2	0	0	0	0	0	0	0	0
C_2	0	0	0	0	0	0	0	0
H_2	0	0	0	0	0	0	0	1

Table 3.48: Stoichiometric matrix for the products in the recombination chemistry model ($\nu^{(i,j)}$): RDX

Species \ Reaction	1	2	3	4	5	6	7	8
C	0	0	0	0	0	0	0	0
O	0	0	0	0	0	0	0	0
CO	1	0	0	0	0	0	0	0
CO_2	0	1	0	0	0	0	0	0
OH	0	0	0	0	1	0	0	0
H	0	0	0	0	0	0	0	0
H_2O	0	0	1	0	0	0	0	1
N	0	0	0	0	0	0	0	0
N_2	0	0	0	1	0	0	0	0
C_2	0	0	0	0	0	1	0	0
H_2	0	0	0	0	0	0	1	0

Table 3.49: Stoichiometric matrix for the reactants in the recombination chemistry model ($\hat{\nu}^{(i,j)}$): RDX

Species \ Reaction	1	2	3	4	5	6	7	8
C	1	0	0	0	0	2	0	0
O	1	1	0	0	1	0	0	1
CO	0	1	0	0	0	0	0	0
CO_2	0	0	0	0	0	0	0	0
OH	0	0	1	0	0	0	0	0
H	0	0	1	0	1	0	2	0
H_2O	0	0	0	0	0	0	0	0
N	0	0	0	2	0	0	0	0
N_2	0	0	0	0	0	0	0	0
C_2	0	0	0	0	0	0	0	0
H_2	0	0	0	0	0	0	0	1

Table 3.50: Fit reaction rate coefficients, temperature exponents, and reaction orders (recombination chemistry model): RDX

Reaction (j)	$k^{(j)}$ $\left(\frac{moles}{cm^3}\right)^{1-m^{(j)}}$	$\gamma^{(j)}$	$m^{(j)}$
1	436.891	1.17437	2
2	924.001	2.27523	2
3	2184.88	2.79995	2
4	4.29675	1.21881	1
5	64.0264	0.32714	2
6	2.64239	2.56523	2
7	1.91827	2.05726	1
8	1043.46	2.79799	2

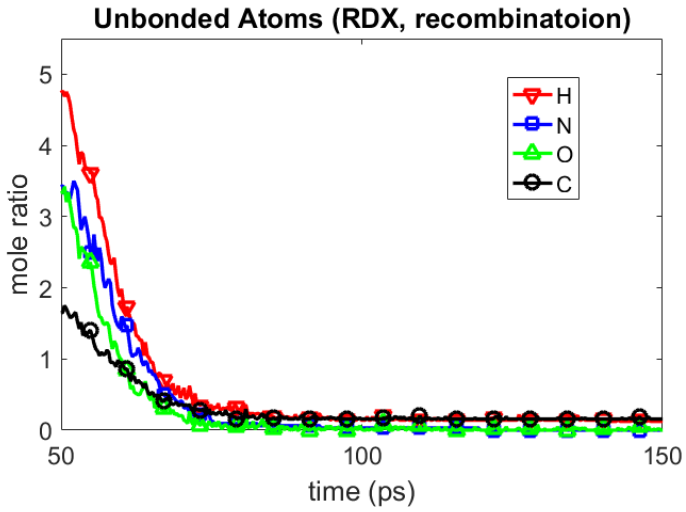

Figure 3.67: Concentration of unbonded atoms versus time (RDX, recombination)

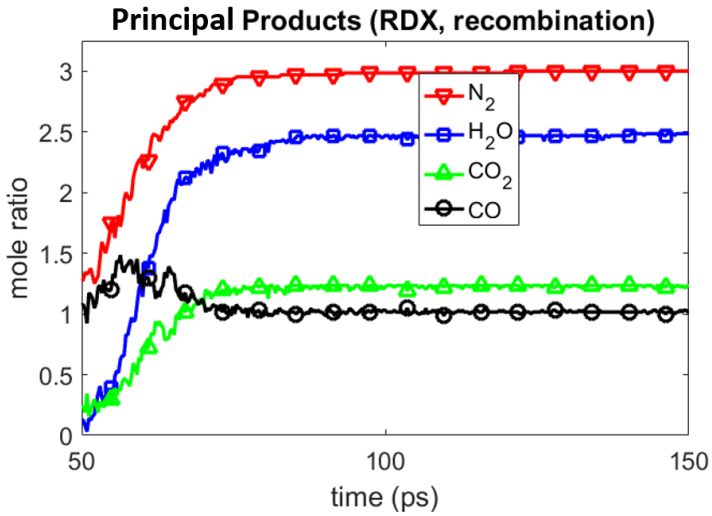

Figure 3.68: Concentration of principal end products versus time (RDX, recombination)

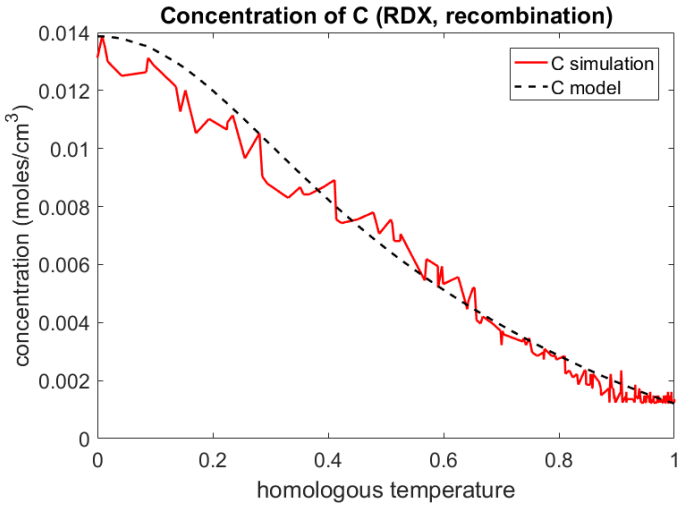

Figure 3.69: Concentration of C versus homologous temperature (RMD simulation and recombination chemistry model): RDX

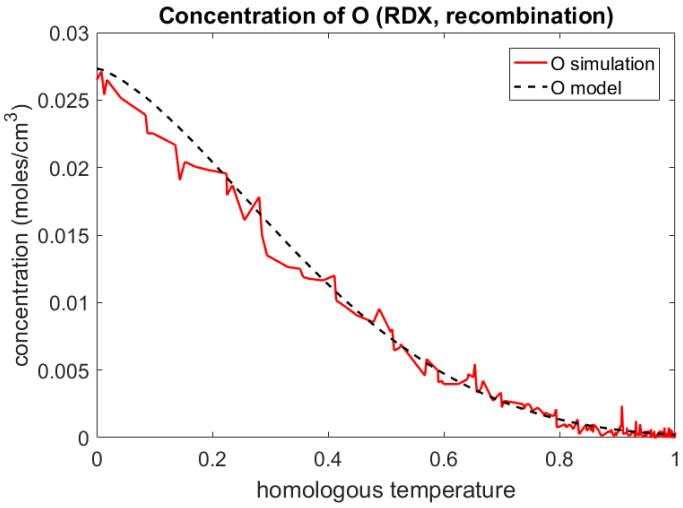

Figure 3.70: Concentration of O versus homologous temperature (RMD simulation and recombination chemistry model): RDX

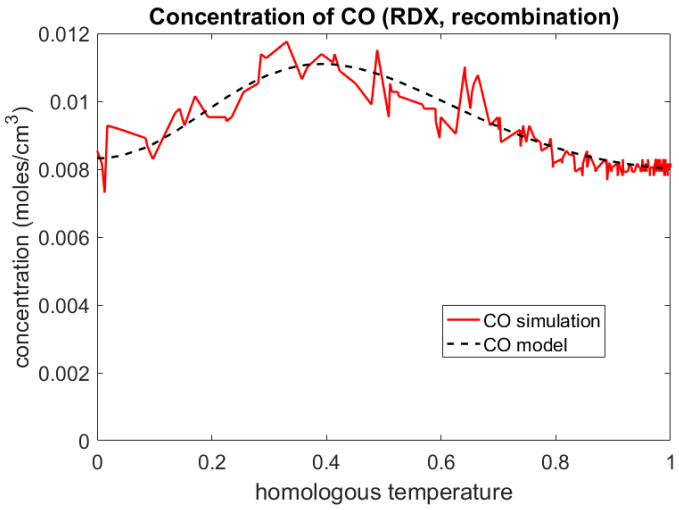

Figure 3.71: Concentration of CO versus homologous temperature (RMD simulation and recombination chemistry model): RDX

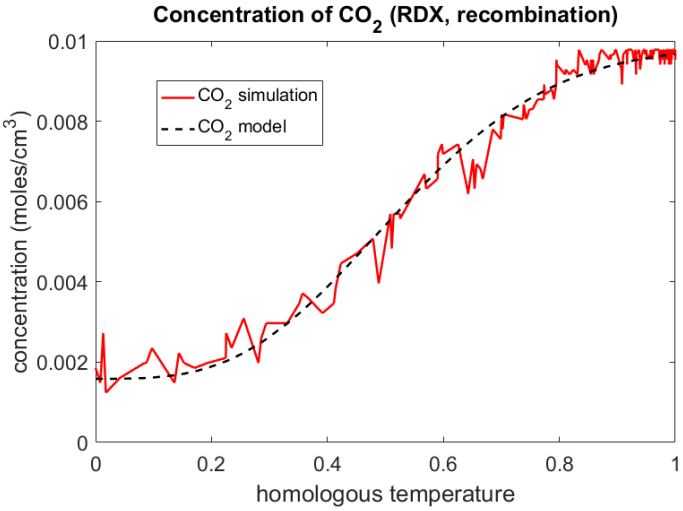

Figure 3.72: Concentration of CO_2 versus homologous temperature (RMD simulation and recombination chemistry model): RDX

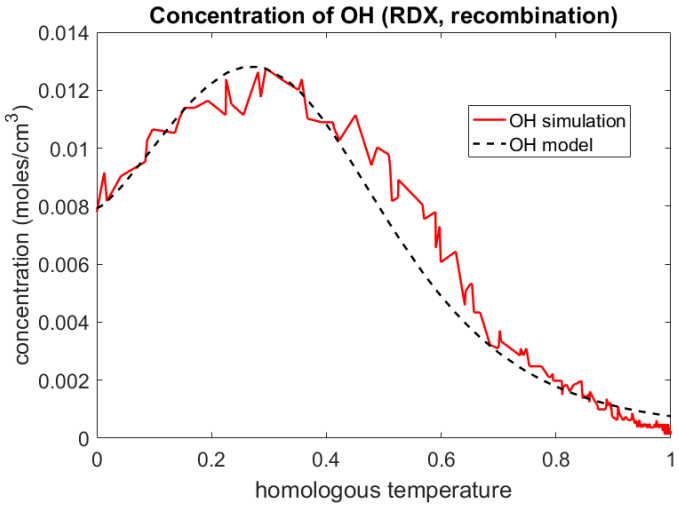

Figure 3.73: Concentration of OH versus homologous temperature (RMD simulation and recombination chemistry model): RDX

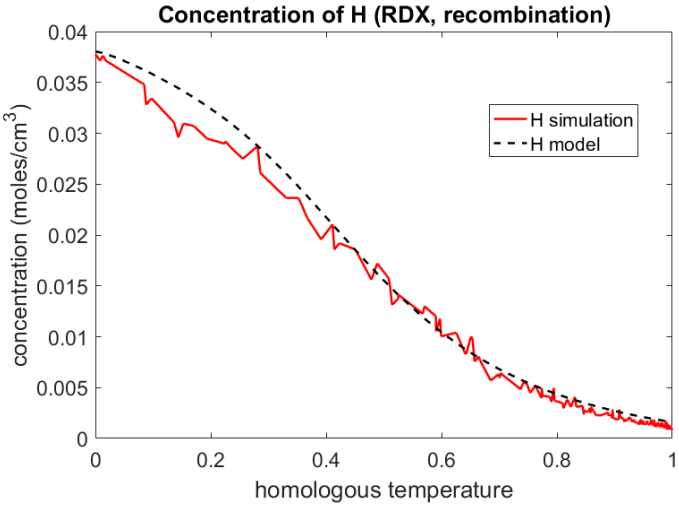

Figure 3.74: Concentration of H versus homologous temperature (RMD simulation and recombination chemistry model): RDX

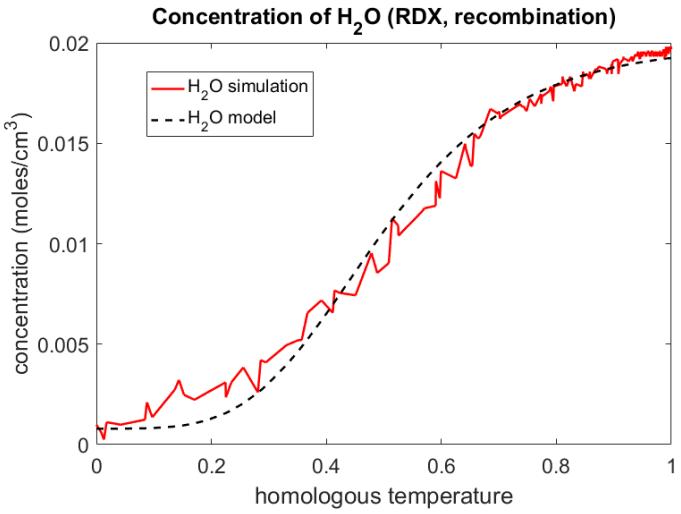

Figure 3.75: Concentration of H_2O versus homologous temperature(RMD simulation and recombination chemistry model): RDX

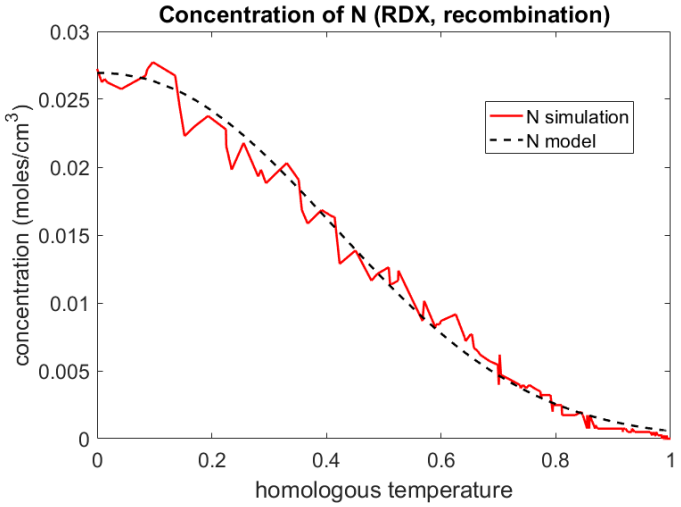

Figure 3.76: Concentration of N versus homologous temperature (RMD simulation and recombination chemistry model): RDX

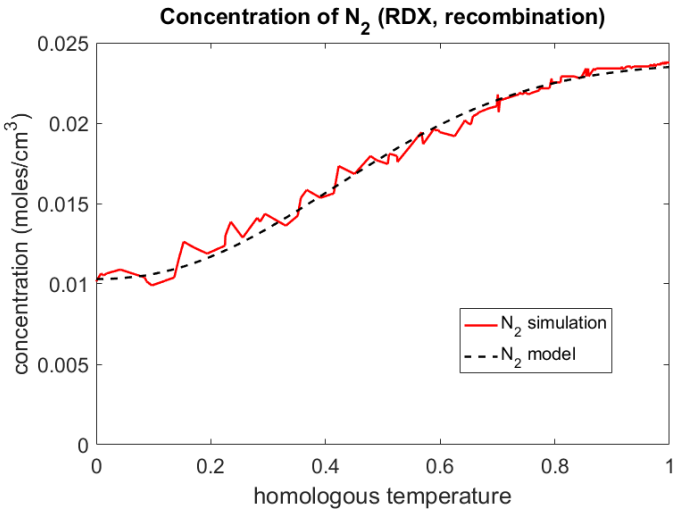

Figure 3.77: Concentration of N_2 versus homologous temperature (RMD simulation and recombination chemistry model): RDX

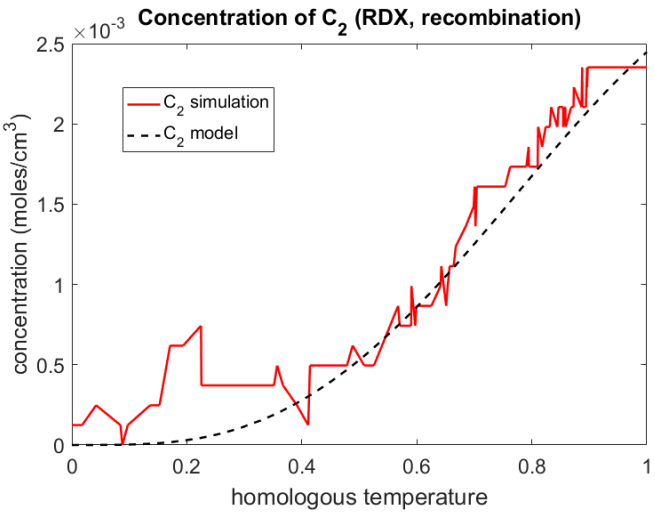

Figure 3.78: Concentration of C_2 versus homologous temperature (RMD simulation and recombination chemistry model): RDX

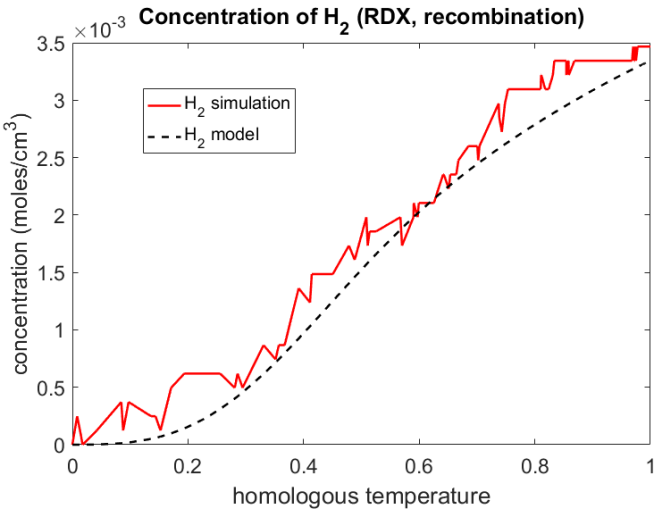

Figure 3.79: Concentration of H_2 versus homologous temperature (RMD simulation and recombination chemistry model): RDX

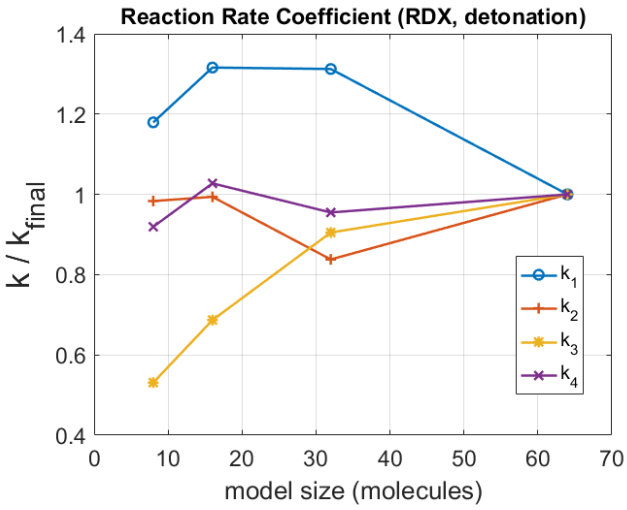

Figure 3.80: Reaction rate coefficients versus model size (detonation chemistry model): RDX

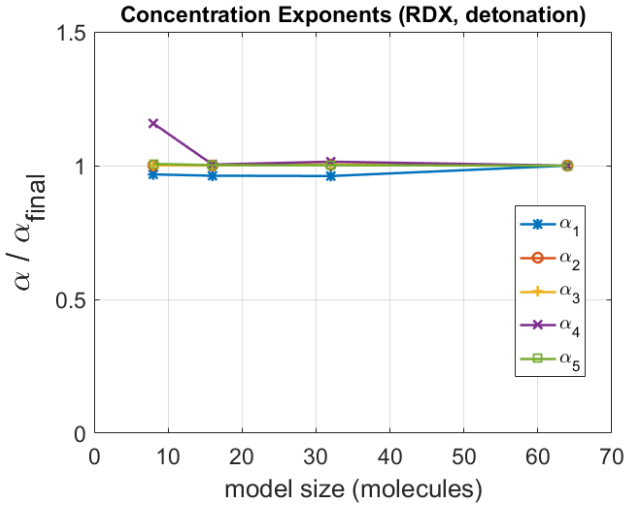

Figure 3.81: Concentration exponents versus model size (detonation chemistry model): RDX

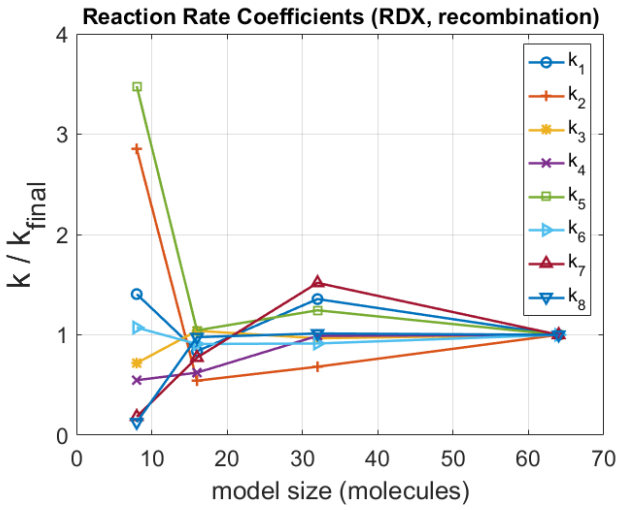

Figure 3.82: Reaction rate coefficients versus model size (recombination chemistry model): RDX

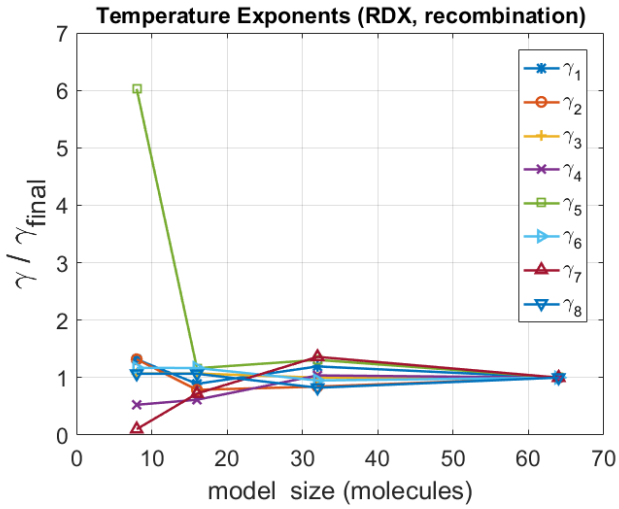

Figure 3.83: Homologous temperature exponents versus model size (recombination chemistry model): RDX

Chapter 4

Conclusions and Recommendations

This work extends the state of the art in reacting molecular dynamics, introducing the first nonholonomic Hamiltonian modeling methodology. It presents a simple NVE formulation as well as a very general formulation capable of modeling NVE, NVT, and other ensembles. Previous work's use of potential-based methods to represent molecular scale chemistry has important disadvantages: (1) the breaking and forming of bonds is implied, not modeled, so that predictions of reacted states can be ambiguous, (2) the development of potential functions capable of representing complex chemistry has proven to be quite difficult, and (3) transient processes of central interest in stability and sensitivity studies are not directly represented in the numerical simulation. In the novel approach presented in this dissertation, the conventional holonomic Hamiltonian (potential based) formulation widely used for molecular scale simulation of reacting shocks is replaced by a nonholonomic formulation, incorporating rate dependent constraints. These constraints describe explicitly the reaction kinetics at the molecular scale, in terms of evolution equations for the breaking and forming of covalent bonds. The formulation rigorously satisfies the first and second laws of thermodynamics under conditions of general thermal and mechanical interaction with the external environment, and

offers important advantages: (1) simple pseudo-potentials replace the enormously complex reacting potentials required in holonomic formulations, (2) important nonlinearities such as a temperature or pressure dependent bond stiffness may be represented, (3) the explicit representation of bonded states eliminates ambiguities in species concentrations, and (4) transient processes of central interest in stability and sensitivity studies are directly simulated in the numerical model. The general RMD formulation presented in Chapter 3 is validated by comparing detonation simulation results for RDX and HMX to published experimental data. Using the RMD simulations, chemical kinetics models are derived which can be used to incorporate the predicted chemistry into models formulated at higher scales. Figures 4.1 through 4.3 plot the computational cost [68] of the validation simulations, as a function of atom count (n), for simulations performed on 16 cores. The results suggest that the computational cost increases at a rate greater than $\mathrm{O}(n)$ but less than $\mathrm{O}(n^2)$.

There are significant opportunities for future work. One is to apply and validate the formulation for other ensembles. An example is the Gibbs ensemble, which holds constant atom number and type, temperature, and pressure. Future work should also consider: (1) the possibility of employing implicit integration schemes [39, 120], in the hope of reducing computational cost, (2) validation against additional explosives (e.g. TNT), and (3) the introduction of bond order time constants which vary with bond type. The formulation might also be extended by the incorporation of three and four body potential energy terms. With respect to practical applications, this research offers im-

portant opportunities for the use of computation to assist in the design of new insensitive energetic materials. Potential applications of the method include: (1) the comparison of detonation simulations for sensitive and insensitive explosives, to investigate whether or not detonation mechanisms may be used to characterize or predict explosive sensitivity, and (2) incorporation of kinetics models developed from RMD simulations into higher scale reacting shock physics applications. Other applications for this modeling work in energetic materials design include the development of 'green' explosive materials, which are of considerable environmental interest. Although further methods development work is needed, the modeling approach presented here departs radically form previous work, and as a result opens major computational methods development opportunities.

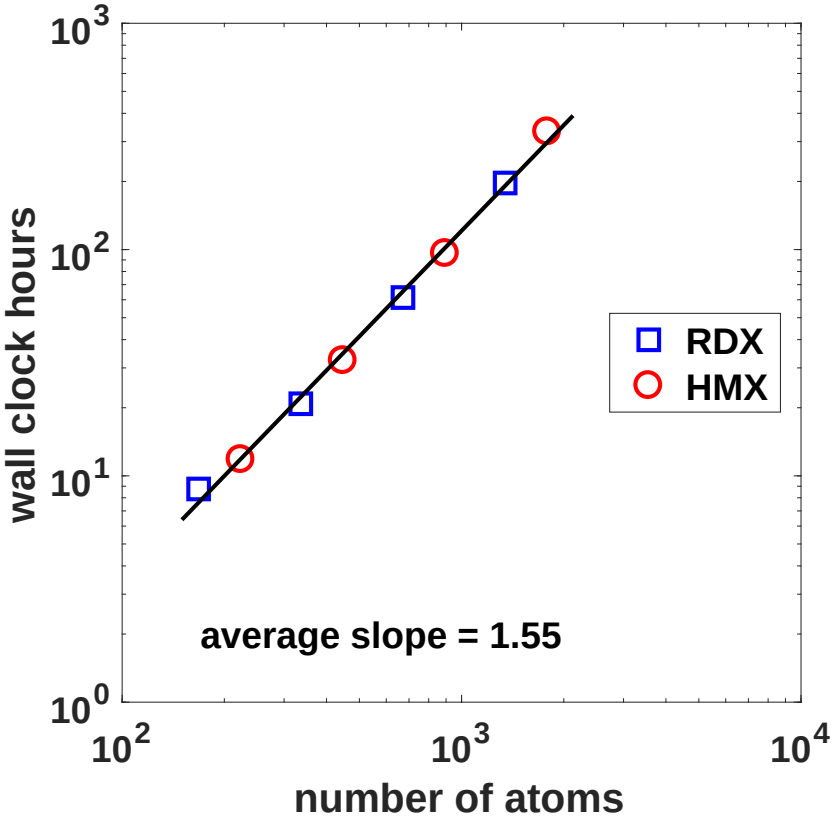

Figure 4.1: Formulation scale up (wall clock hours versus number of atoms)

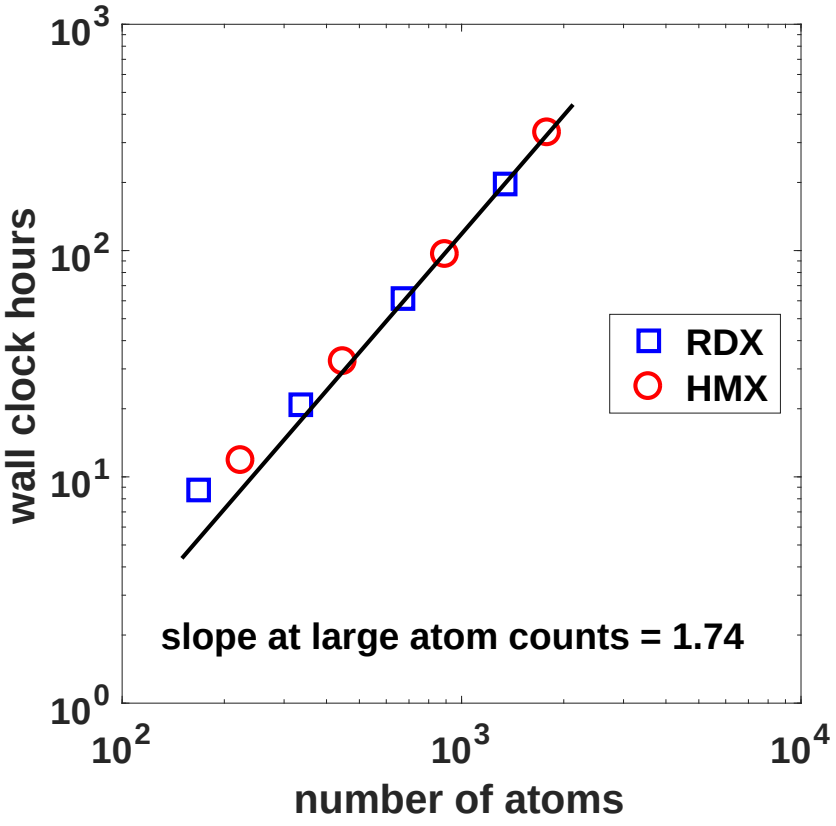

Figure 4.2: Formulation scale up (wall clock hours versus number of atoms)

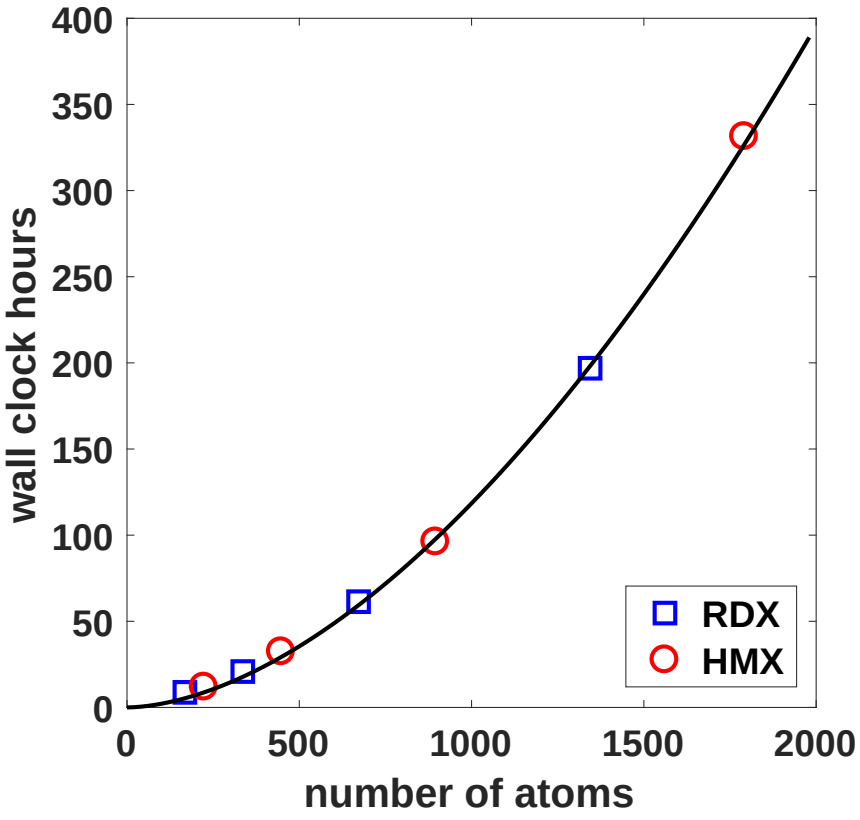

Figure 4.3: Formulation scale up (wall clock hours versus number of atoms)

Appendices

Appendix A

Variable Transformations: Chemistry Models

A.1 Variable Transformation

The following variable transformation is applicable to the detonation and recombination chemistry models.

$$\zeta^{(j)} = \hat{\zeta}^{(j)} C_o, \quad C_s = \hat{C}_s C_o \tag{A.1}$$

where C_o is a reference concentration in units of moles per cubic centimeter. In the transformed model the reaction rate coefficient is

$$\hat{k}^{(j)} = k^{(j)} C_o^{(m^{(j)}-1)} \tag{A.2}$$

The units of the untransformed reaction rate coefficient $k^{(j)}$, in both the detonation and recombination chemistry models, vary as a function of the reaction order, $m^{(j)}$. The units of the transformed reaction rate coefficient, $\hat{k}^{(j)}$, are the same for all reactions.

A.2 Variable Transformation: Detonation Chemistry Model

Applying the transformations from equations A.1 and A.2 to the detonation chemistry model of equation 3.70:

$$\frac{d\hat{C}_i}{dt} = \sum_{j=1}^{N} \left(\nu^{(i,j)} - \hat{\nu}^{(i,j)}\right) \hat{\zeta}^{(j)}, \quad \hat{\zeta}^{(j)} = \left(\frac{\rho}{\rho_o}\right)^{1-m^{(j)}} \hat{k}^{(j)} \prod_{s=1}^{n} \hat{C}_s^{\alpha^{(s,j)}} \tag{A.3}$$

The units of the transformed reaction rate coefficient are ps^{-1}. Using the concentration of solid α-RDX (0.0079 moles per cubic centimeter) and β -HMX (0.0064 moles per cubic centimeter) for C_o, the transformed reaction rate coefficients are shown in Table A.1 for HMX and in Table A.2 for RDX.

A.3 Variable Transformation: Recombination Chemistry Model

The variable transformations in equations A.1 and A.2, when applied to the recombination chemistry model (equation 3.72), produces

$$\frac{d\hat{C}_i}{d\theta_H} = \sum_{j=1}^{N} \left(\nu^{(i,j)} - \hat{\nu}^{(i,j)}\right)\hat{\zeta}^{(j)}, \quad \hat{\zeta}^{(j)} = \left(\frac{\rho}{\rho_o}\right)^{1-m^{(j)}} \hat{k}^{(j)}\theta_H^{\gamma^{(j)}} \prod_{s=1}^{n} \hat{C}_s^{\alpha^{(s,j)}} \tag{A.4}$$

The transformed reaction rate coefficient $\hat{k}$ in the recombination chemistry model is dimensionless. Using the concentration of solid α-RDX (0.0079 moles per cubic centimeter) and β -HMX (0.0064 moles per cubic centimeter) for C_o, the transformed reaction rate coefficient values for the recombination chemistry model are shown in Table A.3 for HMX and in Table A.4 for RDX.

Table A.1: Transformed $k^{(j)}$ (detonation chemistry model): HMX

Reaction	$\hat{k}^{(j)}\ (ps)^{-1}$
1	12.49
2	0.94
3	2.90
4	7.70

Table A.2: Transformed $k^{(j)}$ (detonation chemistry model): RDX

Reaction	$\hat{k}^{(j)}\ (ps)^{-1}$
1	4.94
2	3.95
3	1.42
4	1.45

Table A.3: Transformed $k^{(j)}$ (recombination chemistry model): HMX

Reaction	$\hat{k}^{(j)}$
1	3.97
2	9.27
3	6.78
4	2.31
5	0.53
6	15.08
7	2.39
8	0.34
9	0.0001

Table A.4: Transformed $k^{(j)}$ (recombination chemistry model): RDX

Reaction	$\hat{k}^{(j)}$
1	3.46
2	7.32
3	17.31
4	4.30
5	0.51
6	2.64
7	1.92
8	8.27

Appendix B

Recombination Chemistry: Time Domain

B.1 Recombination Chemistry Model: Time Domain

The transient recombination chemistry model takes the form

$$\frac{dC}{dt} = \left(\frac{dC}{d\theta_H}\right)\left(\frac{d\theta_H}{d\theta}\right)\left(\frac{d\theta}{dt}\right) \tag{B.1}$$

where $\frac{d\theta_H}{d\theta}$ and $\frac{d\theta}{dt}$ may come from RMD or from higher scale models. The function $\frac{dC}{d\theta_H}$ represents the recombination chemistry model formulated in section 3.2.2 and parameterized for HMX and RDX in sections 3.3.2 and 3.3.4 respectively. In the following discussion, $\frac{d\theta_H}{d\theta}$ and $\frac{d\theta}{dt}$ come from the RMD simulation; the time domain kinetics model can then be integrated and compared directly to the RMD concentration versus time simulation data.

The homologous temperature is defined as

$$\theta_H = \frac{\theta_{max} - \theta}{\theta_{max} - \theta_{min}} \tag{B.2}$$

therefore

$$\frac{d\theta_H}{d\theta} = \frac{-1}{\theta_{max} - \theta_{min}} \tag{B.3}$$

The maximum and minimum temperatures (θ_{max} and θ_{min}) are known from the RMD simulation. To calculate $\frac{d\theta}{dt}$ from the RMD simulation data, we fit the temperature versus time data and then differentiate the fitted function.

B.2 Recombination Chemistry in HMX: Time Domain

The minimum and maximum temperatures from the thermostatted portion of the HMX simulation are

$$\theta_{min} = 418.4\ K, \quad \theta_{max} = 9281.3\ K \tag{B.4}$$

The temperature versus time fit in the thermostatted region is shown in Figure B.1. The differentiated fit takes the form

$$\frac{d\theta}{dt} = a\ b\ e^{(b\,t)} + c\ h\ e^{(h\,t)} \tag{B.5}$$

where a=9773, b=-0.07838, c=228, and h=0.008434. The integrated transient recombination chemistry model is compared with the RMD simulation data for HMX in Figures B.2 through B.13. These plots show that the transient recombination chemistry model for HMX is able to reproduce the RMD simulation data.

B.3 Recombination Chemistry in RDX: Time Domain

The minimum and maximum temperatures from the thermostatted portion of the RDX simulation are

$$\theta_{min} = 418.5\ K, \quad \theta_{max} = 9714.6\ K \tag{B.6}$$

The temperature versus time fit in the thermostatted region is shown in Figure B.14. The differentiated fit takes the form

$$\frac{d\theta}{dt} = a\ b\ e^{(b\,t)} + c\ h\ e^{(h\,t)} \tag{B.7}$$

where a=9951, b=-0.0788, c=336.5, and h=0.00364. The integrated transient recombination chemistry model is compared with the RMD simulation data for RDX in Figures B.15 through B.25. These plots show that the transient recombination chemistry model for RDX is able to reproduce the RMD simulation data.

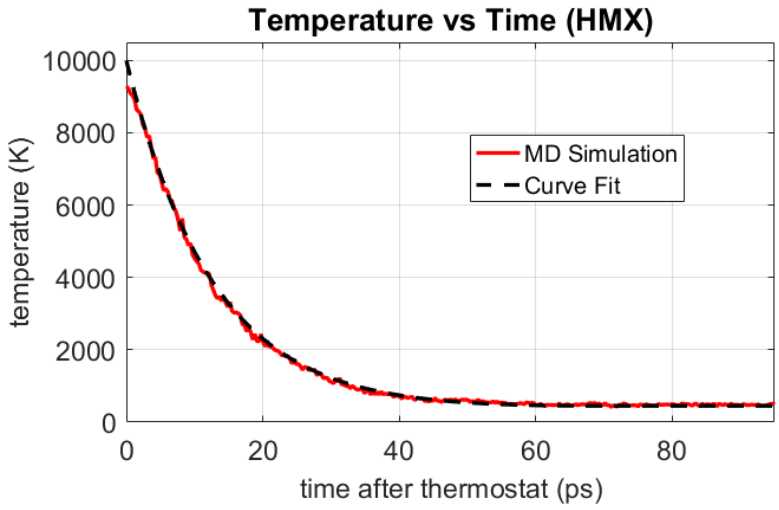

Figure B.1: Temperature versus time fit: HMX

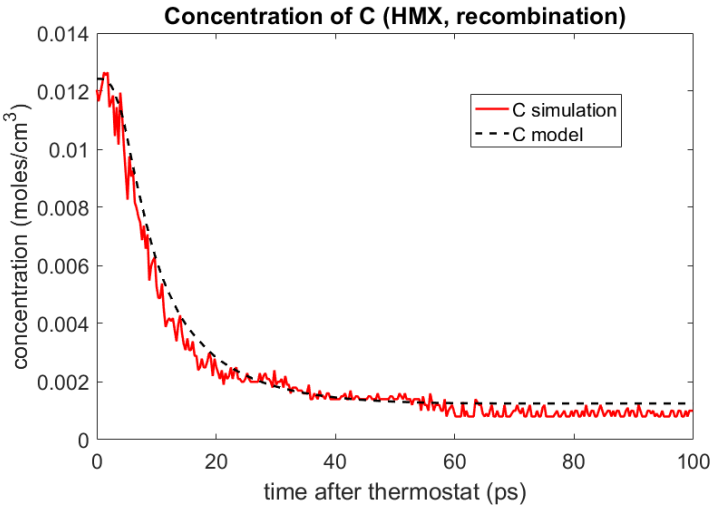

Figure B.2: Concentration of C versus time (RMD simulation and transient recombination chemistry model): HMX

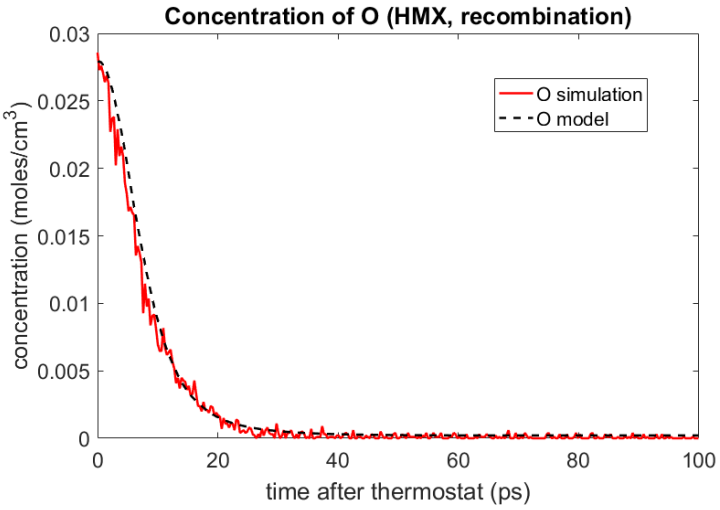

Figure B.3: Concentration of O versus time (RMD simulation and transient recombination chemistry model): HMX

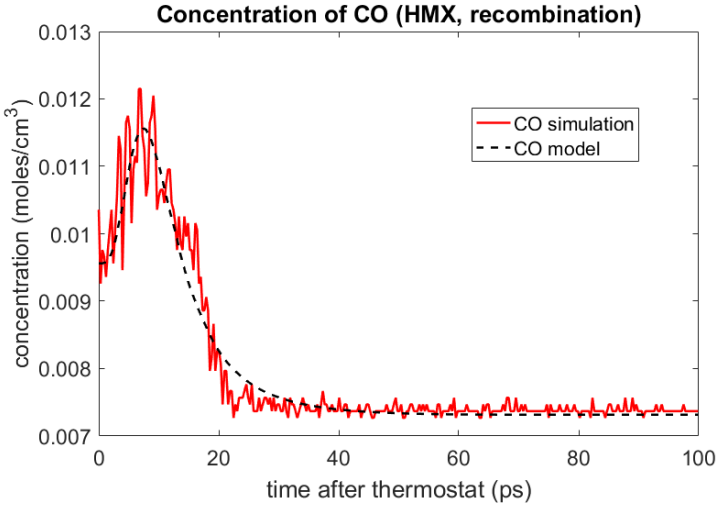

Figure B.4: Concentration of CO versus time (RMD simulation and transient recombination chemistry model): HMX

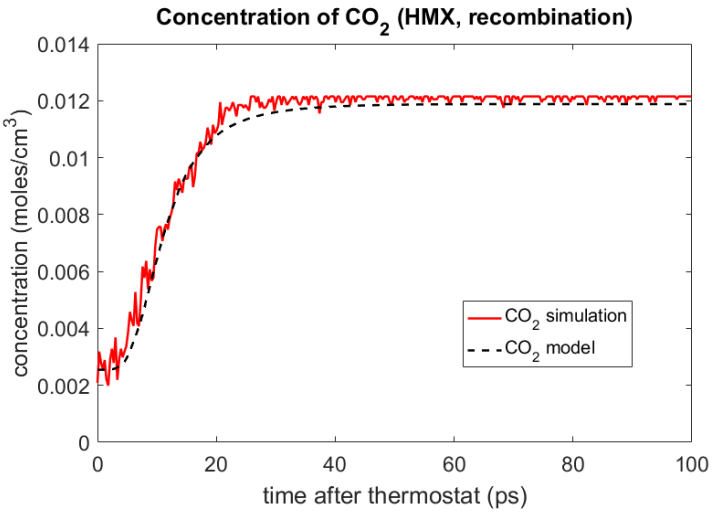

Figure B.5: Concentration of CO_2 versus time (RMD simulation and transient recombination chemistry model): HMX

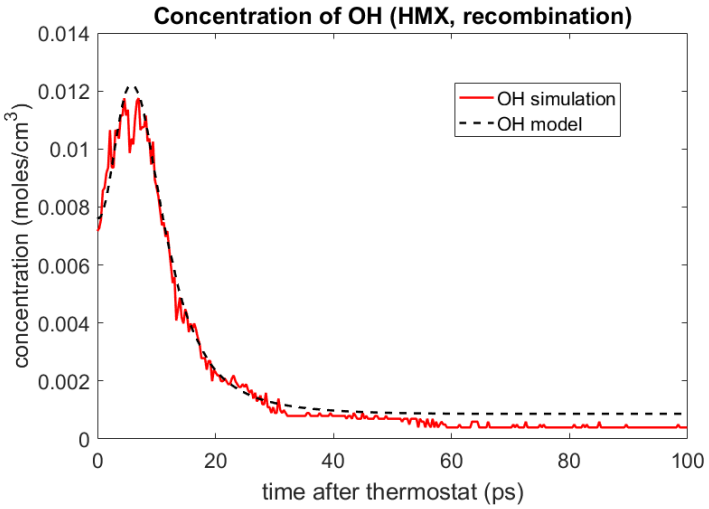

Figure B.6: Concentration of OH versus time (RMD simulation and transient recombination chemistry model): HMX

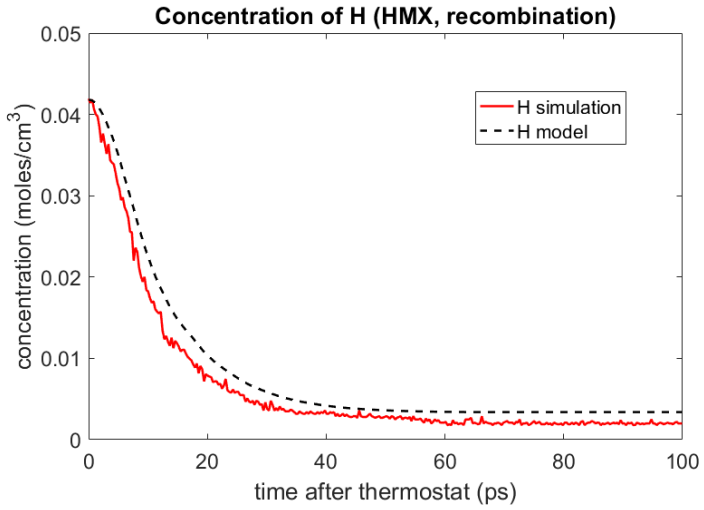

Figure B.7: Concentration of H versus time (RMD simulation and transient recombination chemistry model): HMX

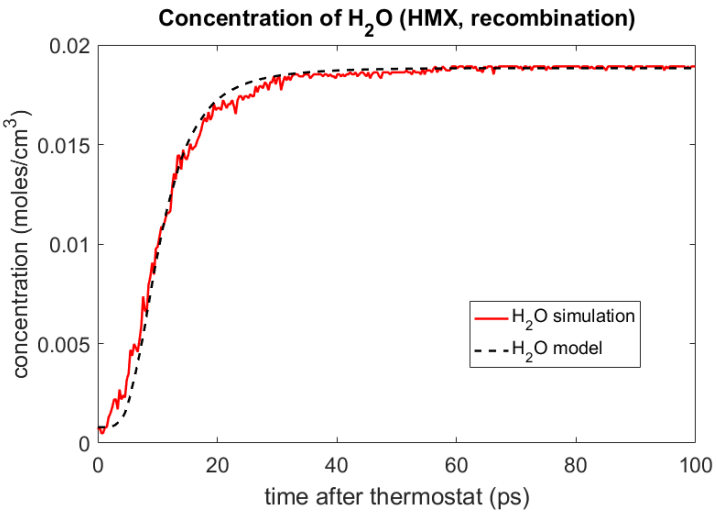

Figure B.8: Concentration of H_2O versus time (RMD simulation and transient recombination chemistry model): HMX

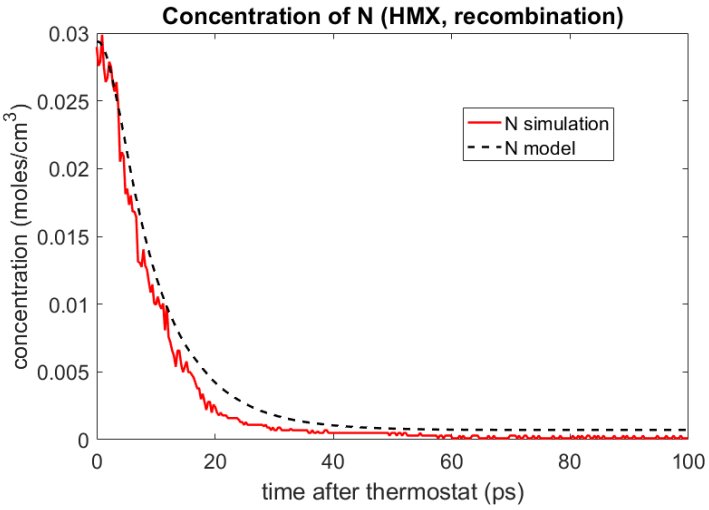

Figure B.9: Concentration of N versus time (RMD simulation and transient recombination chemistry model): HMX

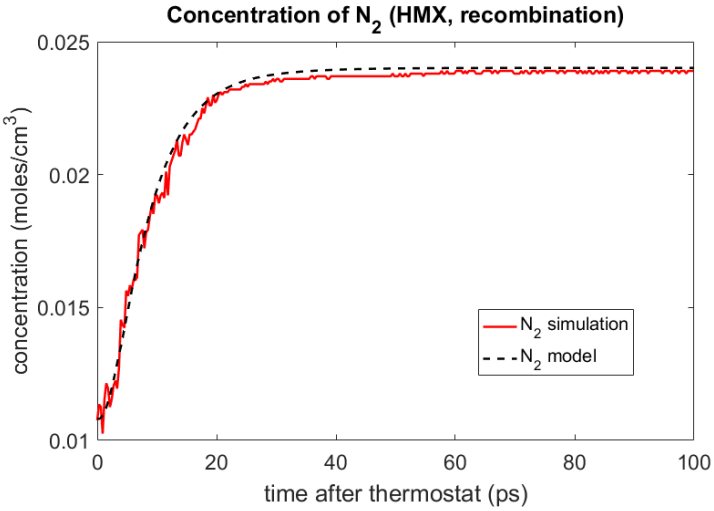

Figure B.10: Concentration of N_2 versus time (RMD simulation and transient recombination chemistry model): HMX

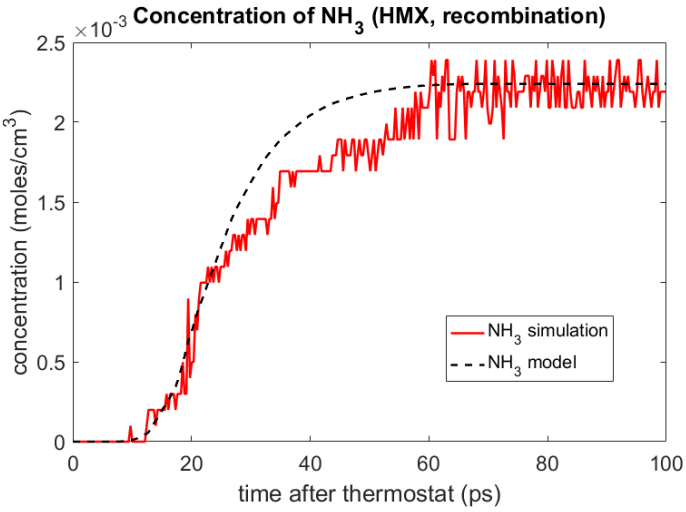

Figure B.11: Concentration of NH_3 versus time (RMD simulation and transient recombination chemistry model): HMX

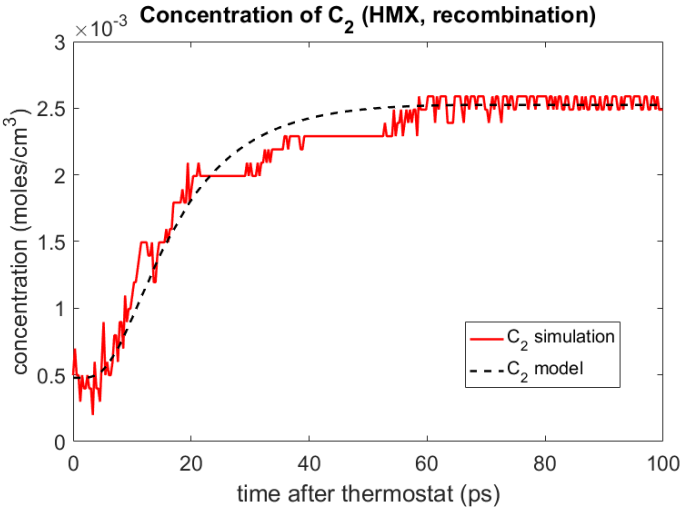

Figure B.12: Concentration of C_2 versus time (RMD simulation and transient recombination chemistry model): HMX

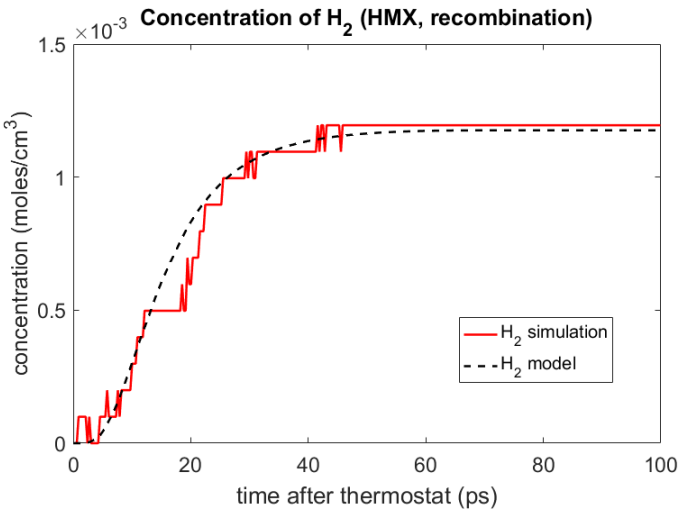

Figure B.13: Concentration of H_2 versus time (RMD simulation and transient recombination chemistry model): HMX

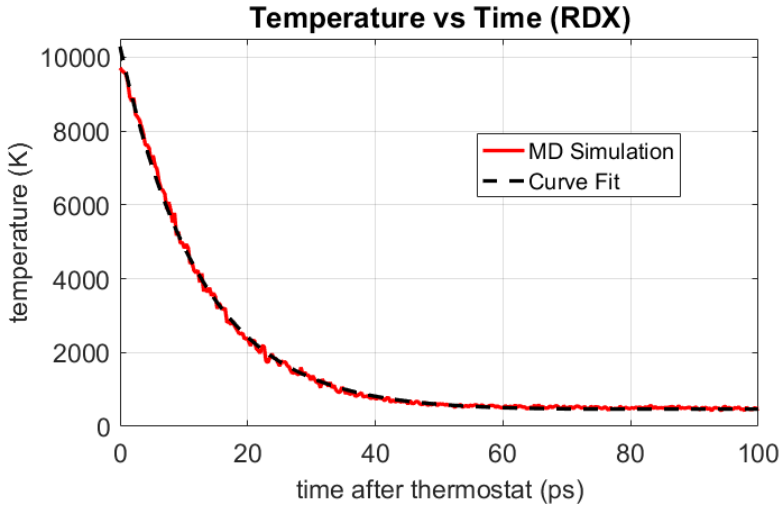

Figure B.14: Temperature versus Time Fit for RDX

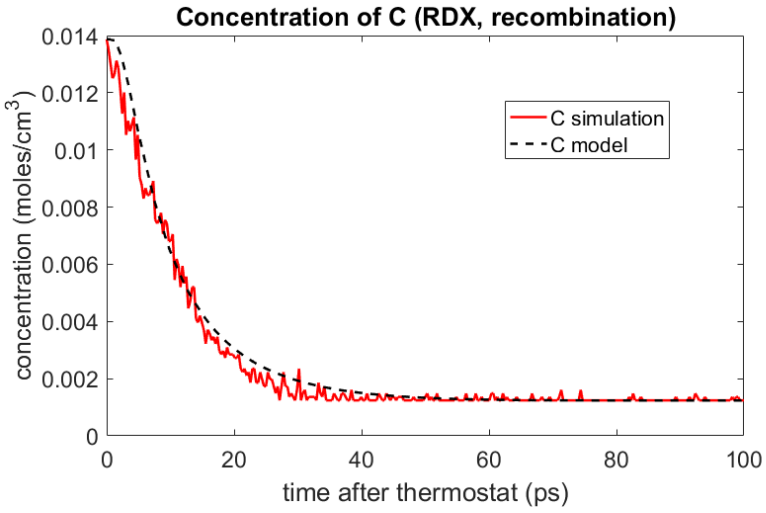

Figure B.15: Concentration of C versus time (RMD simulation and transient recombination chemistry model): RDX

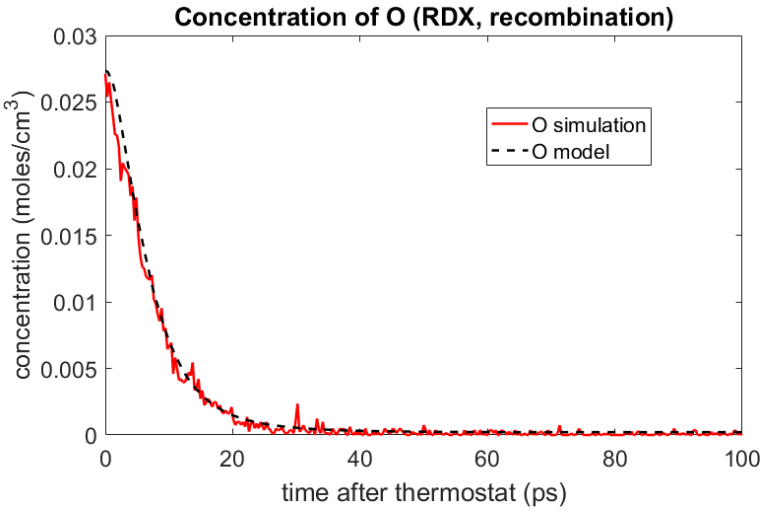

Figure B.16: Concentration of O versus time (RMD simulation and transient recombination chemistry model): RDX

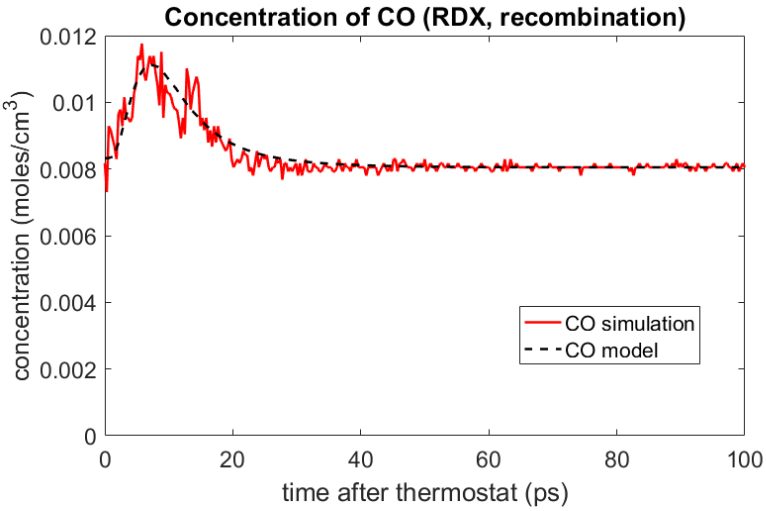

Figure B.17: Concentration of CO versus time (RMD simulation and transient recombination chemistry model): RDX

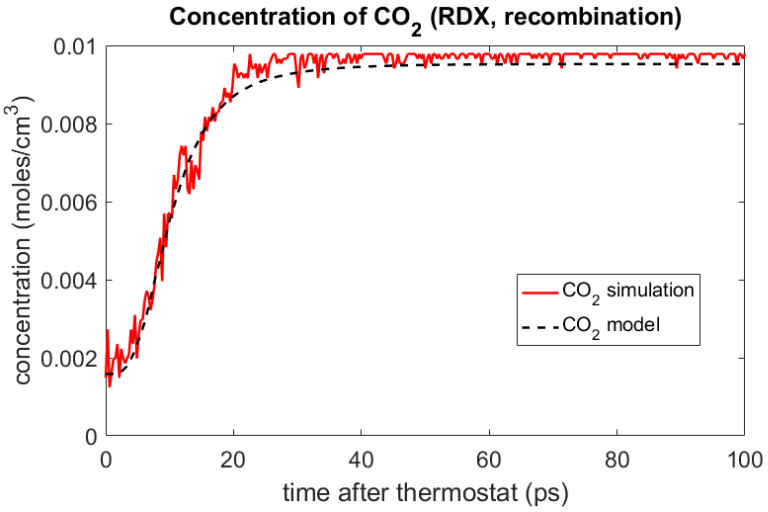

Figure B.18: Concentration of CO_2 versus time (RMD simulation and transient recombination chemistry model): RDX

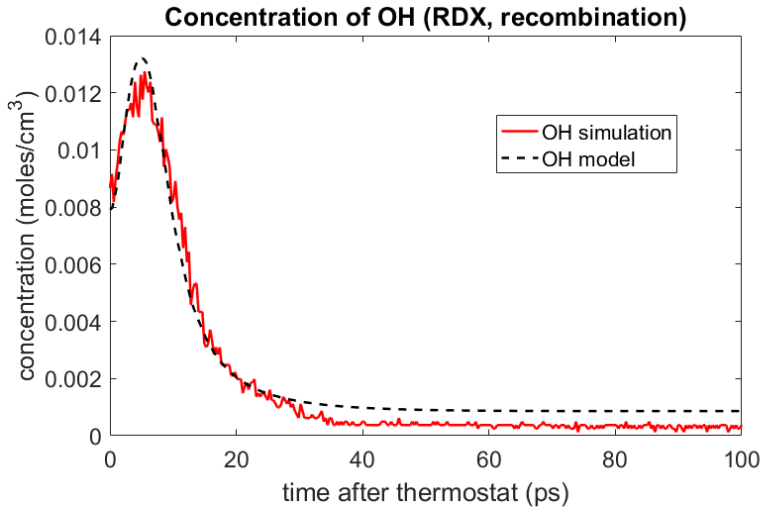

Figure B.19: Concentration of OH versus time (RMD simulation and transient recombination chemistry model): RDX

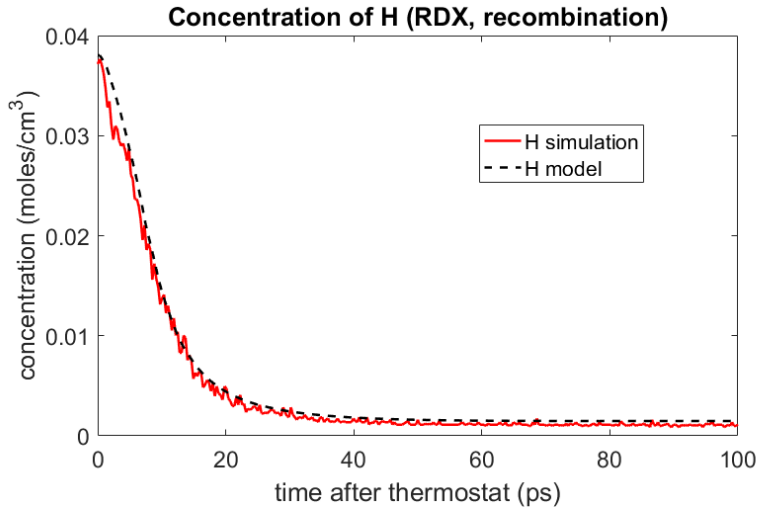

Figure B.20: Concentration of H versus time (RMD simulation and transient recombination chemistry model): RDX

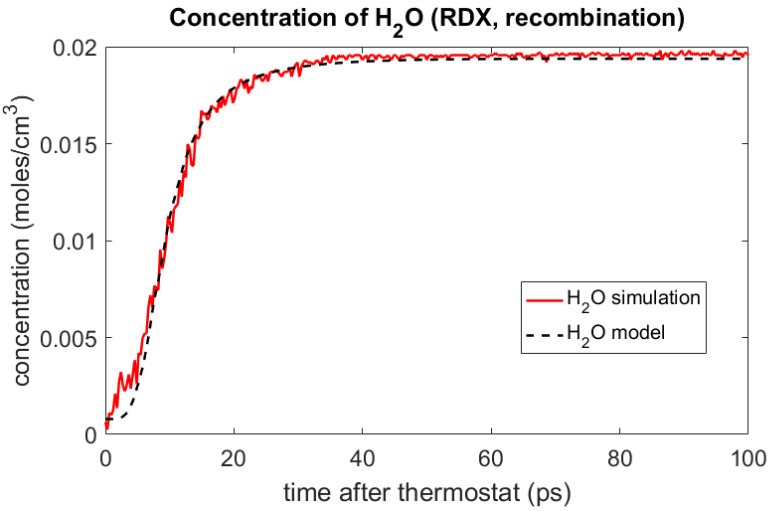

Figure B.21: Concentration of H_2O versus time (RMD simulation and transient recombination chemistry model): RDX

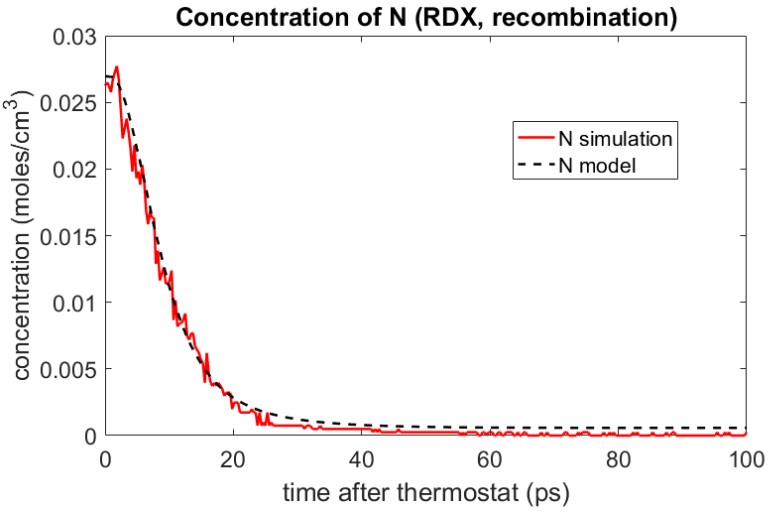

Figure B.22: Concentration of N versus time (RMD simulation and transient recombination chemistry model): RDX

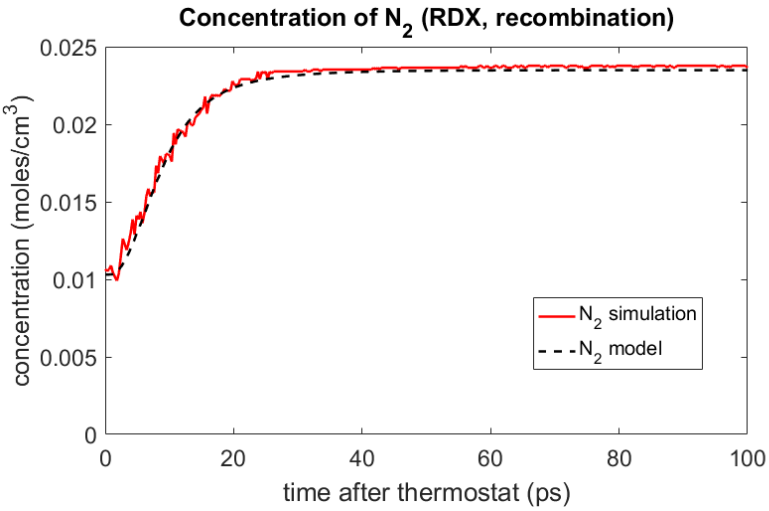

Figure B.23: Concentration of N_2 versus time (RMD simulation and transient recombination chemistry model): RDX

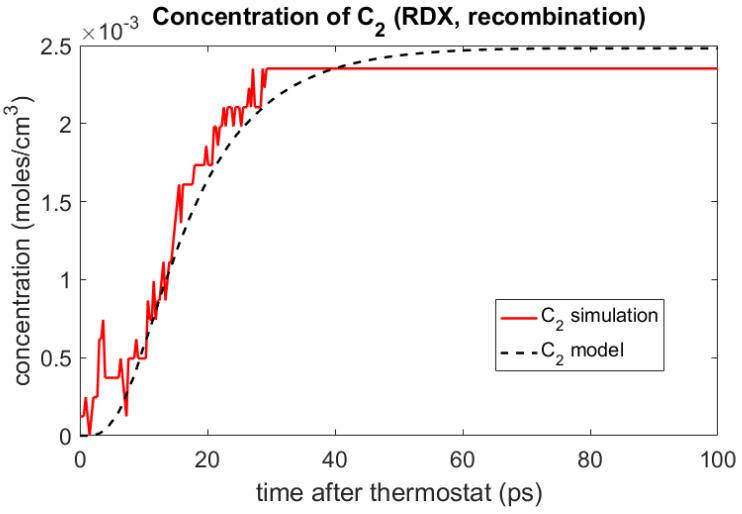

Figure B.24: Concentration of C_2 versus time (RMD simulation and transient recombination chemistry model): RDX

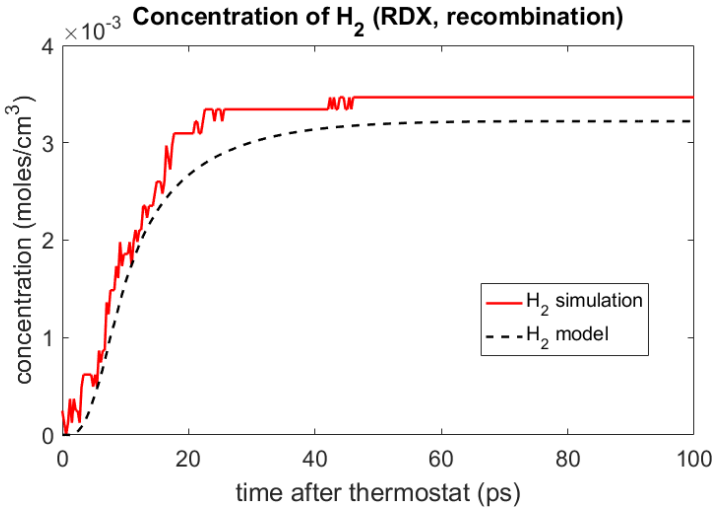

Figure B.25: Concentration of H_2 versus time (RMD simulation and transient recombination chemistry model): RDX

Appendix C

Convergence Plots

C.1 Introduction

This appendix presents plots of computed species concentrations versus model size. The plots are provided to facilitate the review of the numerical data shown in Tables 3.10, 3.11, 3.33, and 3.34.

C.2 Species Convergence Plots: HMX

The data shown in Table 3.10 is presented graphically in Figures C.1 through C.9. The data shown in Table 3.11 is presented graphically in Figures C.10 through C.16

C.3 Species Convergence Plots: RDX

The data shown in Table 3.33 is presented graphically in Figures C.17 through C.25. The data shown in Table 3.34 is presented graphically in Figures C.26 through C.31.

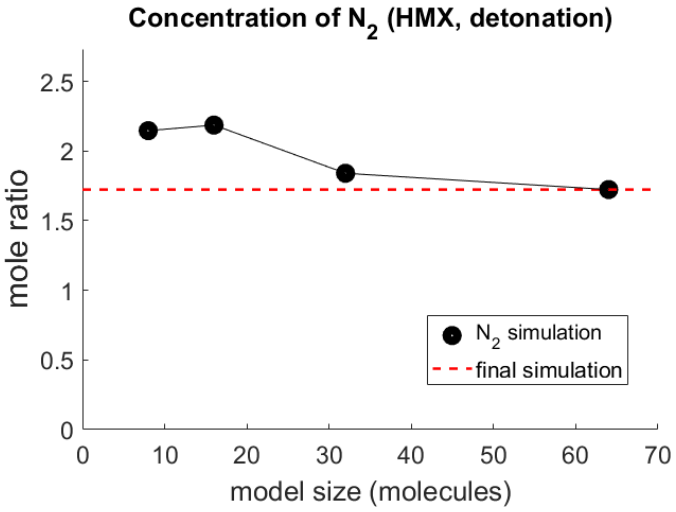

Figure C.1: Concentration of N_2 during steady state versus model size (NVE): HMX

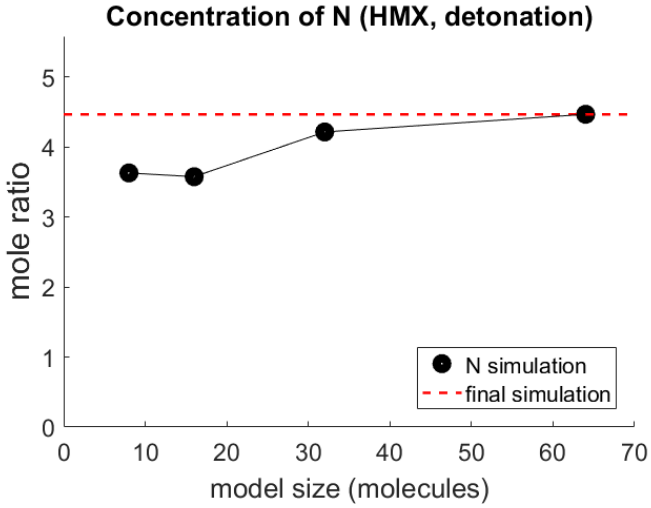

Figure C.2: Concentration of N during steady state versus model size (NVE): HMX

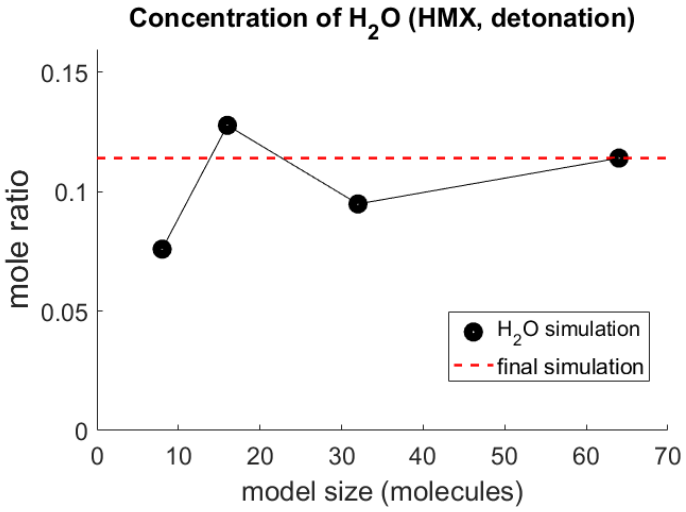

Figure C.3: Concentration of H_2O during steady state versus model size (NVE): HMX

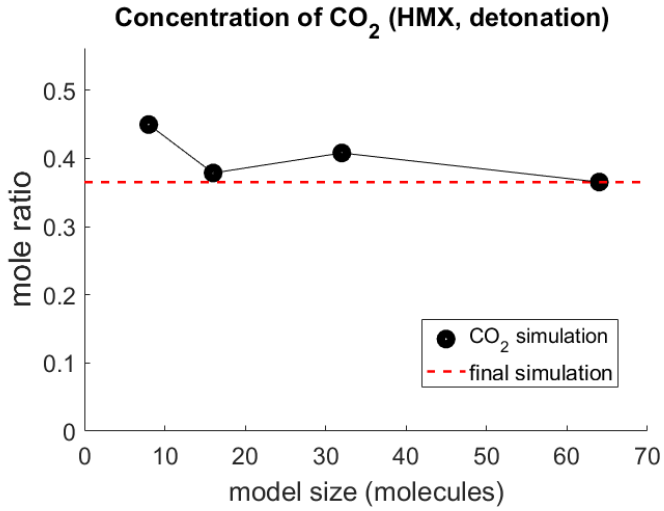

Figure C.4: Concentration of CO_2 during steady state versus model size (NVE): HMX

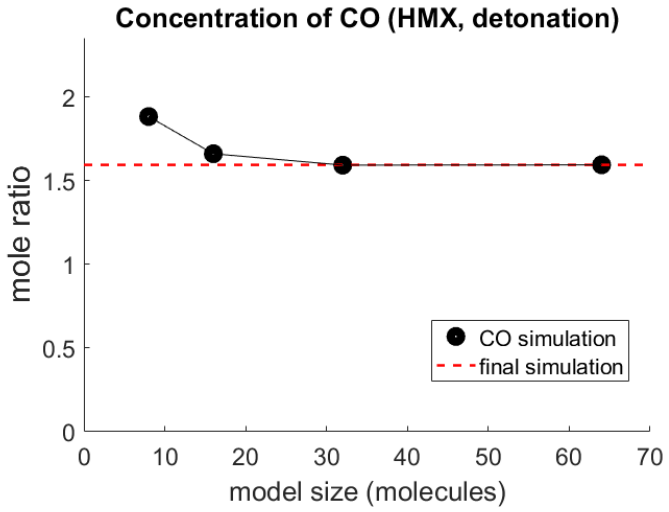

Figure C.5: Concentration of CO during steady state versus model size (NVE): HMX

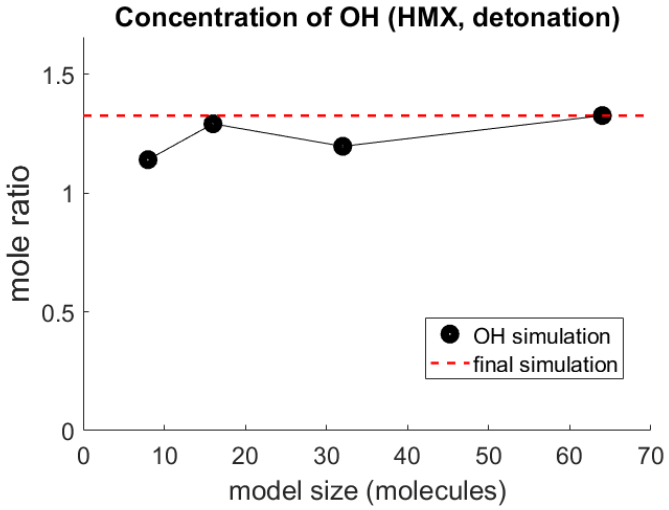

Figure C.6: Concentration of OH during steady state versus model size (NVE): HMX

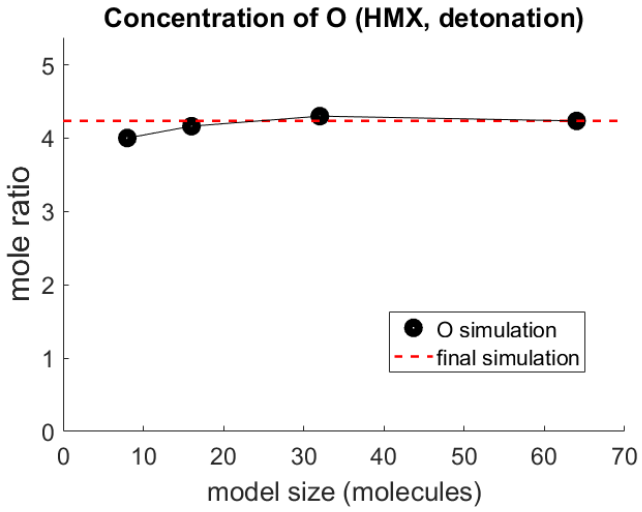

Figure C.7: Concentration of O during steady state versus model size (NVE): HMX

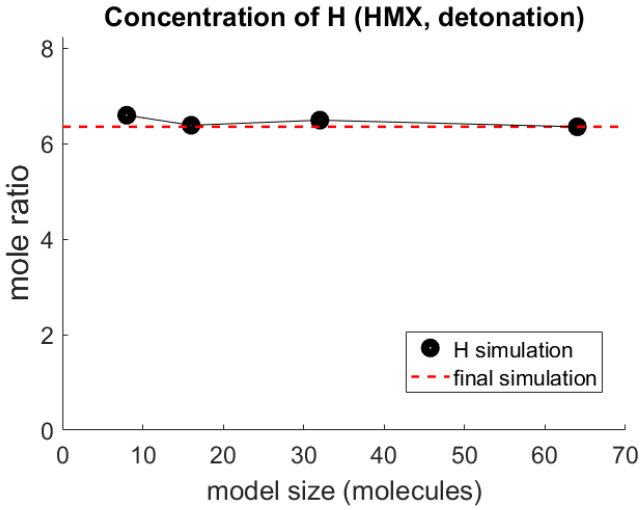

Figure C.8: Concentration of H during steady state versus model size (NVE): HMX

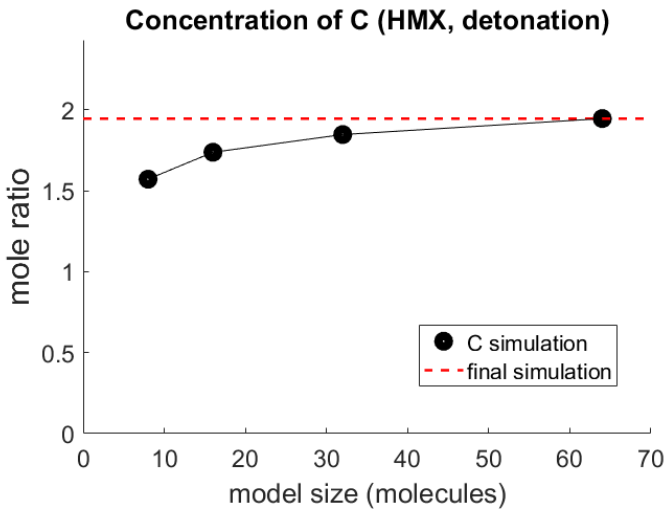

Figure C.9: Concentration of C during steady state versus model size (NVE): HMX

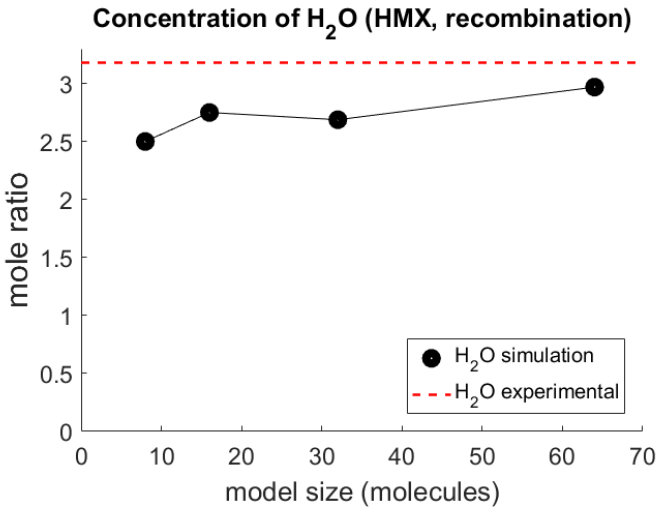

Figure C.10: Product mole ratios for H_2O versus model size: HMX

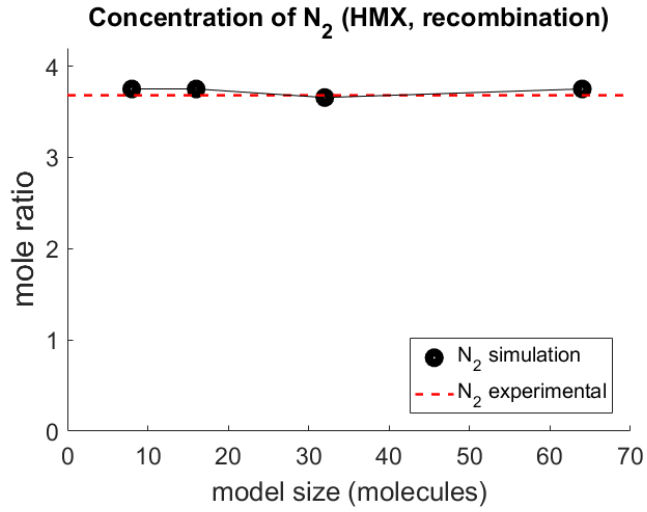

Figure C.11: Product mole ratios for N_2 versus model size: HMX

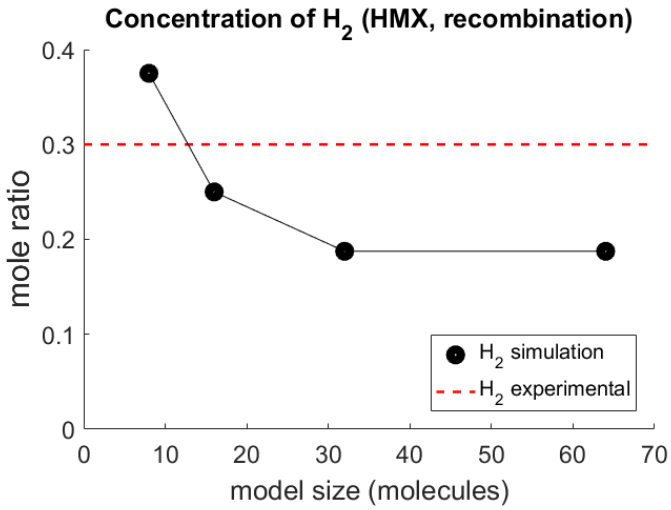

Figure C.12: Product mole ratios for H_2 versus model size: HMX

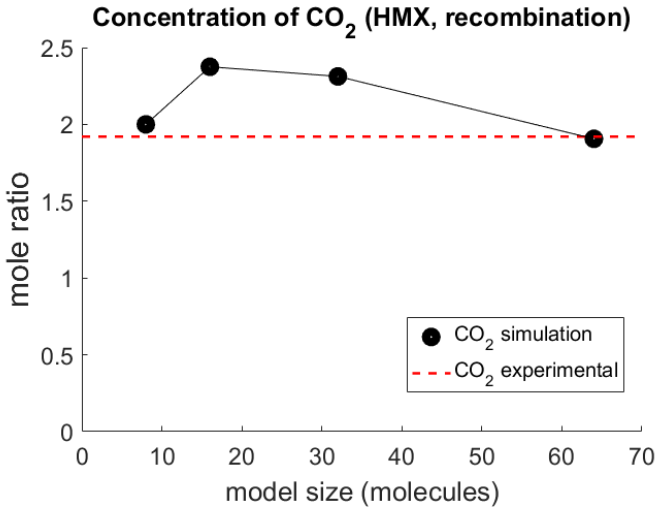

Figure C.13: Product mole ratios for CO_2 versus model size: HMX

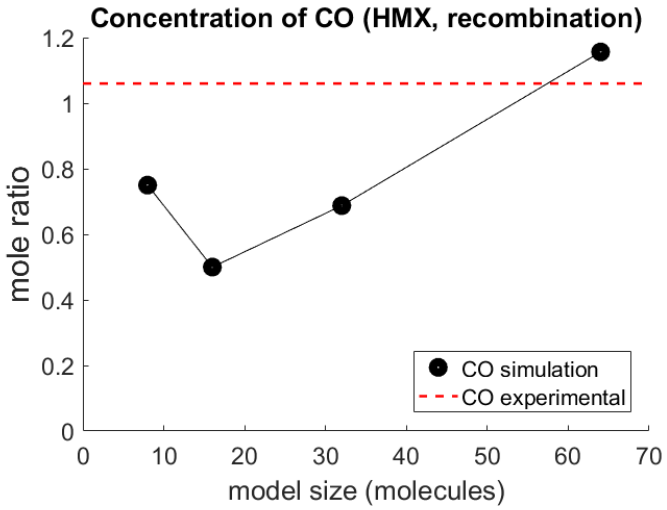

Figure C.14: Product mole ratios for CO versus model size: HMX

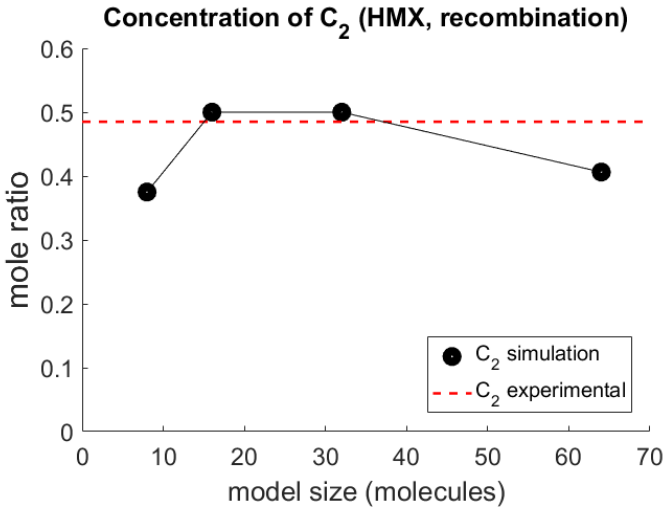

Figure C.15: Product mole ratios for C_2 versus model size: HMX

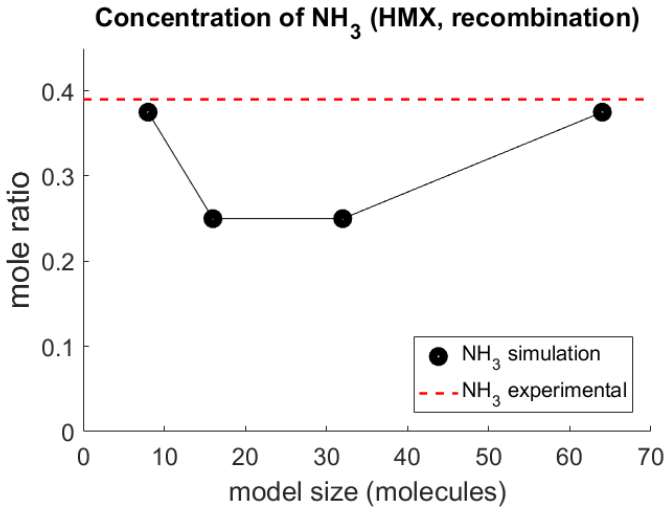

Figure C.16: Product mole ratios for NH_3 versus model size: HMX

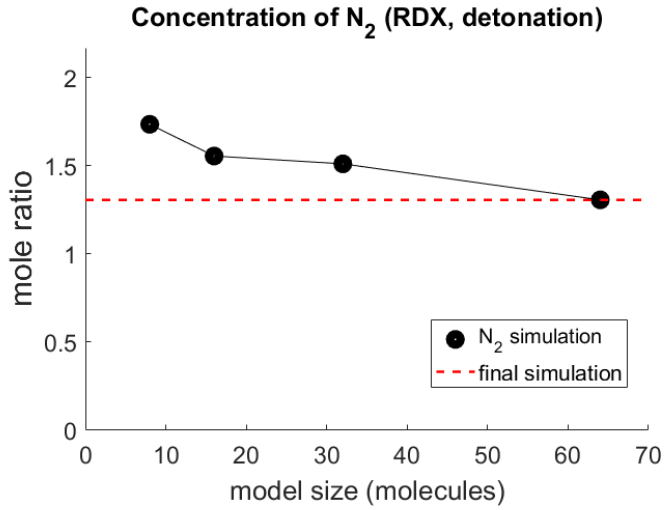

Figure C.17: Concentration of N_2 during steady state versus model size (NVE): RDX

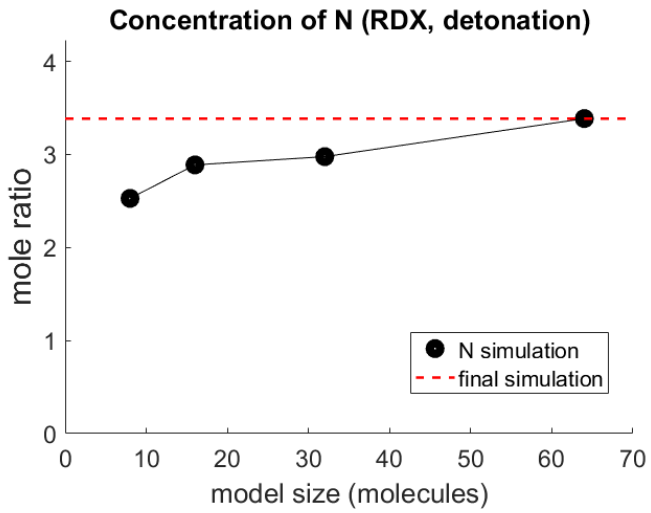

Figure C.18: Concentration of N during steady state versus model size (NVE): RDX

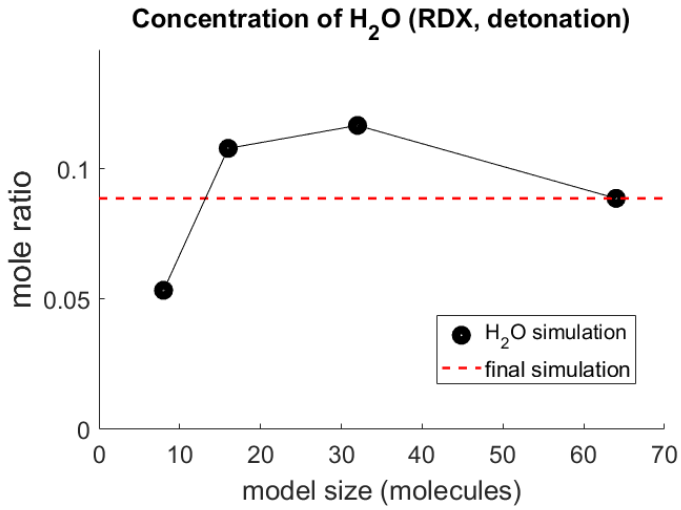

Figure C.19: Concentration of H_2O during steady state versus model size (NVE): RDX

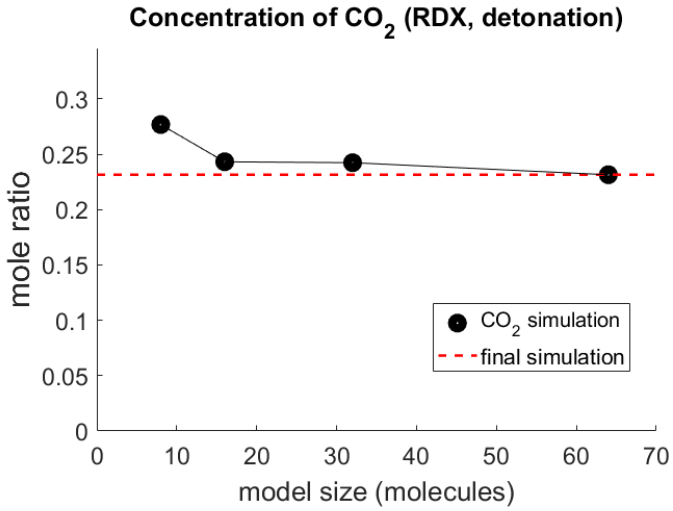

Figure C.20: Concentration of CO_2 during steady state versus model size (NVE): RDX

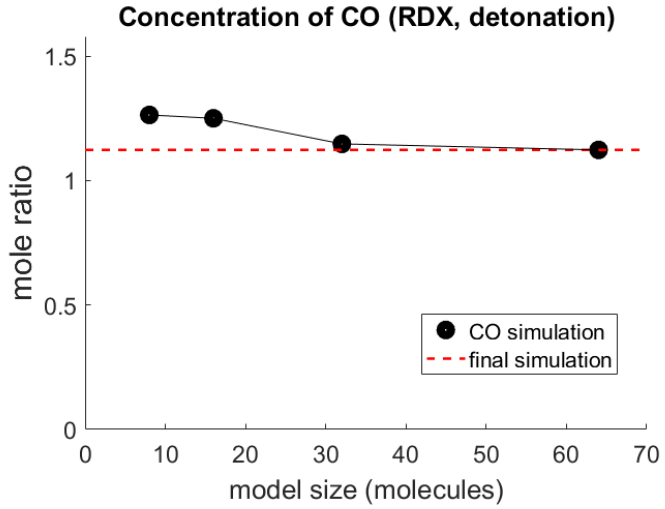

Figure C.21: Concentration of CO during steady state versus model size (NVE): RDX

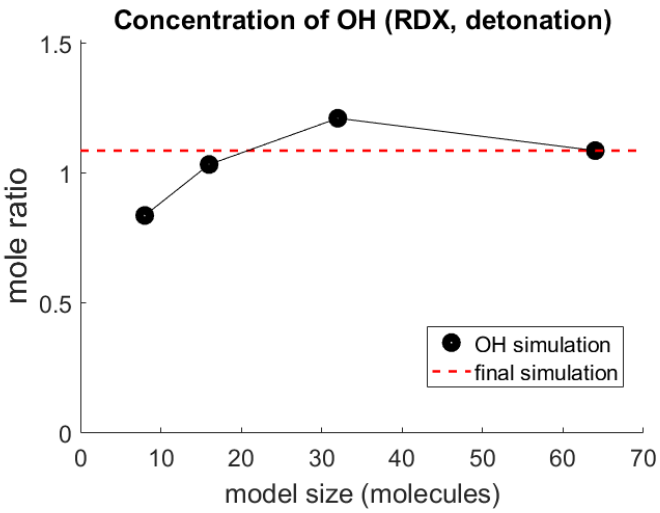

Figure C.22: Concentration of OH during steady state versus model size (NVE): RDX

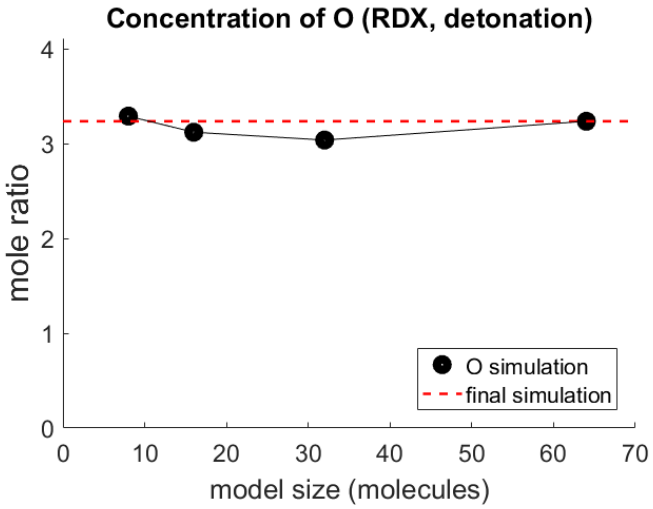

Figure C.23: Concentration of O during steady state versus model size (NVE): RDX

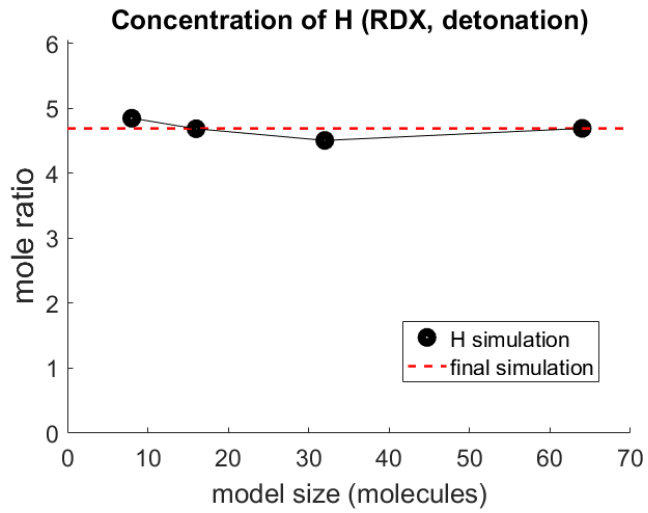

Figure C.24: Concentration of H during steady state versus model size (NVE): RDX

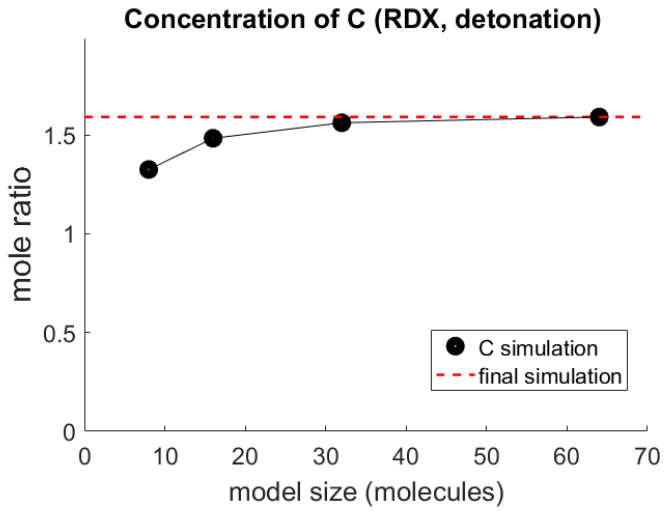

Figure C.25: Concentration of C during steady state versus model size (NVE): RDX

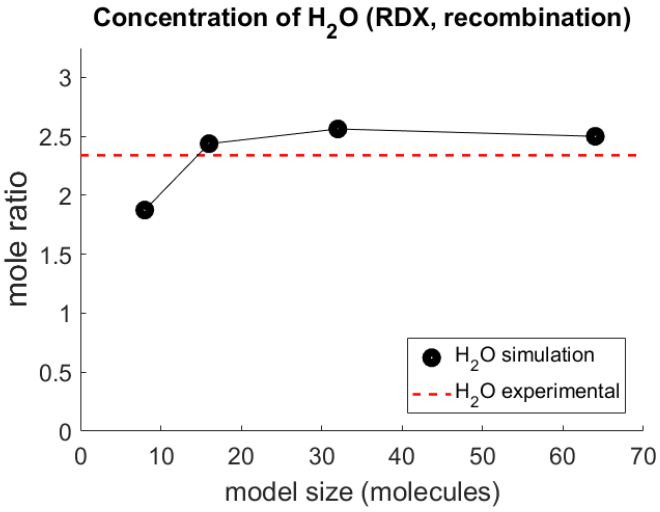

Figure C.26: Product mole ratios for H_2O versus model size: RDX

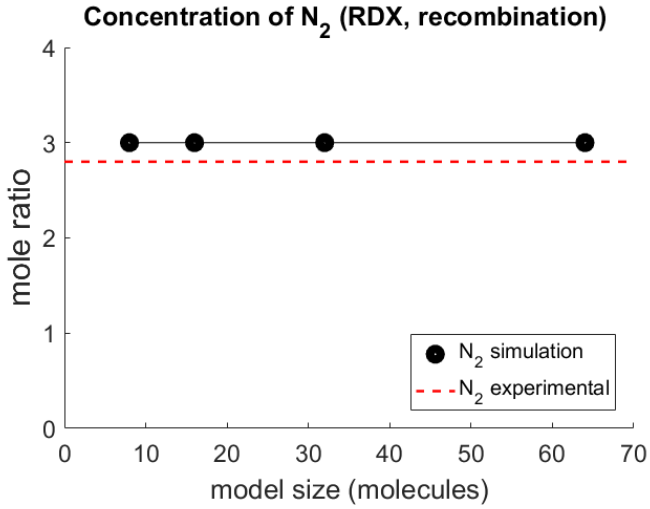

Figure C.27: Product mole ratios for N_2 versus model size: RDX

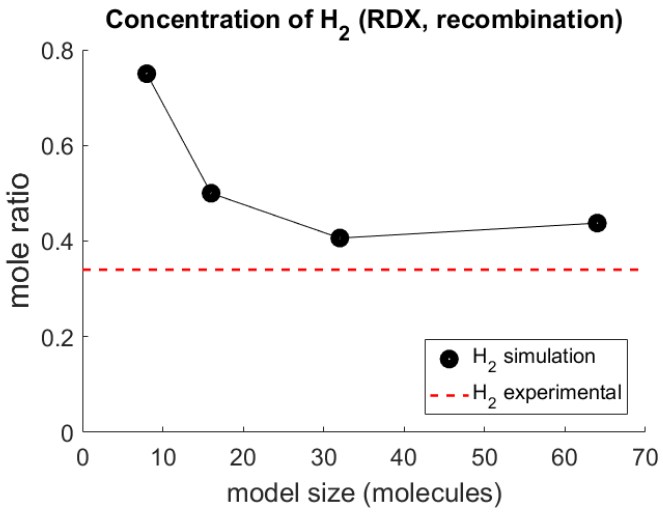

Figure C.28: Product mole ratios for H_2 versus model size: RDX

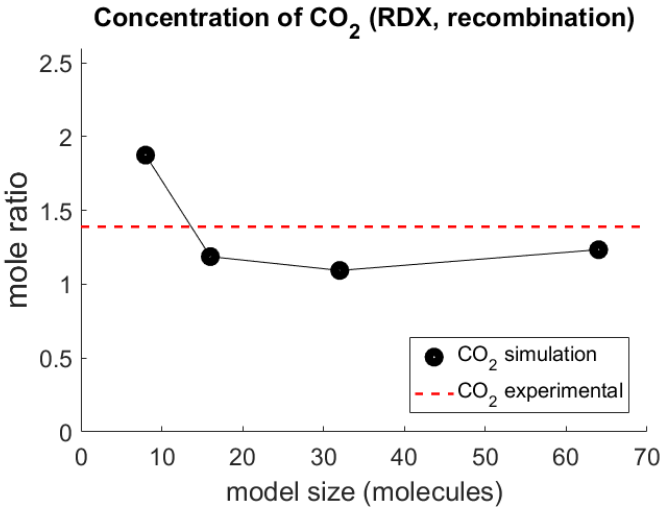

Figure C.29: Product mole ratios for CO_2 versus model size: RDX

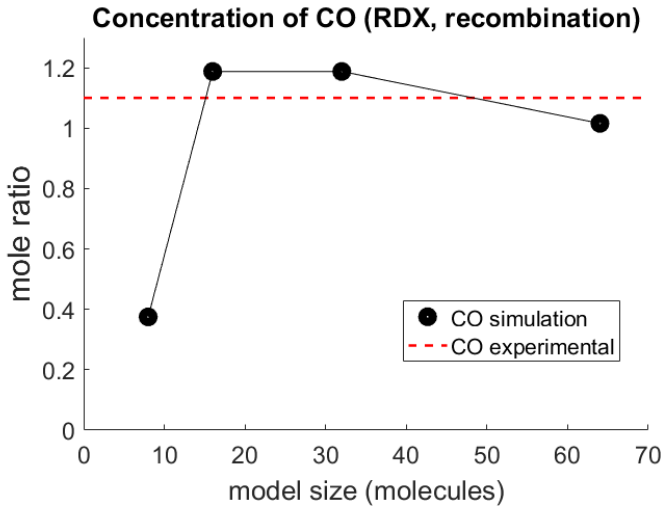

Figure C.30: Product mole ratios for CO versus model size :RDX

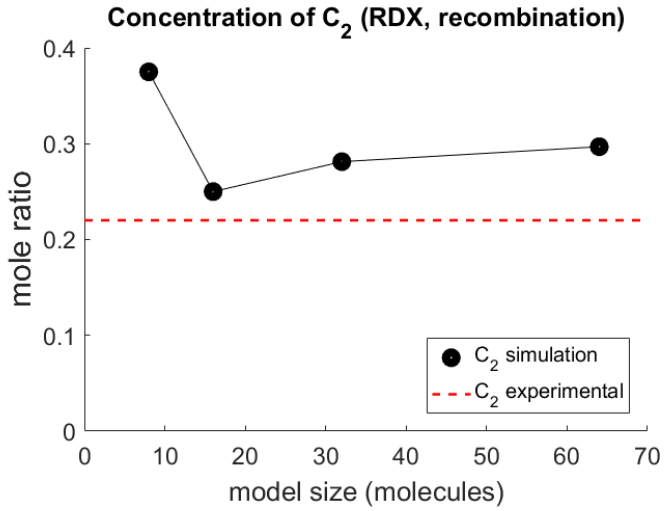

Figure C.31: Product mole ratios for C_2 versus model size: RDX

Bibliography

[1] G. C. Abell. Empirical chemical pseudopotential theory of molecular and metallic bonding. *Physical Review B*, 31:6184–6196, 1984.

[2] J. Akhavan. *The chemistry of explosives*. RSC Publishing, 2011.

[3] R. L. C. Akkermans, S. Toxvaerd, and W. J. Briels. Molecular dynamics of polymer growth. *Journal of Chemical Physics*, 109:2929–2940, 1998.

[4] F. H. Allen, D. G. Watson, L. Bammer, A. G. Orepen, and R. Taylor. Typical interatomic distances:organic compounds. *International Tables of Crystallography*, C:790–811, 2006.

[5] A. An, Y. Liu, S. V. Zybin, H. Kin, and W. A. Goddard. Anisotropic shock sensitivity of cyclotrimethylene trinitramine (RDX) from compress-and-shear reactive dynamics. *Journal of Physical Chemistry C*, 116:1019810206, 2012.

[6] H. C. Andersen. Molecular dynamics simulations at constant pressure and/or temperature. *The Journal of Chemical Physics*, 72(4):2384–2393, 1980.

[7] H. Balamane, T. Halicioglu, and W. A. Tiller. Comparative study of silicon empirical interatomic potentials. *Physical Review B*, 46(4), 1992.

[8] J. Bass and E. Fahrenthold. Nonholonomic hamiltonian method for molecular dynamics simulations of reacting shocks. *presented at the 19th American Physical Society SCCM Conference*, 2015.

[9] J. Bass and E. Fahrenthold. A kinetic formulation of reacting molecular dynamics. *Proceedings of the ASME 2016 International Mechanical Engineering Congress and Exposition*, 2016.

[10] R. Behrens. Identification of octahydro-1,3,5,7- tetranitro-1,3,5,7-tetrazocine (hmx) pyrolysis products by simultaneous thermogravimetric modulated beam mass spectrometry and time-of-flight velocity-spectra measurement. *International Journal of Chemical Kinetics*, 22:135–157, 1990.

[11] R. Behrens. Thermal decomposition of energetic materials: Temporal behaviors of the rates of formation of the gaseous pyrolysis products from condensed-phase decomposftion of octahydro-l,3,5,7-tetranitro-l,3,5,7-tetrazocine. *Journal of Physical Chemistry*, 94:6706–6718, 1990.

[12] M. A. Bellucci and D. F. Coker. Empirical valence bond models for reactive potential energy surfaces: A parallel multilevel genetic program approach. *Journal of Chemical Physics*, 135(044115), 2011.

[13] H. J. C. Berendsen, J. P. M. Postma, W. F. van Gunsteren, A. DiNola, and J. R. Haak. Molecular dynamics with coupling to an external bath. *The Journal of Chemical Physics*, 81(8):3684–3690, 1984.

[14] J. K. Brennan, M. Lisal, K. E. Gubbins, and B. M. Rice. Reaction ensemble molecular dynamics: Direct simulation of the dynamic equilibrium properties of chemically reacting mixtures. *Physical Review E*, 70(061103), 2004.

[15] J. K. Brennan, M. Lisal, J. D. Moore, S. Izvekov, I. V. Schweigert, and J. P. Larentzos. Coarse-grain model simulations of nonequilibrium dynamics in heterogeneous materials. *Journal of Physical Chemistry Letters*, 5:21442149, 2014.

[16] D. W. Brenner. Detonations at nanometer resolution using molecular dynamics. *Physical Review Letters*, 70(14):2174–2177, 1993.

[17] D. W. Brenner, C. T. White, M. L. Elert, and F. E. Walker. Chemical model for intrinsic detonation velocities. *International Journal of Quantum Chemistry: Quantum Chemistry Symposium*, 23:333–337, 1989.

[18] J. Budzien, A. P. Thompson, and S. V. Zybin. Reactive molecular dynamics simulation of shock through a single crystal of pentaerythritol tetranitrate. *Journal of Physical Chemistry B*, 113:13142–13151, 2009.

[19] S. N. Bulusu, editor. *Chemistry and Physics of Energetic Materials*, volume 309 of *Series C: Mathmatics and Physical Science*. Kluwer Academic Publishers, 1989.

[20] D. Chakraborty, R. P. Muller, S. Dasupta, and W. A. Goddard. A detailed model for the decomposition of nitramines: RDX and HMX.

Journal of Computer-Aided Material Design, 8:203–212, 2001.

[21] Y. Cheng, T. Shan, T. Liang, R. K. Behera, S. R. Phillpot, and S. B. Sinnott. A charge optimized many-body (COMB) potential for titanium and titania. *Journal of Physics: Condensed Matter*, 26(115327), 2014.

[22] K. Chenoweth, A. C. T. van Duin, and W. A. Goddard. Reaxff reactive force field for molecular dynamics simulations of hydrocarbon oxidation. *Journal of Physical Chemistry A*, 112:1040–1053, 2008.

[23] K. Chenoweth, A. C. T. van Duin, P. Persson, M. Cheng, J. Oxgaard, and W. A. Goddard. Development and application of a reaxff reactive force field for oxidative dehydrogenation on vanadium oxide catalysts. *Journal of Physical Chemistry*, 112:14645–14654, 2008.

[24] C. S. Choi and H. P. Boutin. A study of the crystal strueture of beta cyelotetramethylene tetranitramine by neutron diffraetion. *Acta Cryst.*, B26:1235–1240, 1970.

[25] C. S. Choi and E. Prince. The crystal structure of cyelotrimethylene-trinitramine. *Acta Cryst.*, B28:2857–2862, 1972.

[26] B. Darwent. Bond dissociation energies in simple molecules. Technical report, National Bureau of Standards, 1970.

[27] J. Dean, editor. *Handbook of Chemistry (15th edition).* McGraw-Hill, New York, 1999.

[28] B. Devine, T. Shan, Y. Cheng, A. J. McGaughey, M. Lee, S. R. Phillpot, and S. B. Sinnott. Atomistic simulations of copper oxidation and cu/cu2o interfaces using charge-optimized many-body potentials. *Physical Review B*, 84(125308), 2011.

[29] F. Dubnikova, R. Kosloff, Y. Zeiri, and Z. Karpas. Novel approach to the detection of triacetone triperoxide (TATP): Its structure and its complexes with ions. *The Journal of Physical Chemistry A*, 106:4951–4956, 2002.

[30] M. R. Mannaa L. E., Fried, C. F. Melius, M. Elstner, and T. Frauenheim. Decompostion of hxm at extreme conditions: A molecular dynamics simulation. *Journal of Physical Chemistry A*, 106:9024–9029, 2002.

[31] D. M. Elert, D. W. Brenner, and C. T. White. One-dimensional molecular-dynamics simulation of the detonation of nitric oxide. *Physcial Review B*, 39(2):1453–1456, 1989.

[32] E. P. Fahrenthold. Computational design of orbital debris shielding. In *AIAA 2014-4176*, 2014.

[33] E. P. Fahrenthold. Computational evaluation of metal foam orbital debris shielding. In *IEEE 978-1-4799-5380-6/15*, 2015.

[34] K. Farah, F. Muller-Plathe, and M. C. Bohm. Classical reactive molecular dynamics implementations: State of the art. *Journal of Chemical Physics and Physical Chemistry*, 13:1127–1151, 2012.

[35] J. C. Fogarty, H. M. Aktulga, A. Y. Grama, A. C. T. van Duin, and S. A. Pandit. A reactive molecular dynamics simulation of the silica-water interface. *Journal of Chemical Physics*, 132(174704), 2010.

[36] D. Furman, R. Kosloff, F. Dubnikova, S. V. Zybin, W. A. Goddard, N. Rom, B. Hurshberg, and Y. Zeiri. Decomposition of condensed phase energetic materials: Interplay between uni- and bimolecular mechanisms. *Journal of the Americal Chemical Society*, 136:41924200, 2014.

[37] N. Ge, Y. Wei, Z. Song, X. Chen, G. Ji, F. Zhao, and D. Wei. Anisotropic responses and initial decomposition of condensed phase b-hmx under shock loading via molecular dynamics simulation in conjunction with multiscale shock techniques. *Journal of Physical Chemistry B*, 118:8691–8699, 2014.

[38] T. C. Germann, B. L. Holian, P. S. Lomdahl, A. J. Heim, N. Grønbech-Jensen, and J. Maillet. Molecular dynamics simulations of detonation in defective explosive crystals. Technical report, Los Alamos, 2002.

[39] B. Gruber and V. Carsten. The impact of viscous effects on the aerodynamic damping of vibrating transonic compressor blades - a numerical study. *Journal of Turbomachinery-Transactions of the ASME*, 2001.

[40] D. Guo, Q. An, W. A. Goddard, S. V. Zybin, and F. Huang. Compressive shear reactive molecular dynamics studies indicating that cocrystals of tnt/cl-20 decrease sensitivity. *Journal of Physical Chemistry C*, 118:30202–30208, 2014.

[41] F. Guo, X. Cheng, , and H. Zhang. Reactive molecular dynamics simulation of solid nitromethane impact on (010) surfaces induced and nonimpact thermal decomposition. *Journal of Physical Chemistry A*, 116:3514–3520, 2012.

[42] S. Han, A. C. T. van Duin, W. A. Goddard, and A. Strachan. Thermal decomposition of condensed-phase nitromethane from molecular dynamics from reaxff reactive dynamics. *Journal of Physical Chemistry B*, 115:6534–6540, 2011.

[43] Y. Han, D. Jiang, J. Zhang, W. Li, Z. Gan, and J. Gu. Development, applications and challenges of reaxff reactive force field in molecular simulations. *Front. Chem. Sci. Eng*, 10:16–38, 2016.

[44] D. E. Hanson, J. D. Kress, and A. F. Voter. An interatomic potential for reactive ion etching of si by cl ions. *Journal of Chemical Physics*, 110(5983), 1999.

[45] A. J. Heim, N. Grønbech-Jensen, T. C. Germann, E. M. Kober, B. L. Holian, and P. S. Lomdahl. The influence of interatomic bonding potentials on detonation properties. *Condensed Matter Material Science*, 2013.

[46] A. J. Heim, N. Grønbech-Jensen, E. M. Kober, J. J. Erpenbeck, and T. C. Germann. Interaction potential for atomic simulations of conventional high explosives. *Physical Review E*, 78(046709), 2008.

[47] A. J. Heim, N. Gronbenbech-Jensen, T. C. Germann, B L. Holian, E. M. Kober, and P. S. Lomdahl. Influence of interatomic bonding potentials on detonation properties. *Physical Review E*, 76(026318), 2007.

[48] A. J. Heim, N.Grønbech-Jensen, E. M. Kober, and T. C. Germann. Molecular dynamics simulations of detonation instability. *Physical Review E*, 78(046710), 2008.

[49] K.O.E. Henriksson, C. Bjorkas, and K. Nordlund. Atomistic simulations of stainless steels: a many-body potential for the Fe–Cr–C system. *Journal of Physics: Condensed Matter*, 25(445401), 2013.

[50] R. J. Hernandez and E. P.Fahrenthold. Hybrid particle-element method for an unstructured hexahedral mesh. *International Journal for Numerical Methods in Engineering*, 94:1191–1215, 2013.

[51] P. H. Hünenberger. Thermostat algorithms for molecular dynamics simulations. *Advanced computer simulation approaches for soft matter sceince 1*, 173:105–149, 2005.

[52] T. T. Jarvi, A. C. T. van Duin, K. Nordlund, and W. A. Goddard. Development of interatomic reaxff potentials for Au-S-C-H systems. *Journal of Physical Chemistry A,*, 115:10315–10322, 2011.

[53] J. C. Koo and E. P. Fahrenthold. Discrete hamilton's equations for arbitrary lagrangian eulerian dynamics of viscous compressible flow. *Computer Methods in Applied Mechanics and Engineering*, 189:875–900, 2000.

[54] K. K. Kuo. *Principles of Combustion*. Wiley, second edition, 2005.

[55] R. Kutteh. New approaches for molecular dynamics simulations with nonholonomic constraints. *Computer Physics Communications*, 119:159–168, 1999.

[56] R. Kutteh and R. B. Jones. Rigid body molecular dynamics with nonholonomic constraints: Molecular thermostat algorithms. *Physical Review E*, 61(3):3186–3198, 2000.

[57] T. Lappas, A. Leonard, and P. Dimotakis. An adapative lagrangian method for computing 1d reacting and nonreacting flows. *Journal of Computational Physics*, 104:361–376, 1993.

[58] J. P. Larentzos, B M. Rice, E. F. C. Byrd, N. S. Weingarten, and J. V. Lill. Parameterizing complex reactive force fields using multiple objective evolutionary strategies (MOES). part 1: Reaxff models for cyclotrimethylene trinitramine (RDX) and 1,1-diamino-2,2- dinitroethene (FOX-7). *Journal of Chemical Theory and Computation*, 11:381–391, 2015.

[59] S. Lee and E. P. Fahrenthold. Nonholonomic hamiltonian method for meso-macroscale simulations of reacting shocks. In *AIP Conference Proceedings*, volume 1793, 2015.

[60] L. Li, M. Xu, W. Song, A. Ovcharenko, G. Zhang, and D. Jia. The effect of empirical potential functions on modeling of amorphous carbon

using molecular dynamics method. *Applied Surface Science*, 286:287–297, 2013.

[61] T. Liang, B. Devine, S. R. Phillpot, and S. B. Sinnot. Variable charge reactive potential for hydrocarbons to simulate organic-copper interactions. *The Journal of Physical Chemistry A*, 116:79767991, 2012.

[62] T. Liang, Y. K. Shin, Y. Cheng, D. E. Yilmaz, K. G. Vishnu, O. Verners, C. Zou, S. R. Phillpot, S. B. Sinnott, and A. C.T. van Duin. Reactive potentials for advanced atomistic simulations. *Annual Review of Materials Research*, 43:109–129, 2013.

[63] J. H. Lii and N. L. Alinger. Molecular mechanics. the mm3 force field for hydrocarbons. 2. vibrational frequencies and thermodynamics. *Journal of the American Chemical Society*, 1989.

[64] C. Lin, H. Wang, M. C. Lin, and C. F. Melius. A shock tube study of the CH2O+NO2 reaction at high temperatures. *International Journal of Chemical Kinetics*, 22:455–482, 1990.

[65] H. Liu, H. Qian, Y. Zhao, and Z. Lu. Dissipative particle dynamics simulation study on the binary mixture phase separation coupled with polymerization. *The Journal of Chemical Physics*, 127(144903), 2007.

[66] L. Liu, Y. Liu, S. V. Zybin, H. Sun, and W. A. Goddard. Reaxff-lg: Correction of the reaxff reactive force field for london dispersion,

with applications to the equations of state for energetic materials. *The Journal of Physical Chemistry A*, 115:11016–11022, 2011.

[67] Y. Long and J. Chen. Systematic study of the reaction kinetics for HMX. *Journal of Physical Chemistry A*, 119:4037–4082, 2015.

[68] B. Lu, X. Cheng, J. Huang, and J. A. McCammon. Order n algorithm for computation of electrostatic interactions in biomolecular systems. *Proceedings of the National Academy of Sciences of the United States of America*, 103:19314–19319, 2006.

[69] M. R. Manaa and L. E. Fried. Intersystem crossings in model energetic materials. *Journal of Physical Chemistry A*, 103:9349–9354, 1999.

[70] D. Marx and J. Hutter. *Ab Initio Molecular Dynamics*. Cambridge University Press New York and the United Kingdom, 2009.

[71] MathWork. *Matlab Optimization Toolbox User's Guide*.

[72] R. R. Mcguire and T. C. Tarver. Chemical-decomposition models for the thermal explosion of confined hmx, tatb, rdx, and tnt explosives. In *Seventh Symposium on Detonation*, pages 1–8, 1981.

[73] D. A. McQuarrie. *Statistical Mechanics*. New York: Harper and Row, 1976.

[74] C. U. Morgan and R. A. Beyer. Electron-spin- resonance studies of hmx pyrolysis products. *Combustion and Flame*, 36:99–101, 1979.

[75] T. Nagy, J. Y. Reyes, and M. Meuwly. Multisurface adiabatic reactive molecular dynamics. *Journal of Chemical Theory and Computation*, 10:1366–1375, 2014.

[76] K. D. Nielson, A. C. T. van Duin, J. Oxgaard, W. Deng, and W. A. GoddardIII. Developement of the reaxff reactive force field for describing transition metal catalyzed reaction, with application to the initial stages of the catalytic formation of carbon nanotubes. *Journal of Physical Chemistry. A*, 109:493–499, 2005.

[77] K. Nomura, R. K. kalia, A. Nakano, and P. Vashishta. A scalable parallel algorithm for large-scale reactive force-field molecular dynamics simulations. *Computer Physics Communications*, 178:73–78, 2008.

[78] K. Nomura, R. K. Kalia, A. Nakano, P. Vashishta, A. C. T. van Duin, and W. A. Goddard. Dynamic transition in the structure of an energetic crystal during chemical reactions at shock front prior to detonation. *Physical Review Letters*, 99(148303), 2007.

[79] M. R. Nyden, G. P. Forney, and J. E. Brown. Molecular modeling of polymer flammability: Application to the design of flame-resistant polyethylene. *Macromolecules*, 25:1658–1666, 1992.

[80] T. C. O'Connor, J. Andzelm, and M. O. Robbins. Airebo-m: A reactive model for hydrocarbons at extreme pressures. *Journal of Chemical Physics*, 142(024903), 2015.

[81] J. G. O. Ojwang, S. Chaudhuri, A. C. T. van Duin, Y. J. Chabal, and J. Veyan. Multiscale modeling of interaction of alane cluster on al(111) surfaces: A reactive force field and infrared absorption spectroscopy approach. *The Journal of Chemical Physics*, 132(084509), 2010.

[82] D. Ornellas. The heat and products of detonation of hmx, tnt, nm, and fefo. *Journal of Physical Chemistry*, 72(7):2390–2394, 1967.

[83] D. L. Ornellas. Calorimetric determination of the heat and products of detonation for explosives: October 1961 to april 1982. Technical report, Lawrence Livermore Labratory, 1982.

[84] N. Parsons, D. A. Levin, and A. C. T. van Duin. Molecular dynamics based chemistry models of hypervelocity collisions of O(3P) + SO2(X, 1A1) in dsmc. *Journal of Chemical Physics*, 138(044316), 2013.

[85] M. Perez, O. Lame, F. Leonforte, and J. Barrat. Polymer chain generation for coarse-grained models using radical like polymerization. *The Journal of Chemical Physics*, 128(234904), 2008.

[86] M. J. Pilling and P. W. Seakin. *Reaction Kinetics*. Oxford University Press, 1995.

[87] P. Politzer and J. S. Murray. Detonation performance and sensitivity: A quest for balance. *Advances in Quantum Chemistry*, 69:1–30, 2014.

[88] P. Politzer and J. S. Murray. The role of product composition in determining detonation velocity and detonation pressure. *Central European Journal of Energetic Materials*, 2014.

[89] O. Rahaman, A. C. T. van Duin, W. A. Goddard, and D. J. Doren. Development of a reaxff reactive force field for glycine and application to solvent effect and tautomerization. *Journal of Physical Chemistry B*, 115:249–261, 2011.

[90] B. M. Rice, W. Mattson, J. Grosh, and S. F. Trevino. Molecular-dynamics study of detonation. ii. the reaction mechanism. *Physcial Review E*, 53:623–635, 1996.

[91] B. M. Rice, M. William, and J. Grosh. Molecular dynamics study of detonation: I. a comparison with hydrodynamic predictions. *Physical Review E*, 53(1):611–622, 1996.

[92] N. Rom, S. V. Zybin, A. C. T. van Duin, W. A. Goddard, Y. Zeiri, G. Katz, and R. Kosloff. Density-dependent liquid nitromethane decomposition: Molecular dynamics simulations based on reaxff. *Journal of Physical Chemistry A*, 115:10181–10202, 2011.

[93] M. F. Russo and A. C. T. van Duin. Atomistic-scale simulations of chemical reactions: bridging from quantum chemistry to engineering. *Nuclear Instruments and Methods in Physics Research B*, 269:1549–1554, 2011.

[94] D. E. Sagnella and M. E. Tuckerman. An empirical valence bond model for proton transfer in water. *Journal of Chemical Physics*, 108:2073–2083, 1998.

[95] F. A. Sapozhnikov, V. V. Dremov, I. V. Derbenev, A. V. Karavae, and L. Soulard. Molecular dynamics simualtion of tatb-like explosives. In *Shock Compression of Condensed Matter*, pages 463–466, 2007.

[96] T. P. Senftle, S. Hong, M. Islam, S. B. Kylasa, Y. Zheng, T. K. Shin, C. Junkermeier, R. Engel-Herbert, M. J. Janik, H. M. Aktulga, T. Verstraelen, A. Grama, and A. C. T. van Duin. The reaxff reactive force-field: development, applications and future directions. *Nature Partner Journals :Computational Materials*, 2(15011), 2016.

[97] T. Shan, B. D. Devine, S. R. Phillpotm, and S. B. Sinnot. Molecular dynamics study of the adhesion of Cu/SiO2 interfaces using a variable-charge interatomic potential. *Physical Review B*, 83(315007), 2011.

[98] T. Shan, D. B. Devine, J. M. Hawkins, A. Ashagiri, S. R. Phillpot, and S. B. Sinnott. Second generation charge-optimized many-body potential for Si/SiO2 and amorphous silica. *Physical Review B*, 82(235302), 2010.

[99] O. Sharia and M. M. Kuklja. Ab initio kinetics of gas phase decomposition reactions. *Journal of Physical Chemistry A*, 114:12656–12661, 2010.

[100] K. D. Smith, M. Bruns, S. I. Stoliarov, M. R. Nyden, O. A. Ezekoye, and P. R. Westmoreland. Assessing the effect of molecular weight on the kinetics of backbone scission reaction in polyethylene using reactive molecular dynamics. *Polymer*, 52:3104–3111, 2011.

[101] H. Song, Y. Zhang, H. Li, T. Zhou, and G. Huang. All-atom, non-empirical, and tailor-made force field for alpha-rdx from first principles. *Royal Society of Chemistry*, 4:40518–40533, 2014.

[102] M. J. Stevens. Interfacial fracture between highly cross-linked polymer networks and a solid surface: Effect of interfacial bond density. *Macromolecules*, 34:2710–2718, 2001.

[103] A. Strachan, E. Kober, A. C. T. van Duin, J. Oxgaard, and W. A. Goddard. Thermal decomposition of rdx from reactive molecular dynamics. *Journal of Chemical Physics*, 122(054502), 2005.

[104] A. Strachan, A. C. T. van Duin, D. Chakraborty, S. Dasgupta, and W. A. Goddard. Shock waves in high-energy materials: The initial chemical events in nitramine rdx. *Physical Review Letters*, 91(098301), 2003.

[105] A. Strachan, A. C. T. van Duin, and W. A. Goddard. Initial chemical events in the energetic material rdx under shock loading: role of defects. In *Shock Compression of Condensed Matter 2003*, pages 895–898, 2003.

[106] S. J. Stuart, A. B. Tutein, and J. A. Harrison. A reactive potential for hydrocarbons with intermolecular interactions. *Journal of Chemical*

Physics, 112:6472–6486, 2000.

[107] C. M. Tarver and T. D. Tran. Thermal decomposition models for hmx-based plastic bonded explosives. *Combustion and Flame*, 137:50–62, 2004.

[108] D. E. Taylor, K. E. Strawhecker, E. R. Shanholtz, D. C. Sorescu, and R. C. Sausa. Investigations of the intermolecular forces between rdx and polyethylene by force distance spectroscopy and molecular dynamics simulations. *Journal of Phsical Chemistry A*, 118:50835097, 2014.

[109] J. Tersoff. New empirical model for the structural properties of silicon. *Physical Review Letters*, 56(6):632–635, 1986.

[110] J. Tersoff. Modeling solid-state chemistry: Interatomic potentials for mnlticomponent systems. *Physical Review B*, 39(8):5566–5568, 1989.

[111] A. C. T. van Duin, S. Dasgupta, F. Lorant, and W. A. Reaxff: A reactive force field for hydrocarbons. *Journal of Physical Chemistry A*, 105:9396–9409, 2001.

[112] A. C. T. van Duin, Y. Zeiri, F. Dubnikova, R. Kosloff, and W. A. Goddard. Atomistic-scale simulations of the initial chemical events in the thermal initiation of triacetonetriperoxide. *Journal of the American Chemical Society*, 127:11053–11062, 2005.

[113] K. Vanommeslaeghe, E. Hatcher, C. Acharya, S. Kundu, S. Zhong, J. Shim, E. Darian, O. Guvench, P. Lopes, I. Vorobyov, and A. D. Mack-

erell. Charmm general force field: A force field for drug-like molecules compatible with the charmm all-atom additive biological force fields. *The Journal of Computational Chemistry*, 2010.

[114] R. S. Vařeková, Z. Jirouskova, J. Vanek, S. Suchomel, and J. Koca. Electronegativity equalization method: Parameterization and validation for large sets of organic, organohalogene and organometal molecule. *International Journal of Molecular Science*, 8:572–582, 2007.

[115] V. Varshney, S. S. Patnaik, A. K. Roy, and B. L. Farmer. A molecular dynamics study of epoxy-based networks: Cross-linking procedure and prediction of molecular and material properties. *Macromolecules*, 41:6837–3842, 2008.

[116] R. L. C. Vink, G. T. Barkema, W. F. van der Weg, and N. Mousseau. Fitting the stillinger-weber potential to amorphous silicon. *Journal of Non-Crystalline Solids*, 282:248–255, 2001.

[117] M. Warrier, P. Pahari, and S. Chaturvedi. Interatomic potential parameters for molecular dynamics simulations of RDX using a reactive force field: A validation study. *Journal of Physics: Conference Series*, 377(012100), 2012.

[118] N. S. Weingarten and B. M. Rice. Evaluation of reaxff-lg force fields for use in molecular dynamics simulations of sucrose. *Theoretical Chemistry Accounts*, 135(227), 2016.

[119] M. A. Wood, A. C. T. van Duin, and A. Strachan. Coupled thermal and electromagnetic induced decomposition in the molecular explosive hmx; a reactive molecular dynamics study. *Journal of Physcial Chemistry A*, 118:885895, 2014.

[120] L. Xiaohan, P. Xindong, and L. Xingliang. An improved dynamic core for a non-hydrostatic model system on the yin-yang grid. *Advances in Atmospheric Sciences*, 2015.

[121] Q. Yan, S. Zeman, P. E. S. Jimenez, T. Zhang, L. A. Perez-Maqueda, and A. Elbeih. The mitigation effect of synthetic polymers on initiation reactivity of cl-20: Physical models and chemical pathways of thermolysis. *The Journal of Physical Chemistry C*, 118:2288122895, 2014.

[122] L. Zhang, A. C. T. van Duin, S. V. Zybin, and W. A. Goddard. Thermal decomposition of hydrazines from reactive dynamics using the reaxff reactive force field. *Journal of Physical Chemistry B*, 113:10770–10778, 2009.

[123] L. Zhang, S. V. Zybin, A. C. T. van Duin, S. Dasgupta, and W. A. Goddard. Shock induced decomposition and sensitivity of energetic materials by reaxff molecular dynamics. In *Shock Compression of Condensed Matter*, pages 585–588, 2005.

[124] L. Zhang, S. V. Zybin, A. C. T. van Duin, and W. A. Goddard. Modeling high rate impact sensitivity of perfect rdx and hmx crystals by reaxff reactive dynamics. *Journal of Energetic Materials*, 28:92–127, 2010.

[125] L. Zhang, V. Zybin, A. C. T. van Duin, S. Dasgupta, W. A. Goddard, and E. M. Kober. Carbon cluster formation during thermal decomposition of octahydro-1,3,5,7-tetranitro- 1,3,5,7-tetrazocine and 1,3,5-triamino-2,4,6-trinitrobenzene high explosives from reaxff reactive molecular dynamics simulations. *Journal of Physcial Chemistry A*, 113:10619–10640, 2009.

[126] S. Zhang and T. N. Truong. Branching ratio and pressure dependent rate constants of multichannel unimolecular decomposition of gas phase a hmx: An ab initio dynamics study. *Journal of Physical Chemistry A*, 105:2427–2434, 2001.

[127] T. Zhou, L. Liu, W. A. Goddard, S. V. Zybin, and F. Huang. Reaxff reactive molecular dynamics on silicon pentaerythritol tetranitrate crystal validates the mechanism for the colossal sensitivity. *Journal of Physical Chemistry and Chemical Physics*, 16:23779–23791, 2014.

[128] S. V. Zybin, W. A. Goddard, P. Xu, A. C. T. van Duin, and A. P. Thompson. Physical mechanism of anisotropic sensitivity in pentaerythritol tetranitrate from compressive-shear reaction dynamics simulations. *Applied Physics Letters*, 96(081918), 2010.

[129] S. V. Zybin, P. Xu, Q. An, and W. A. Goddard. Reaxff reactive molecular dynamics: Coupling mechanical impact to chemical initiation in energetic materials. In *2010 DoD High Performance Computing Modernization Program Users Group Conference*, pages 273–278. IEEE, 2010.

Vita

Joseph Louis Bass was born in Austin, Texas to Jon Mical Bass and K Richelle Bass. He graduated from McCallum High School in Austin, Texas in 2009. Upon graduating he spent four years pursuing a Bachelor of Science degree in Mechanical Engineering from the University of Texas, graduating in May of 2013. He entered into graduate school in the summer of 2013 and began the pursuit of his PhD in Mechanical Engineering.

Email address: Josephbass627@gmail.com

This dissertation was typeset with LaTeX[†] by the author.

[†]LaTeX is a document preparation system developed by Leslie Lamport as a special version of Donald Knuth's TeX Program.